INFORMATION TO USERS

This manuscript has been reproduced from the microfilm master. UMI films the text directly from the original or copy submitted. Thus, some thesis and dissertation copies are in typewriter face, while others may be from any type of computer printer.

The quality of this reproduction is dependent upon the quality of the copy submitted. Broken or indistinct print, colored or poor quality illustrations and photographs, print bleedthrough, substandard margins, and improper alignment can adversely affect reproduction.

In the unlikely event that the author did not send UMI a complete manuscript and there are missing pages, these will be noted. Also, if unauthorized copyright material had to be removed, a note will indicate the deletion.

Oversize materials (e.g., maps, drawings, charts) are reproduced by sectioning the original, beginning at the upper left-hand corner and continuing from left to right in equal sections with small overlaps. Each original is also photographed in one exposure and is included in reduced form at the back of the book.

Photographs included in the original manuscript have been reproduced xerographically in this copy. Higher quality 6" x 9" black and white photographic prints are available for any photographs or illustrations appearing in this copy for an additional charge. Contact UMI directly to order.

UMI

A Bell & Howell Information Company
300 North Zeeb Road, Ann Arbor MI 48106-1346 USA
313/761-4700 800/521-0600

GENERATION AND MANIPULATION OF INFRARED LIGHT USING QUASI-PHASEMATCHED DEVICES: ULTRASHORT-PULSE, APERIODIC-GRATING AND GUIDED-WAVE FREQUENCY CONVERSION

A DISSERTATION
SUBMITTED TO THE DEPARTMENT OF ELECTRICAL ENGINEERING
AND THE COMMITTEE ON GRADUATE STUDIES
OF STANFORD UNIVERSITY
IN PARTIAL FULFILLMENT OF THE REQUIREMENTS
FOR THE DEGREE OF
DOCTOR OF PHILOSOPHY

Mark Alan Arbore

June 1998

I certify that I have read this dissertation and that in my opinion it is fully adequate, in scope and quality, as a dissertation for the degree of Doctor of Philosophy

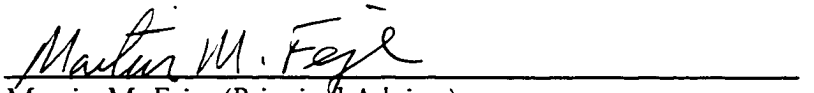

Martin M. Fejer (Principal Adviser)

I certify that I have read this dissertation and that in my opinion it is fully adequate, in scope and quality, as a dissertation for the degree of Doctor of Philosophy

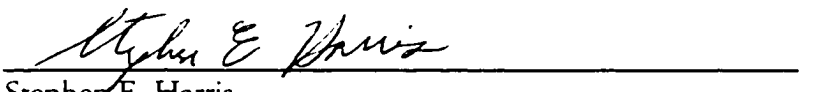

Stephen E. Harris

I certify that I have read this dissertation and that in my opinion it is fully adequate, in scope and quality, as a dissertation for the degree of Doctor of Philosophy

James S. Harris

Approved for the University Committee on Graduate Studies:

Abstract

Nonlinear optical frequency conversion is often used to extend the useful wavelength range of available laser sources - and has been employed commercially for decades. However, in many cases, inadequate properties of conventional nonlinear materials have prevented the application of frequency conversion to low power laser sources. Recent advances in nonlinear materials, particularly those making use of the quasi-phasematching (QPM) technique, have enabled the generation of an increasing range of wavelengths with improved efficiencies. Periodically (or aperiodically) poled lithium niobate (PPLN) is the most successful of the QPM-based materials, not only offering high efficiencies and wavelength versatility, but also enabling nonlinear frequency conversion interactions which are impossible with conventional materials.

In this thesis, I will describe several experiments which demonstrate frequency conversion using sub-picosecond ($<10^{-12}$ seconds) pulses with bulk PPLN as the nonlinear material. Both second harmonic generation (SHG) and tunable optical parametric generation (OPG) are described. Significantly greater efficiencies and/or lower thresholds are achieved with PPLN than are possible with conventional materials.

Then, I will describe an entirely new nonlinear optical process. This interaction, which relies on aperiodic QPM structures, is capable of simultaneous frequency conversion and compression of optical pulses. First, I detail the theoretical background for this interaction. Second, I describe experiments which show efficient conversion from 1560 to 780 nm while compressing pulses from 17 ps to 110 fs.

Finally, I will describe results of experiments employing annealed proton exchanged (APE)-PPLN waveguides for frequency conversion with even greater efficiencies. The 380-pJ-threshold OPG device that I demonstrated has a threshold which is two orders of magnitude below that of our bulk PPLN OPG device and four orders of magnitude below that of any other published OPG result in any material system in any geometry.

Acknowledgments

Many people have played important roles in my stay at Stanford, so many that I will not attempt (and fail) to thank them all here. However, I would be remiss to not acknowledge the many professors I have had the privilege of learning from in these four and a half years. Most notably, my thesis advisor, Marty Fejer, has devoted extraordinary amounts of time and attention to guiding my research and teaching me how to do things correctly. Marty always can suggest a myriad of ideas to pursue, whether the problem is experimental or theoretical.

I appreciate the time spent by Steve Harris and Jim Harris while serving on my reading committee and providing helpful comments on this dissertation. I also appreciate the efforts of Professors Bob Byer and Bernard Widrow, who served on my orals committee. I have always found Professor Byer's perspective valuable. During my first quarter at Stanford, I worked for Professor Richard Pantell and with Dr. Michel Digonnet on my first of several theoretical projects. Were it not for the intervention of Professor Fabian Pease while I was a prospective student, I might have gone elsewhere for graduate school. Finally, I appreciate all of the patience demonstrated by numerous to-remain-un-named professors who allowed me to turn in homework assignments extremely late when my research unfairly took priority.

I have greatly enjoyed the time spent with my friends, fellow graduate students and collaborators, as well as the many Ginzton personnel and technicians. From them, I learned much about life, as well as research. In particular, Mike Bortz has given me a steady stream of wise advice and Kellie Koucky has always treated me like a son. I have been fortunate enough to be given the opportunity to collaborate with so many researchers around the world, an unexpected pleasure of studying at Stanford. My long-standing collaboration with the team at IMRA lead to much of the research described in this dissertation.

My father always encouraged my academic pursuits, yet reminded me not to work too hard. My brother's skillful formatting of this dissertation enabled me to begin my new job when planned, and forget about editing for a while. Finally, I wish to thank Laura Smoliar for making the preceding one and one half years of my life so wonderful, even when the light at the end of the graduate-school tunnel was obscured.

Table of Contents

Abstract iv

Acknowledgments v

Table of Contents vi

List of Tables viii

List of Figures ix

Chapter 1: Introduction 1
- 1.1 Motivation 1
- 1.2 Nonlinear optical frequency conversion 2
- 1.3 Quasi-phasematching 4
- 1.4 Ultrashort pulse concepts 6
- 1.5 Ultrashort pulse frequency conversion concepts 7
- 1.6 Pulse compression with chirped QPM-SHG 10
- 1.7 Overview of this dissertation 12
- References 14

Chapter 2: Theory of quasi-phasematched ultrashort-pulse second harmonic generation 19
- 2.1 Introduction 19
- 2.2 Maxwell's equations 20
- 2.3 Frequency domain slowly-varying envelope equations 22
- 2.4 Derivation of the SHG output field 24
- 2.5 Continuous-wave SHG and tuning curves 27
- 2.6 Pulsed input fields and the derivation of the SHG transfer function 28
- 2.7 Quasi-static and nonstationary limits 33
- 2.8 Optimum crystal length regime 34
- 2.9 Transform limited fundamental pulses 37
- 2.10 Uniform quasi-phasematching 43
- 2.11 Ultrashort-pulse figure of merit 44
- 2.12 Comparison of nonlinear materials 47
- 2.13 Aperiodic QPM gratings 50
- 2.14 Linearly chirped QPM gratings 51
- 2.15 Compression of linearly chirped Gaussian pulses 52
- 2.16 Compression of arbitrary chirped pulses 55

2.17 Efficiency of pulse compression 56
2.18 Efficiency of pulse compression with focused beams 57
2.19 Group velocity dispersion at the fundamental frequency 60
2.20 Summary of chapter 61
References 62

Chapter 3: Quasi-phasematched ultrashort-pulse second harmonic generation experiments 64
3.1 Introduction 64
3.2 Efficient QPM-SHG with PPLN 65
3.3 Pulse compression with chirped-QPM SHG 73
3.4 Fiber-CPA system experiments using chirped-QPM SHG 78
3.5 Advantages of chirped-QPM 80
3.6 Summary of chapter 81
References 82

Chapter 4: Quasi-phasematched ultrashort-pulse optical parametric generation: theory and experiments 84
4.1 Introduction 84
4.2 Theory of ultrashort-pulse optical parametric generation (OPG) 85
4.3 Bulk OPG experiment 89
4.4 Waveguide OPG theory 92
4.5 Waveguide OPG background 96
4.6 Waveguide OPG experiment 98
4.7 Summary of chapter 100
References 101

Chapter 5: Conclusion 103
5.1 Summary of dissertation 103
5.2 Summary of results 103
5.3 Future directions 104
References 106

Appendix A: Alternate derivation of the second harmonic generation (SHG) transfer function: Time domain approach 107
A.1 Introduction 107
A.2 Slowly varying envelope approximation 107
A.3 The depletion-free and dispersion-free pump limit 109
A.4 Derivation of the SHG transfer function 110
References 114

Appendix B: Summary of notation used in chapter 2 115

List of Tables

2.1 Time-bandwidth products evaluated for various pulse shapes 37

2.2 Numerical efficiency and pulse-length factors evaluated for various pulse shapes 41

2.3 Optimum crystal length and efficiency evaluated for various pulse shapes 42

2.4 Pulse shape efficiency parameter for optimum crystal length for various pulse shapes ... 47

2.5 Comparison of the ultrashort-pulse figure of merit (FOM) for several technologically important nonlinear materials. 48

B.1 Summary of notation used in chapter 2 115

List of Figures

1.1 Comparison of non-phasematched, phasematched and quasi-phasematched frequency conversion 5

1.2 Continuous-wave (CW) and ultrashort-pulse optical waves in both the time and frequency domains. 7

1.3 Group velocity and phase velocity for ultrashort pulses. 8

1.4 Pulse stretching and compression with dispersive systems. 8

1.5 Summary of effects related to group velocity mismatch during nonlinear optical frequency conversion. 9

1.6 SHG in chirped QPM structures 11

1.7 Mechanism of pulse compression during SHG in a chirped-QPM grating. 12

2.1 The SHG efficiency depends on the crystal length and on the pulse shape. 39

2.2 The SH pulse length depends on the crystal length and on the pulse shape. 40

2.3 Temporal shapes of SH waveforms (shown on a linear scale) for $sech^2$ fundamental pulses and crystals of various lengths. 41

2.4 Comparison of three technologically important nonlinear materials. 49

2.5 Normalized input and output pulse lengths for SHG in a chirped-QPM grating. 55

2.6 Normalized conversion efficiencies for SHG in a chirped-QPM grating.....58

3.1 Measured fundamental pulse spectrum shown on a linear scale. 66

3.2 Measured fundamental pulse autocorrelation shown on a logarithmic scale.....67

3.3 Measured SH pulse spectrum shown on a linear scale. 68

3.4 Measured SH pulse autocorrelation shown on a logarithmic scale. 69

3.5 SHG conversion efficiency vs. average power at 1.56 μm. 71

3.6 Approximation to the saturated conversion energy efficiency for $sech^2$ pulses and Gaussian beams. 72

3.7 Experimental apparatus for demonstrating pulse compression during chirped-QPM SHG. 73

3.8 Autocorrelation traces of the fundamental and SH pulses at maximum compression.....75

3.9 Input and output autocorrelation widths vs. the chirp of the input pulse. 76

3.10 Efficiency plotted against delay line dispersion. 78

3.11 Schematic of a simple fiber-CPPLN chirped pulse amplification system.....79

3.12 Average power SHG conversion efficiency. 80

4.1 Schematic of the OPG process. 86

4.2 Nearly-degenerate OPG threshold for bulk PPLN devices with optimum length. 89

4.3 Experimental setup for demonstration of 54-nJ-threshold OPG in bulk PPLN.....91

4.4 OPG conversion efficiency in bulk PPLN. 91

4.5 Output signal and idler wavelengths for bulk PPLN OPG. 92

4.6 Theoretical OPG threshold for APE-PPLN waveguide devices with optimum length. ..96

4.7 Integrated structure for robust coupling of pump light into a parametric frequency conversion waveguide device. 98

4.8 Conversion efficiency and pump transmission for waveguide-OPG.....99

4.9 Wavelength tuning of waveguide-OPG device. 100

Chapter 1:Introduction

1.1 Motivation

Ultrashort-pulse lasers are, in many ways, the ideal light source for diverse applications. Examples of these applications include precision-machining[1-4], multi-photon microscopy[5] of biological tissues[6-10], opthamological surgery[11], other medical applications[12,13], time-division-multiplexed (TDM) communications[14] and time-domain spectroscopy[15-17]. Lasers can provide high brightness and high intensities, they can exhibit high spectral purity and they can be focused precisely. In addition to these general capabilities, ultrashort-pulse lasers can provide pulse durations ranging from ~ $5x10^{-15}$ seconds[18,19] through the picosecond (10^{-12} seconds) regime.

Various types of ultrashort-pulse lasers can produce useful output over much of the UV through far-infrared electromagnetic spectrum. However, for many applications, most of these types of lasers are impractical. Many laser systems (gas, chemical, dye, free-electron, etc...) are clumsy, unreliable, inefficient and/or expensive.

Only the injection diode laser has none of these problems. Unfortunately, practical diode lasers are only commercially available over a limited range of near-infrared wavelengths, and with limited output brightness. While substantial progress on extracting ultrashort pulses directly from diode lasers[20,21] has been made in recent years, many of the systems which have been demonstrated thus far have suffered from extremely low power levels and/or the same problems listed above for non-diode lasers.

Diode-pumping of solid state lasers can, with relative simplicity, provide alternate wavelengths with greater brightness and further improved performance than can be obtained directly from diodes. Indeed, one of the more attractive capabilities of several diode-pumped solid-state laser systems is the generation of high-quality ultrashort optical pulses.

Two particularly appealing ultrashort-pulse laser technologies are diode-pumped Cr:LiSAlF/LiSGaF[9,22-24] and diode-pumped erbium-fiber[25-27]. Both material systems offer milliwatt-level femtosecond pulses with electrical-to-optical conversion efficiencies of several percent. Hero experiments have pushed these limits to watt-level[28] average powers and μJ pulse energies[29]; electrical-to-optical conversion efficiencies in the 10's of percent range should be possible. However, despite their appeal, these and other ultrashort-pulse laser systems offer only limited selections of output wavelengths. Many applications require wavelengths which are currently unavailable from practical systems.

Nonlinear optical frequency conversion is often used to extend the useful wavelength range of available laser sources. However, in many cases, inadequate properties of conventional nonlinear materials have prevented the application of frequency conversion to low power sources such as diode-pumped fiber lasers. Recent advances in nonlinear materials, particularly that of the quasi-phasematching (QPM) technique, have enabled the generation of an increasing range of wavelengths with improved efficiencies and with lower power laser sources. Previous work on QPM frequency conversion has focused on continuous-wave (CW) or nanosecond-pulse lasers, while the work described in this dissertation focuses on the ultrashort-pulse regime.

1.2 Nonlinear optical frequency conversion

In general, when one or more intense waves pass through an optically nonlinear material, they mix with each other and with themselves. This mixing process can generate waves at sum, difference and harmonic frequencies. It is conventional[30] to describe these mixing phenomena using a Taylor expansion of the material polarization response, $\boldsymbol{P}$, to the applied (optical) electric field, $\boldsymbol{E}$.

$$\boldsymbol{P} = \varepsilon_0[\chi^{(1)}\boldsymbol{E} + \chi^{(2)}\boldsymbol{E}^2 + \chi^{(3)}\boldsymbol{E}^3 + \ldots]. \tag{1.1}$$

The polarization acts as a driving term in Maxwell's equations for electromagnetic wave propagation. The first-order term in equation (1.1), which is related to the phase velocity, is responsible for all of linear optics, including refraction, reflection, diffraction and dispersion.

The second-order term describes the phenomena which are studied in this dissertation. This term vanishes for materials which posses inversion symmetry, but can have substantial magnitude in materials such as lithium niobate (which is used for all of the experimental work described in this dissertation). The third-order term results in several technologically important (though not always desirable) effects such as self-focusing, self-phase modulation, 4-wave mixing, soliton formation and optical switching. Several good texts[31,32] cover the theory of nonlinear optics.

We now consider only the second-order term and assume a monochromatic input field at the (fundamental) frequency ω. The material polarization, $\boldsymbol{P}$, will then have Fourier components at frequencies 0, ω and 2ω. The component at frequency 2ω represents second harmonic generation (SHG). In the related process of sum frequency generation (SFG), two inputs at frequencies $\omega+\Delta$ and $\omega-\Delta$ combine to generate an output at frequency 2ω. These effects are the subject of chapters 2 and 3 of this dissertation.

The efficiency, η, of SHG for plane-wave inputs, neglecting depletion of the fundamental field and neglecting dispersion, can be written in the form

$$\eta = \frac{I_{2\omega}}{I_{\omega}} = \frac{8\pi^2 d_{eff}^2}{n^2 c\varepsilon_0 \lambda_{\omega}^2} I_{\omega} L^2, \tag{1.2}$$

where I_{ω} and $I_{2\omega}$ are the intensities at the fundamental and second harmonic (SH) frequencies, L is the length of the nonlinear material, d_{eff} is the material's nonlinear coefficient and λ_{ω} is the vacuum wavelength at the fundamental frequency. We note that, in addition to the nonlinear coefficient, the fundamental intensity and the length of the nonlinear material are also important parameters in determining the efficiency of the SHG interaction. Other frequency conversion processes obey similar efficiency scaling rules. We shall see in section 1.5, and again in chapter 2, that for finite aperture beams I_{ω} and L are intimately connected by diffraction effects. This connection has qualitative effects on the efficiency in real experimental situations

1.3 Quasi-phasematching

The above discussion of nonlinear optical frequency conversion, by neglecting dispersion, assumed perfect phase velocity matching between all of the interacting waves. Because of material dispersion (all materials are dispersive to some extent), phase velocity matching rarely occurs accidentally. A non-zero phase mismatch limits the interaction length to the distance over which the interacting waves remain in phase with each other. This distance is called the "coherence length," or L_c. Because, in practice, L_c is typically a few μm to a few hundred μm, non-phasematched interactions are usually not efficient.

Conventional nonlinear materials rely on natural birefringence to compensate for this phase velocity mismatch, limiting the choices of materials and polarizations which can be used for frequency conversion. Quasi-phasematching[33] (QPM), proposed[30] in 1962 and first demonstrated[34-37] in 1976, provides an alternative set of material requirements. Rather than requiring the existence of an appropriate amount of birefringence, QPM requires the existence of a fabrication technology which enables microstructuring of the nonlinear optical properties of a material.

To understand QPM, we first consider frequency conversion in non-phasematched materials. In the first coherence length of material, a weak output wave is generated. In the second coherence length of material, the nonlinear polarization interferes destructively with this free wave, exactly cancelling it. Hence, the power in the generated wave oscillates with distance between zero and the power generated in one coherence length. This oscillatory behavior is shown in figure 1.1.

In its simplest implementation, QPM uses a periodic modulation of the nonlinear susceptibility to compensate for the material dispersion. Each time the waves drift out of phase by π, the sign of the nonlinear coefficient (and therefore the nonlinear polarization) is switched. Therefore, the nonlinear polarization is never allowed to interfere destructively with the generated wave. The generated wave grows monotonically with distance, though, on average, not as quickly as for the phasematched case.

For the case of mth-order QPM-SHG, the period required for the modulation of the nonlinear coefficient, $\Lambda_{QPM} = 2mL_c$, is given by

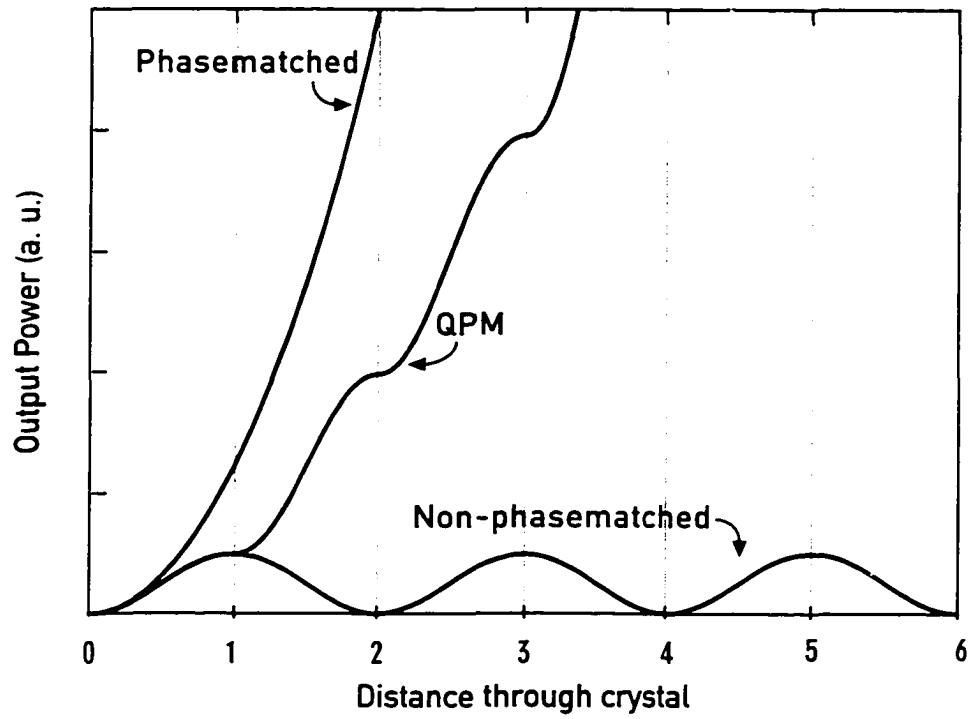

Figure 1.1: Comparison of non-phasematched, phasematched and quasi-phasematched frequency conversion. The distance through the material is normalized to coherence lengths, L_c.

$$\Lambda_{QPM} = \frac{m\lambda_1}{2|n_2 - n_1|}, \tag{1.3}$$

where λ_1 is the fundamental wavelength, n_1 is the fundamental refractive index and n_2 is the SH refractive index. Given the correct grating period, QPM allows for interactions between any wavelengths within a material's transparency range, allows use of non-birefringent materials, and eliminates constraints on polarization - thereby enabling use of the large nonlinear coefficients available for interactions between parallel electric fields. The availability of large nonlinear coefficients more than makes up for the $(2/m\pi)^2$ reduction in efficiency which is depicted in figure 1.1. The advantages of QPM described so far constitute engineerability and quantitative improvements (in efficiency and/or accessible wavelengths) over conventional phasematching techniques.

As will be shown in this thesis, QPM can also enable exploitation of phenomena which are not possible with conventional phasematching techniques. The opportunities presented by the use of aperiodic QPM-gratings are introduced in section 1.6.

1.4 Ultrashort pulse concepts

For many applications, ultrashort pulses are valuable because of two of their intrinsic properties. One is their obvious use in systems which temporally resolve extremely fast phenomena. Another is the very large peak optical powers that are provided, while keeping average powers low. This second property relates directly to nonlinear frequency conversion.

As we saw in section 1.2, high optical intensity (i.e. high power) is required for efficient nonlinear frequency conversion. Therefore, frequency conversion naturally favors ultrashort-pulse lasers over continuous-wave (CW) lasers of the same average power. However, as we shall see shortly, there are limits to how far this line of reasoning can be taken.

Ultrashort laser pulses intrinsically have wide bandwidth. For a pulse with duration τ, the minimum possible bandwidth is approximately $1/\tau$. The bandwidth of a pulse with a 100 fs duration must be at least 10^{13} Hz, which corresponds to a wavelength spread of approximately 10 nm for near-infrared wavelengths. Figure 1.2 compares CW and ultrashort-pulse optical waves in both the time and frequency domains.

When an ultrashort pulse propagates through a dispersive material (all materials are dispersive to some extent), different frequency components experience different phase velocities. It is convenient to describe the propagation of the pulse in terms of three quantities: the phase velocity of the carrier (typically the center) frequency of the pulse, the group velocity of the pulse envelope and the group velocity dispersion (GVD), which causes pulse spreading. Figure 1.3 details the relevant velocities of a pulse propagating without GVD. A formal discussion of group velocity can be found in Siegman.[38]

Group velocity dispersion is important for pulses with sufficiently large bandwidths and in sufficiently dispersive materials. When different spectral portions of a pulse experience significantly different group velocities, they will gradually spread apart from each other. When the spectral components of a pulse are temporally dispersed, the pulse is called "chirped." Chirping (or stretching) of a pulse using GVD is shown in figure 1.4. Depending on the sign of the

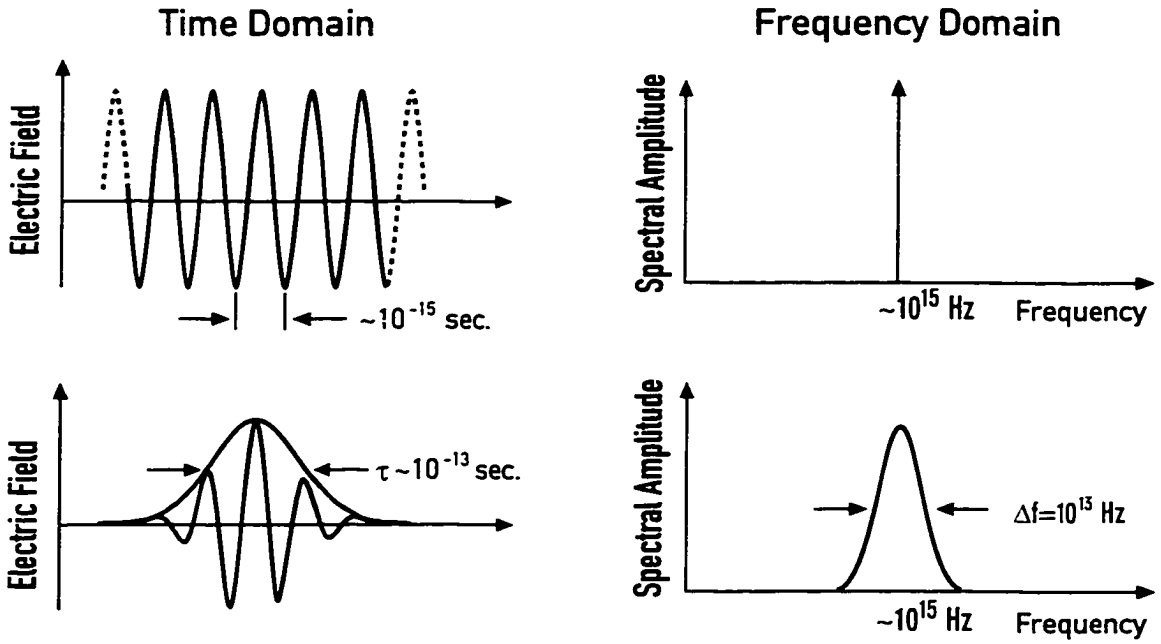

Figure 1.2: Continuous-wave (CW) and ultrashort-pulse optical waves in both the time and frequency domains. While an ideal CW wave has zero bandwidth, an ultrashort pulse with duration τ has a minimum bandwidth of approximately $1/\tau$.

GVD, it can either add or remove chirp from a pulse, as shown in figure 1.4. Several types of dispersive systems are routinely used for pulse stretching and compression.[39-43] Third-order nonlinear effects, when combined with dispersive systems, are also routinely used for pulse compression.[44,45]

1.5 Ultrashort pulse frequency conversion concepts

The concept of group velocity is very important for frequency conversion of ultrashort pulses. Nonlinear crystals used in CW applications typically have lengths of several cm. However, an ultrashort pulse with a duration of 100 fs only has a physical dimension of 30 μm (or less in materials with a high refractive index). The relative position of the various interacting pulse envelopes, therefore, becomes important.

Figure 1.6 depicts SHG of ultrashort pulses. The light generated in the crystal will propagate at a group velocity which is, in general, not the same as that of the input light. The mis-

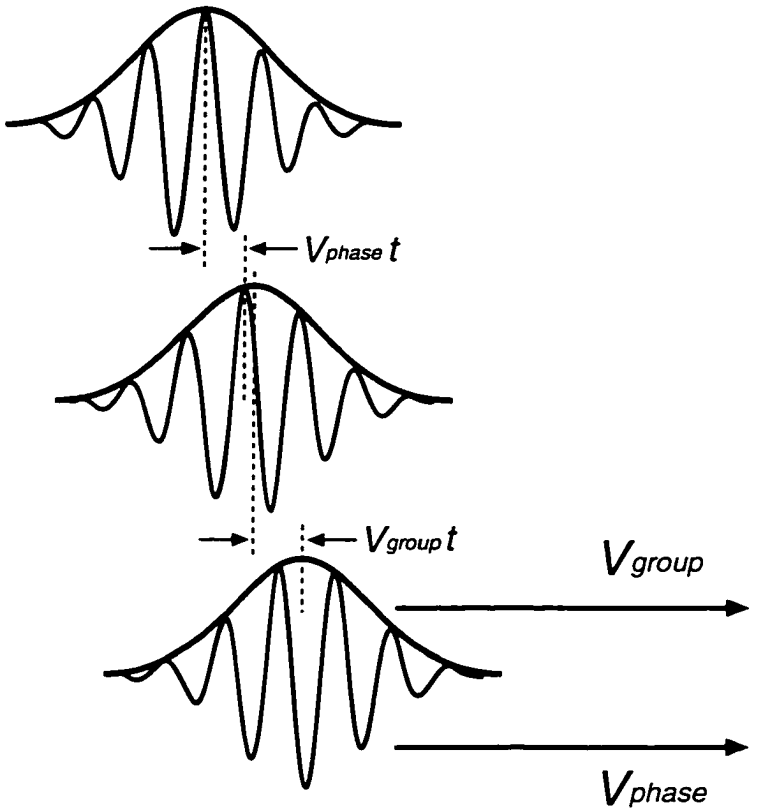

Figure 1.3: An ultrashort pulse propagates with two characteristic velocities. The phase-fronts propagate with the phase velocity of the carrier frequency, while the pulse envelope propagates at the group velocity. In the example shown here, the pulse envelope is travelling faster than the phase-fronts.

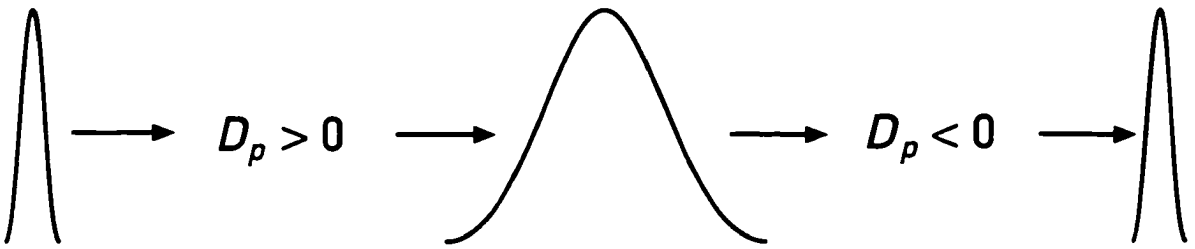

Figure 1.4: A dispersive system can be used to either stretch or compress a pulse, depending on the relative sign of the system dispersion and the pulse chirp.

match between the group velocities of the interacting pulses, therefore, leads to a maximum interaction distance. The light generated at the beginning of the crystal will walk off of the

input light after propagating some distance, which is called the "group velocity walkoff length". This length can be on the order of several μm to several cm for many fs and ps interactions in technologically important nonlinear materials.

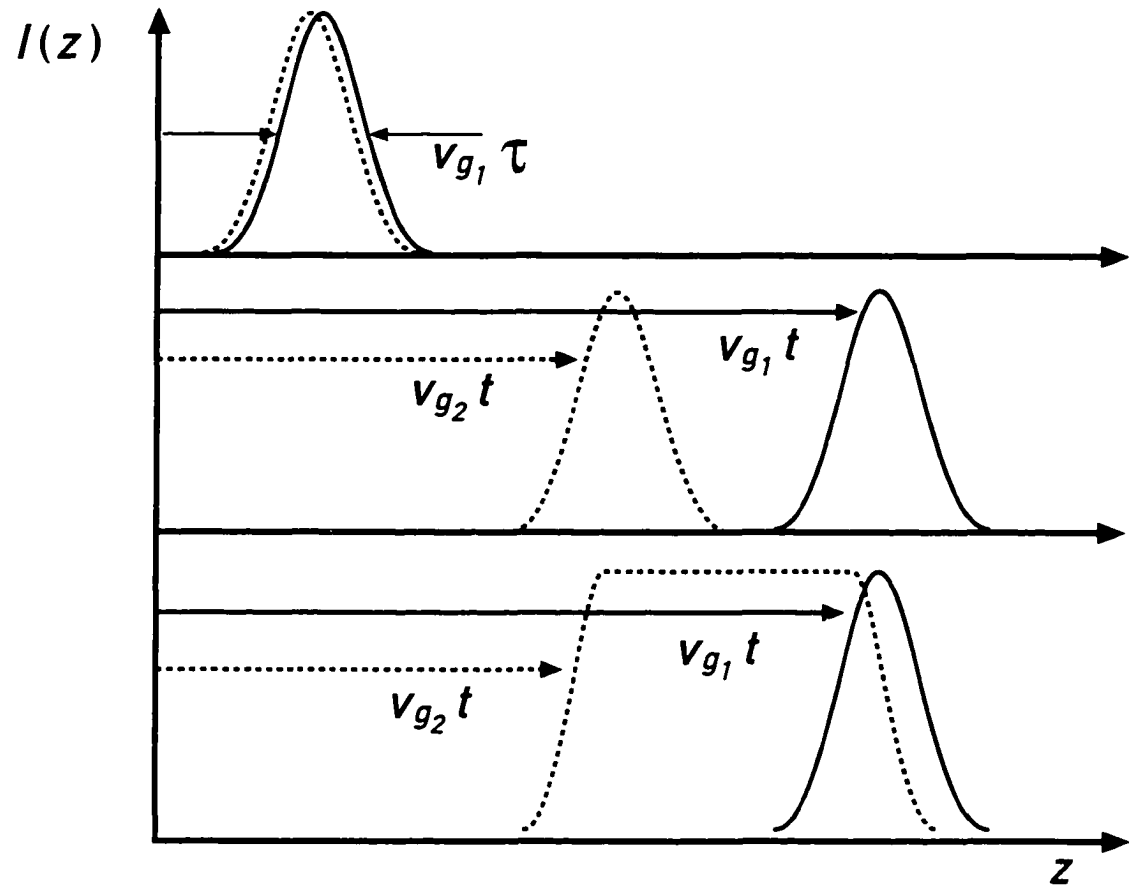

Figure 1.5: Summary of effects related to group velocity mismatch during nonlinear optical frequency conversion. The top curve shows an input pulse generating an output pulse with similar pulse shape and duration. The middle curve shows that, after propagating some distance, the input and output pulses no longer overlap and no longer can interact. The bottom curve shows the distorted output pulse which is generated in excessively long nonlinear crystals.

When nonlinear crystals with lengths which exceed the group velocity walkoff length are used, a distorted output pulse is typically generated. This stretched output pulse is generated by superimposing output pulses generated in different positions in the nonlinear crystal and delayed different amounts by the group velocity mismatch (GVM). This stretched output

pulse usually differs from the stretched pulses described in section 1.4 in that it is not chirped, and therefore not compressible.

1.6 Pulse compression with chirped QPM-SHG

The above discussion assumes uniform (or periodic QPM) nonlinear media. If the material has a chirped QPM grating, then an effective GVD, similar to that described in section 1.4, can be generated during second harmonic generation (SHG). This effective GVD is a result of the interplay of two phenomena: group velocity mismatch between the fundamental and second harmonic pulses, intrinsic to the nonlinear material, and spatial localization of second harmonic conversion of particular frequency components, a property of aperiodic QPM gratings.

Group velocity walkoff implies that the second harmonic field generated at each spatial position in the nonlinear medium undergoes a particular time delay relative to the fundamental pulse, as observed at the output of the material. In other words, GVM maps position to time delay.

In section 1.3 we found that with QPM, the grating period determines which wavelength can be doubled. Therefore, with SHG in aperiodic QPM gratings, different spatial regions of the nonlinear material quasi-phasematch doubling of different frequency components of the fundamental pulse. In other words, aperiodic-QPM maps position to frequency components of a pulse.

The phenomena described above are summarized in figure 1.6, which shows the evolution of two spectral components of fundamental and SH pulses in a chirped QPM grating. We consider two frequency components (at the blue [checkerboard] and red [solid] ends of its spectrum) of an input pulse. At time t_1, the input pulse has not yet entered the nonlinear material. At time t_2, the input pulse overlaps with a region of a chirped QPM grating which quasi-phasematches SHG of the blue frequency component. At time t_3, the input pulse overlaps with a region of a chirped QPM grating which quasi-phasematches SHG of the red frequency component. However, at time t_3, the SH pulse at the blue end of the SH spectrum (which was generated at time t_2) has lagged behind the fundamental, and therefore lags behind the red SH frequency component. At time t_4, the input and SH pulses have exited the

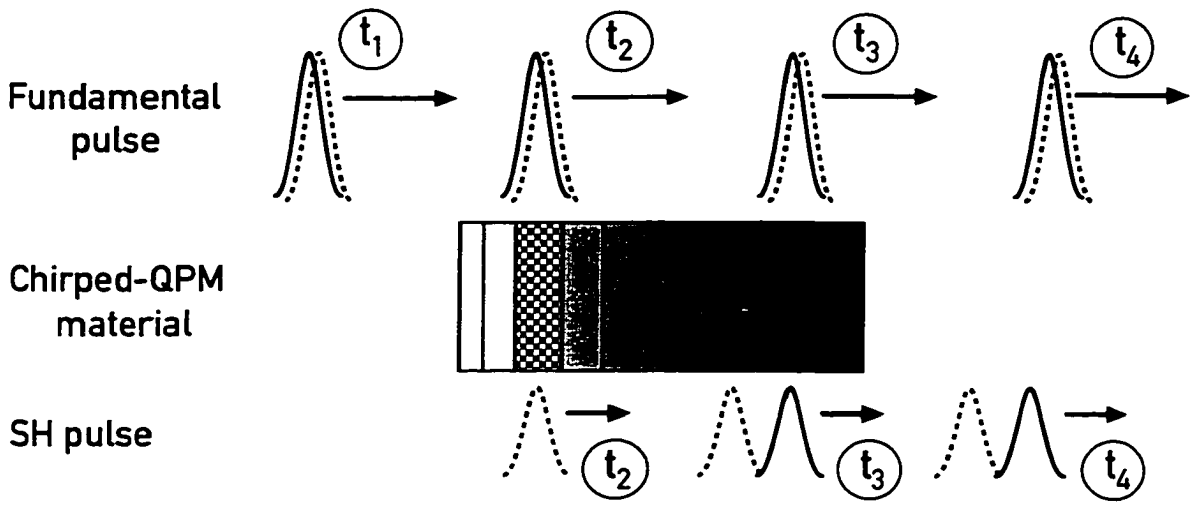

Figure 1.6: Evolution of two (shown as checkerboard and solid) frequency components of fundamental and SH pulses in a chirped QPM grating at times t_1- t_4. A time delay between the frequency components of the SH, relative to that of the fundamental, is produced by a combination of GVM between the fundamental and second harmonic pulses and spatial localization of second harmonic conversion of particular frequency components.

nonlinear material, and the SH pulse retains the time delay between its red and blue components. Similar arguments show that the same crystal oriented in the reverse direction will generate the opposite delay between the red and blue components of the pulse.

If the fundamental pulse is chirped, then the frequency components "picked-out" by regions of the QPM grating correspond to temporal slices. By choosing the location of each spatial frequency component of the grating, one determines the time delay each temporal slice of the fundamental pulse experiences relative to the second harmonic. If the chirp rate (aperiodicity) of the QPM grating exactly matches the chirp of the input pulse, then the generated output pulse has all of its spectral components coincident in time, as shown in figure 1.7. It is therefore compressed.

It is clear from this time-domain argument that the chirped-QPM nonlinear material must be longer than the walkoff length for the compressed SH output pulse. More precisely, the material must be at least as long as the walkoff length for the chirped fundamental pulse. This minimum material length arises from the need for the SH pulse to walk through the entire fundamental pulse, picking up frequency components along its way. We can also see that the orientation of the chirped-QPM grating must match the sign of the chirp on the fundamental

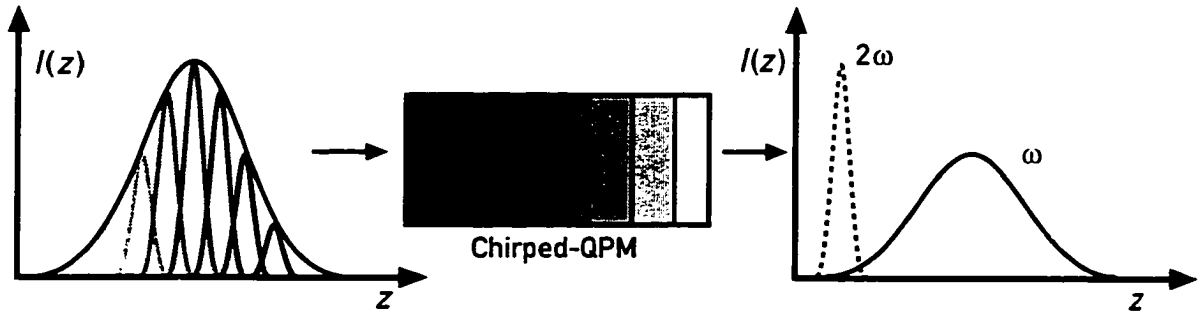

Figure 1.7: Mechanism of pulse compression during SHG in a chirped-QPM grating. Note that the fundamental pulse exiting the material has not been compressed, whereas the SH pulse is compressed relative to the fundamental.

pulse. Finally, we note that, with the opposite orientation, chirped-QPM gratings can be used to stretch pulses.

1.7 Overview of this dissertation

This dissertation describes most of the basic issues which govern quasi-phasematched frequency conversion of ultrashort optical pulses. In particular, the topics of bandwidth limits, pulse broadening, material requirements and conversion efficiency are both analyzed theoretically and investigated experimentally. This dissertation also demonstrates that QPM materials such as PPLN make possible practical coherent sources that are pumped by low-power diode-pumped fiber-lasers. Once such practical ultrashort-pulse laser system has recently been commercialized.[46]

Chapter 2 develops the theory of QPM-SHG for ultrashort pulses in the presence of arbitrary material dispersion at the SH frequency, with group velocity mismatch between the fundamental and SH frequencies and with arbitrary QPM grating designs. A convenient transfer function interpretation is used to explain phenomena such as pulse broadening and pulse compression, and to derive general expressions for efficiency. A novel pulse compression process is analyzed in detail.

Chapter 3 summarizes the results of experiments which confirm many of the predictions of Chapter 2. Namely, it is shown that SHG using bulk PPLN as the nonlinear material can be very efficient compared to that which can be obtained with conventional nonlinear materials.

Also, pulse compression during SHG in chirped QPM structures is shown to be simple, engineerable and efficient. Finally, a practical system which takes advantage of this pulse compression phenomenon is demonstrated.

Chapter 4 describes tunable optical parametric generation. It is shown theoretically and experimentally that very low OPG thresholds can be obtained with bulk PPLN. A waveguide-PPLN device with an extremely low threshold is also demonstrated.

Chapter 5 summarizes the above results and describes some potential future directions for extending the work discussed in this dissertation. Appendices provide an alternate derivation of some of the theoretical results in Chapter 2 and summarize notation.

References

[1]P. Bado and X. Liu, "Compact and robust ultrafast lasers for materials microprocessing," to be published in Commercial Applications of Ultrafast Lasers, Proceedings of the SPIE, volume 3269, (Society of Photo-Optical Instrumentation Engineers), (1998).

[2]P. P. Pronko, P. A. Van Rompay and S. Sato, "Materials synthesis and processing with ultrafast lasers," to be published in Commercial Applications of Ultrafast Lasers, Proceedings of the SPIE, volume 3269, (Society of Photo-Optical Instrumentation Engineers), (1998).

[3]B. C. Stuart, H. T. Nguyen and M. D. Perry, "Femtosecond laser material processing," to be published in Commercial Applications of Ultrafast Lasers, Proceedings of the SPIE, volume 3269, (Society of Photo-Optical Instrumentation Engineers), (1998).

[4]L. Bromley and J. Weston A. Hankla, "Practical considerations for industrial ultrafast lasers," to be published in Commercial Applications of Ultrafast Lasers, Proceedings of the SPIE, volume 3269, (Society of Photo-Optical Instrumentation Engineers), (1998).

[5]W. Denk, J. H. Strickler and W. W. Webb, "Two-photon laser scanning florescence microscopy," Science **248**, 73-76 (1990).

[6]D. L. Woskosin and J. G. White, "Multiple-photon excitation florescence applied to embryo development," to be published in Commercial Applications of Ultrafast Lasers, Proceedings of the SPIE, volume 3269, (Society of Photo-Optical Instrumentation Engineers), (1998).

[7]W. Denk, K. R. Delaney, A. Gelperin, D. Kleinfeld, B. W. Strowbridge, D. W. Tank and R. Yuste, "Anatomical and functional imaging of neurons using 2-photon laser scanning microscopy," Journal of Neuroscience Methods **54**, 151-162 (1994).

[8]S. Maiti, J. B. Shear, R. M. Williams, W. R. Zipfel and W. W. Webb, "Measuring serotonin distribution in live cells with three-photon excitation," Science **275**, 530-532 (1997).

[9]K. Svoboda, W. Denk and W. Knox, "Two-photon-excitation scanning microscopy of living neurons with a saturable Bragg reflector mode-locked diode-pumped Cr:LiSrAlFl laser," Optics Letters **21**, 1411 (1996).

[10]D. W. Piston, B. R. Masters and W. W. Webb, "Three-dimensionally resolved NAD(P)H cellular metabolic redox imaging of the *in situ* cornea with two-photon excitation laser scanning microscopy," Journal of Microscopy **178**, 20-27 (1995).

[11]R. M. Kurtz and T. Juhasz, "Opthalmic applications of ultrafast lasers," to be published in Commercial Applications of Ultrafast Lasers, Proceedings of the SPIE, volume 3269, (Society of Photo-Optical Instrumentation Engineers), (1998).

[12]E. A. Wachter, W. P. Partridge Jr., W. G. Fisher and H. C. Dees, "Simultaneous two-photon excitation of photodynamic therapy agents," to be published in Commercial Applications of Ultrafast Lasers, Proceedings of the SPIE, volume 3269, (Society of Photo-Optical Instrumentation Engineers), (1998).

[13]H. Nathel, "Overview of medical applications of ultrafast technology," to be published in Commercial Applications of Ultrafast Lasers, Proceedings of the SPIE, volume 3269, (Society of Photo-Optical Instrumentation Engineers), (1998).

[14]L. Kazovsky, S. Benedetto and A. Willner, *Optical Fiber Communication Systems* (Artech House, Norwood, MA., 1996).

[15]A. H Zewail, "Ultrafast lasers in chemistry and biology," in International Quantum Electronics Conference, Vol. 9, 1994 OSA Technical Digest Series (Optical Society of America, Washington, D. C.), (1994).

[16]A. H. Zewail, "Femtochemistry: ultrafast dynamics of the chemical bond," (World Scientific, River Edge, NJ., 1994).

[17]D. M. Dantus, R. M. Bowman and A. H. Zewail "Femtosecond laser observations of molecular vibration and rotation," Nature **343**, 737-789 (1990).

[18]S. Sartania, Z. Cheng, M. Lenzner, G. Tempea, C. Spielmann, F. Krausz and K. Ferencz, "Generation of 0.1-TW 5-fs optical pulses at a 1-kHz repetition rate," Optics Letters **22**, 1562-1564 (1997).

[19]M. Nisoli, S. Stagira, S. De Silvestri, O. Scelto, S. Sartania, Z. Cheng, M. Lenzner, C. Spielmann and F. Krausz, "A novel nigh-energy pulse compression system: generation of multigigawatt sub-5-fs pulses," Applied Physics B (Lasers and Optics) **B65**, 189-196 (1997).

[20]P. J. Delfyett, L. T. Florez, N. Stoffel, T. Gmitter, N. C. Andreadakis, Y. Silberberg, J. P.

Heritage and G. A. Alphonse, "High-power ultrafast laser diodes," IEEE Journal of Quantum Electronics **QE-28**, 2203-2219 (1992).

[21]P. J. Delfyett, S. Gee, H. Shi, J. Connolly and G. A. Alphonse, "Diamond shaped semiconductor amplifiers for high-power external cavity modelocked diode lasers," to be published in Commercial Applications of Ultrafast Lasers, Proceedings of the SPIE, volume 3269, (Society of Photo-Optical Instrumentation Engineers), (1998).

[22]R. Mellish, S. C. W. Hyde, N. P. Barry, R. Jones, P. M. W. French, J. R. Taylor, C. J. Van der Poel and A. Valster, "All-solid-state diode-pumped Cr:LiSAF femtosecond oscillator and regenerative amplifier," Applied Physics B (Lasers and Optics) **B65**, 221-226 (1997).

[23]I. T. Sorokina, E. Sorokin, E Wintner, A. Cassanho, H. P. Tenssen, and R. Szipocs, "14-fs pulse generation in Kerr-lens mode-locked prismless Cr:LiSGaF and Cr:LiSAF lasers: observation of pulse self-frequency shift," Optics Letters **22**, 1716-1718 (1997).

[24]D. Kopf, K. J. Weingarten, G. Zhang, M. Moser, M. A. Emanuel, R. J. Beach, J. A. Skidmore and U. Keller, "High-average-power diode-pumped femtosecond Cr:LiSAF lasers," Applied Physics B (Lasers and Optics) **B65**, 235-243 (1997).

[25]B. C. Collings, K. Bergman, S. T. Cundiff, S. Tsuda, J. N. Kutz, J. E. Cunningham, W. Y. Jan, M. Koch and W. H. Knox, "Short cavity erbium/ytterbium fiber lasers mode-locked with a saturable Bragg reflector," IEEE Journal of Selected Topics in Quantum Electronics **3**, 1065-1075 (1997).

[26]M. E. Fermann, A. Galvanauskas, G. Sucha and D. Harter, "Fiber-lasers for ultrafast optics," Applied Physics B (Lasers and Optics) **B65**, 259-275 (1997).

[27]M. E. Fermann, D. Harter, J. D. Minelly, and G. G. Vienne, Optics Letters **21**, 967 (1996).

[28]A. Galvanauskas, M. E. Fermann, D. Harter, J.D. Minelly, G. G. Vienne, and J. E. Caplen, "Broad-area diode-pumped 1 Watt femtosecond fiber system," in Conference on Lasers and Electro-Optics, Vol. 9, 1996 OSA Technical Digest Series (Optical Society of America, Washington, D.C.), 495-496, (1996).

[29]A. Galvanauskas, M. E. Fermann, P. Blixt and D. Harter, "Microjoule ultrashort pulses from a hybrid diode laser-fiber amplifier system," in Conference on Lasers and Electro-

Optics, Vol. 8, 1994 OSA Technical Digest Series (Optical Society of America, Washington, D.C.), 72-73, (1994).

[30]J. A. Armstrong, N. Bloembergen, J. Ducuing, and P. S. Pershan, "Interactions between light waves in a nonlinear dielectric," Physical Review **127**, 1918 (1962).

[31]H. Rabin and C. L. Tang, "Quantum Electronics: A Tretise," in *Nonlinear Optics, Part B* (Academic Press, New York, 1975).

[32]P. N. Butcher and D. Cotter, *The elements of nonlinear optics* (Cambridge University Press, Cambridge, 1990).

[33]M. M. Fejer, G. A. Magel, D. H. Jundt, and R. L. Byer, "Quasi-Phasematched Second Harmonic Generation: Tuning and Tolerances," IEEE Journal of Quantum Electronics **28**, 2631 (1992).

[34]A. Szilagyi, A. Hordvik and H. Schlossberg, "A quasi-phasematching technique for efficient optical mixing and frequency doubling," Journal of Applied Physics **47**, 2025-2032 (1976).

[35]M. S. Piltch, C. D. Cantrell and R. C. Sze, "Infrared second harmonic generation in nonbirefringent cadmium telluride," Journal of Applied Physics **47**, 3514-3517 (1976).

[36]M. Okada, K. Takizawa and S. Ieiri, "Second harmonic generation by periodic laminar structure of the nonlinear optical crystal," Optics Communications **18**, 331-334 (1976).

[37]D. E. Thompson, J. D. McMullen and D. B. Anderson, "Second harmonic generation in GaAs "stack of plates" using high power CO_2 laser radiation," Applied Physics Letters **29**, 113-115 (1976).

[38]A. E. Siegman, *Lasers* (University Science Books, Mill Valley, CA., 1986).

[39]J. A. Giordmaine, M. A. Duguay and J. W. Hansen, "Compression of optical pulses," IEEE Journal of Quantum Electronics **QE-4**, 252 (1968).

[40]E. Treacy, "Optical pulse compression with diffraction gratings," IEEE Journal of Quantum Electronics **QE-5**, 454 (1969).

[41]R. L. Fork, O. E. Martinez and J. P. Gordon, "Negative dispersion using a pair of prisms," Optics Letters **9**, 150-152 (1984).

[42]F. J. Duarte and J. A. Piper, "Dispersion theory of multiple-prism beam expanders for

pulsed dye lasers," Optics Communications **43**, 303 (1982).

[43]O. E. Martinez, "3000 times grating compressor with positive group velocity dispersion: Application to fiber compensation in 1.3-1.6 μm region," IEEE Journal of Quantum Electronics **QE-23**, 59 (1987).

[44]L. F. Mollenauer, R. H. Stolen, J. P. Gordon and W. L. Tomlinson, "Extreme picosecond pulse narrowing by means of soliton effect in single-mode optical fibers," Optics Letters **8**, 289 (1983).

[45]G. P. Agrawal, *Nonlinear Fiber Optics*, 2 ed. (Academic Press, San Diego, 1995).

[46]Femtolite 780 fiber laser spec sheet, (IMRA America, Ann Arbor, MI.,).

Chapter 2: Theory of quasi-phasematched ultrashort-pulse second harmonic generation

2.1 Introduction

In this chapter, we develop a theory of phasematched or quasi-phasematched ultrashort-pulse second harmonic generation in the undepleted-pump approximation. A frequency domain analysis is used because it allows inclusion of arbitrary material dispersion properties. (A less general analysis in the time domain is treated in Appendix A.) We find that when GVD at the fundamental frequency can be neglected, a simple transfer function relationship describes the SHG process for arbitrary input pulses. The SHG transfer function depends only on material properties and the QPM grating design. Less general forms of this transfer function for phasematched and quasi-phasematched interactions were derived by Glenn[1] in 1969 and Sidick[2] in 1996, respectively.

In this chapter, we apply the SHG transfer function relationship to two important cases. First, we examine quantitatively the trade-off between efficiency and pulse distortion when choosing the crystal length for ultrashort-pulse SHG. Second, we show that chirped QPM gratings can be designed to generate transform-limited SH output pulses from arbitrarily chirped fundamental input pulses. To put these theoretical results into perspective, we analyze the efficiency for ultrashort-pulse SHG that one can expect from various nonlinear materials with transform-limited input pulses and for chirped-QPM materials with chirped input pulses.

There has been substantial work in the theory of ultrashort-pulse nonlinear optics. Early experimental work[3] identified the importance of group-velocity effects in SHG of ultrashort pulses. Subsequent theoretical work[1] quantified these effects using a frequency-domain analysis. Akhmanov wrote several reviews of early work in the field[4,5], considering mostly time-domain analyses. More recent work by Sidick[2,6-8] considered quasi-phasematched interac-

tions and included many numerical simulations of thin-film interactions. However, no prior work in the field has treated SHG of chirped pulses with aperiodic QPM gratings.

Aperiodic-grating QPM interactions have been studied both theoretically[9,10] and experimentally[11]. To date, all treatments have considered the case of tunable continuous-wave SHG. No prior work in the field has treated SHG of ultrashort pulses with aperiodic QPM gratings. This chapter develops a theoretical framework for treating such interactions and explores them in detail.

In sections 2.2 and 2.3, we derive a frequency-domain slowly-varying envelope equation which is different from the form often found in the literature, but valuable for analyzing interactions in the presence of arbitrary dispersion. In section 2.4, we specify our analysis to the case of SHG and discuss the form of the nonlinear polarization wave, including the case where GVD at the fundamental frequency can not be neglected. In section 2.5, we analyze the case of CW-SHG and discuss tuning curves. In section 2.6, we derive a general solution for undepleted-pump SHG in the presence of arbitrary material dispersion and arbitrary QPM gratings. We then find a simple transfer function relationship which applies when dispersion at the fundamental frequency is negligible. In sections 2.7 through 2.9, we consider ultrashort-pulse SHG with uniform nonlinear materials. In section 2.10, we discuss quasi-phasematching. In sections 2.11 and 2.12, we analyze the efficiency of SHG and compare various nonlinear materials. In sections 2.13 through 2.19, we analyze in detail the compression of ultrashort pulses using SHG in chirped QPM gratings.

2.2 Maxwell's Equations

All linear and nonlinear optical phenomena can be described fully by Maxwell's equations in the form

$$\nabla \times \boldsymbol{E}(\boldsymbol{r},t) = -\frac{d}{dt}\boldsymbol{B}(\boldsymbol{r},t) \text{ and} \tag{2.1}$$

$$\nabla \times \boldsymbol{H}(\boldsymbol{r},t) = \frac{d}{dt}\boldsymbol{D}(\boldsymbol{r},t), \tag{2.2}$$

where $\boldsymbol{E}(\boldsymbol{r},t)$, $\boldsymbol{B}(\boldsymbol{r},t)$, $\boldsymbol{H}(\boldsymbol{r},t)$ and $\boldsymbol{D}(\boldsymbol{r},t)$ are the full electric field, magnetic field, magnetic displacement and electric displacement vectors, respectively. (A table summarizing the notation used in this chapter is included in Appendix B.) We move to the frequency domain by taking the temporal Fourier transform of equations (2.1) and (2.2). In this thesis, we use the following notation: If $F(t)$ is a function, then $\hat{F}(\omega)$ is its temporal Fourier transform[12]. Henceforth the hat (^) symbol is used to denote Fourier domain quantities. We use the transform pair

$$\hat{F}(\omega) \equiv \int_{-\infty}^{\infty} F(t)\exp(-i\omega t)dt \text{ and} \tag{2.3}$$

$$F(t) = \frac{1}{2\pi}\int_{-\infty}^{\infty} \hat{F}(\omega)\exp(i\omega t)d\omega. \tag{2.4}$$

We note that ω represents optical radian frequencies. Maxwell's equations transform to

$$\nabla \times \hat{\boldsymbol{E}}(\boldsymbol{r}, \omega) = -i\omega\hat{\boldsymbol{B}}(\boldsymbol{r}, \omega) \text{ and} \tag{2.5}$$

$$\nabla \times \hat{\boldsymbol{H}}(\boldsymbol{r}, \omega) = i\omega\hat{\boldsymbol{D}}(\boldsymbol{r}, \omega). \tag{2.6}$$

Material properties are described by the frequency-domain constitutive relationships between displacement and field. For nonmagnetic media, we use $\hat{\boldsymbol{B}}(\boldsymbol{r}, \omega) = \mu_0\hat{\boldsymbol{H}}(\boldsymbol{r}, \omega)$. For nonlinear dielectrics, we use

$$\hat{\boldsymbol{D}}(\boldsymbol{r}, \omega) = \varepsilon_0\varepsilon(\omega)\hat{\boldsymbol{E}}(\boldsymbol{r}, \omega) + \widehat{\boldsymbol{P}_{NL}}(\boldsymbol{r}, \omega), \tag{2.7}$$

where $\widehat{\boldsymbol{P}_{NL}}(\boldsymbol{r}, \omega)$ is the electric nonlinear polarization component at frequency ω, $\varepsilon(\omega) = n^2(\omega)$ is the dielectric constant and n is the refractive index. In this thesis, we assume lossless materials and, therefore, purely real ε. We also assume media in which $\boldsymbol{D}(\boldsymbol{r},t)$ is parallel to $\boldsymbol{E}(\boldsymbol{r},t)$, and therefore that ε can be described with scalar, rather than tensor, quantities.

Assuming plane wave interactions with a propagation direction z, we obtain from equations (2.5)-(2.7) the one-dimensional frequency-domain scalar wave equation

$$\frac{\partial^2}{\partial z^2}\hat{E}(z,\omega) + k^2(\omega)\hat{E}(z,\omega) = -\mu_0\omega^2\widehat{P_{NL}}(z,\omega), \tag{2.8}$$

where we have written the **k**-vector in the medium as $k^2(\omega) = [\omega^2 \cdot \varepsilon(\omega)]/c^2$. The frequency dependence of this **k**-vector can be modeled by any appropriate dispersion relation. We note that in the case of linear media ($P_{NL} = 0$), solutions to equation (2.8) take the form $\hat{E}(z,\omega) = \hat{E}(z=0,\omega)\exp[\pm ik(\omega)z]$. This Fourier component corresponds in the time domain to traveling waves, $E(z,t) = \hat{E}(z=0,\omega)\exp(i[\omega t \pm k(\omega)z])$.

2.3 Frequency domain slowly-varying envelope equations

We now restrict this analysis to nonlinear interactions between fields with bandwidths that are small compared to their optical carrier frequency. This simplification allows us to derive a distinct pair of slowly varying envelope equations for the fundamental and second harmonic waves. Most of the analysis in this chapter will be general enough to accurately describe most wideband signals, but several specific results will be focused on the particular case of ultrashort pulses.

We begin by defining a spatial envelope, $\hat{A}(z,\omega)$, which contains both amplitude and phase information, for each frequency component of the electric field. We write the Fourier transform of the electric field in the form

$$\hat{E}(z,\omega) = \hat{A}(z,\omega)\exp[-ik(\omega)z], \tag{2.9}$$

which involves no loss of generality. We note that equation (2.9) is a critical step in the analysis of this chapter, as it serves to define the typical spatial envelope function, $\hat{A}(z,\omega)$. We therefore discuss several features of this definition here. We first note that $\hat{A}(z,\omega)$ is a complex quantity, defined for both positive and negative frequencies, ω. We also note that $k(\omega)$ is the frequency-dependent **k**-vector, not the **k**-vector evaluated at the carrier frequency of the pulse, as is commonly found in similar analyses in the literature. Here, $k(\omega)$ is a signed quantity such that $k(-\omega) = -k(\omega)$ and $k(\omega) > 0$ for $\omega > 0$. We also note that at $z = 0$, the spatial envelope is the same as the Fourier transform of the electric field,

$$\hat{E}(z = 0, \omega) = \hat{A}(z = 0, \omega). \tag{2.10}$$

The above definition of the field envelope, with a frequency-dependent **k**-vector, is not the typical envelope definition used in the ultrafast or nonlinear optics literature. (The typical envelope is defined in equation (2.52) and discussed in some detail in section 2.6.) However, the definition in equation (2.9) leads to a mathematically and physically more transparent analysis for cases where GVD at the fundamental frequency can not be neglected. The most important feature of this envelope is that it is defined in the frequency domain, rather than in the time domain. Also, the carrier frequency of a pulse is not factored out, but the effects of dispersion in linear dielectrics are factored out of the envelope, as is discussed in section (2.4).

It is instructive to relate this envelope to the electric field. Substituting equation (2.9) into equation (2.4), we may write any electric field in terms of $\hat{A}(z, \omega)$ as,

$$E(z, t) = \frac{1}{2\pi}\int_{-\infty}^{\infty} \hat{A}(z, \omega)\exp(i[\omega t - k(\omega)z])d\omega. \tag{2.11}$$

Alternatively, we may write $\hat{A}(z, \omega)$ in terms of the electric field

$$\begin{aligned}\hat{A}(z, \omega) &= \exp[ik(\omega)z]\int_{-\infty}^{\infty} E(z, t)\exp(-i\omega t)dt \\ &= \exp[ik(\omega)z]\hat{E}(z, \omega) \quad .\end{aligned} \tag{2.12}$$

To derive a simplified form of equation (2.28), we first differentiate equation (2.9) and find

$$\begin{aligned}\frac{\partial^2}{\partial z^2}\hat{E}(z, \omega) &= \exp[-ik(\omega)z]\frac{\partial^2}{\partial z^2}\hat{A}(z, \omega) \\ &\quad - 2ik(\omega)\exp[-ik(\omega)z]\frac{d}{dz}\hat{A}(z, \omega) - k^2(\omega)\hat{E}(z, \omega) \quad .\end{aligned} \tag{2.13}$$

We then make a slowly varying envelope approximation (SVEA) by assuming that the spatial derivative of the envelope is small compared to the **k**-vector, i.e. $\frac{d}{dz}\hat{A}(z, \omega) << k(\omega)$. Physically, we are assuming that $\hat{A}(z, \omega)$ changes negligibly over the distance of one optical wavelength. The SVEA allows us to drop the second spatial derivative in equation (2.13). Substituting into equation (2.8) gives

$$\frac{d}{dz}\hat{A}(z,\omega) = -i\frac{\mu_0\omega^2}{2k(\omega)}\widehat{P_{NL}}(z,\omega)\exp[ik(\omega)z], \tag{2.14}$$

where we note that $\widehat{P_{NL}}(z,\omega)$ is not an envelope quantity; rather, it contains the full spatial dependence of the nonlinear polarization wave and is the complex amplitude of its temporal Fourier transform.

2.4 Derivation of the SHG output field

We now recognizing that, for convenience, we may write the electric field as a sum of the field components at the fundamental (E_1) and second harmonic (E_2) frequencies. That is,

$$E(z,t) = E_1(z,t) + E_2(z,t) \text{ or} \tag{2.15}$$

$$\hat{E}(z,\omega) = \hat{E}_1(z,\omega) + \hat{E}_2(z,\omega). \tag{2.16}$$

We also decompose the electric field envelope analogously with equation (2.16) as

$$\hat{A}(z,\omega) = \hat{A}_1(z,\omega) + \hat{A}_2(z,\omega), \tag{2.17}$$

where $\hat{A}_1(z,\omega)$ and $\hat{A}_2(z,\omega)$ are the electric field envelopes for the fundamental pulse and second harmonic pulse, respectively. Substituting equation (2.17) into equation (2.14), and assuming that the fundamental and second harmonic spectra do not overlap, gives the following pair of frequency-domain SVEA equations

$$\frac{d}{dz}\hat{A}_i(z,\omega) = -i\frac{\mu_0\omega^2}{2k(\omega)}\widehat{P_{NL,i}}(z,\omega)\exp[ik(\omega)z], \tag{2.18}$$

where $i = 1, 2$. Note that equation (2.18) applies individually to each frequency component of the pulse envelopes. In order to solve this set of coupled partial differential equations we need to assume a form for the nonlinear polarization, $\widehat{P_{NL}}(z,\omega)$.

From now on, we assume that the overall conversion efficiency is low, and therefore, that there is no depletion of the fundamental (pump). In equation (2.18) for the fundamental

envelope, we set the nonlinear polarization, $\widehat{P_{NL}}(z, \omega = \omega_1)$, which drives pump depletion, to zero. We now have

$$\frac{d}{dz}\hat{A}_1(z, \omega) = 0 \text{ and} \tag{2.19}$$

$$\frac{d}{dz}\hat{A}_2(z, \omega) = -i\frac{\mu_0\omega^2}{2k(\omega)}\widehat{P_{NL}}(z, \omega)\exp[ik(\omega)z]. \tag{2.20}$$

We also assume a nonlinear material of length L and centered about $z = 0$. Then, by definition, $P_{NL} = 0$ for $|z| > L/2$.

We take a brief digression in this analysis to use the physically obvious solution of equation (2.19) to demonstrate some key properties of the envelope functions. The solution for the fundamental envelope is

$$\hat{A}_1(z, \omega) = \hat{A}_1(-L/2, \omega), \tag{2.21}$$

where $\hat{A}_1(-L/2, \omega)$ is the fundamental field envelope at the input facet of the nonlinear crystal. We note that, because the effects of dispersion are explicitly retained in the definition (2.9), the frequency-domain fundamental field envelope is independent of position within the crystal when nonlinear effects are neglected, even though the fundamental field experiences dispersion. We use the notation $\hat{A}_1(\omega) \equiv \hat{A}_1(-L/2, \omega)$ henceforth for simplicity. Again, expressed explicitly in the time domain for monochromatic input, we have traveling waves, $E_1(z, t) = \hat{A}_1(\omega)\exp(i[\omega t - k(\omega)z]) + \text{c.c.}$ For finite bandwidth fields, substituting $\hat{A}_1(z, \omega)$ from equation (2.21) into equation (2.11) gives the solution for the undepleted pump case

$$E_1(z, t) = \frac{1}{2\pi}\int_{-\infty}^{\infty}\hat{A}_1(\omega)\exp(i[\omega t - k(\omega)z])d\omega. \tag{2.22}$$

The solution for the second harmonic is not so simply expressed. Integration of equation (2.20) gives the formal solution

$$\hat{A}_2(z, \omega) = \hat{A}_2(-L/2, \omega) - i\frac{\mu_0\omega^2}{2k(\omega)}\int_{-L/2}^{z}\widehat{P_{NL}}(z', \omega)\exp[ik(\omega)z']dz'. \tag{2.23}$$

The frequency domain boundary condition for unseeded SHG is $\hat{A}_2(-L/2, \omega) = 0$. Hence, the SH envelope at the output of the nonlinear material, $\hat{A}_2(L/2, \omega)$, is

$$\hat{A}_2(L/2, \omega) = -i\frac{\mu_0\omega^2}{2k(\omega)}\int_{-L/2}^{L/2} \widehat{P_{NL}}(z', \omega)\exp[ik(\omega)z']dz'. \tag{2.24}$$

We now increase the integration bounds from $[-L/2, L/2]$ to $[-\infty, \infty]$, recognizing that this cannot affect the solution (2.24) because $P_{NL} = 0$ for $|z'| > L/2$. We then have

$$\hat{A}_2(L/2, \omega) = -i\frac{\mu_0\omega^2}{2k(\omega)}\int_{-\infty}^{\infty} \widehat{P_{NL}}(z', \omega)\exp[ik(\omega)z']dz'. \tag{2.25}$$

At this stage in the analysis, we have not yet specified the nonlinear polarization, $\widehat{P_{NL}}(z, \omega)$. Before we specify a particular form, we can interpret, physically, the implications of equation (2.25). The SH field at each frequency at the output of the nonlinear medium is given by a coherent sum of the phase-delayed waves generated by the nonlinear polarization produced at each position along the nonlinear medium. The phase delay experienced is determined by the material dispersion at each SH frequency.

The nonlinear polarization spectrum, $\widehat{P_{NL}}(z, \omega)$, relevant to SHG in a medium which is negligibly dispersive in $\chi^{(2)}$ can be written in terms of the fundamental electric field in the form[13]

$$\widehat{P_{NL}}(z, \omega) = (1/2)\varepsilon_0\chi^{(2)}(z)\int_{-\infty}^{\infty} \hat{E}_1(z, \omega')\hat{E}_1(z, \omega - \omega')d\omega', \tag{2.26}$$

where $\chi^{(2)}(z)$ is the material nonlinear susceptibility, allowed here to vary with position. We note that equation (2.26) corresponds to the time-domain relation

$$P_{NL}(z, t) = (1/2)\varepsilon_0\chi^{(2)}(z)E_1^2(z, t). \tag{2.27}$$

As we are assuming that the interaction occurs in the transparency range of the nonlinear material, and the medium is negligibly dispersive in $\chi^{(2)}$, we may use the more conventional notation for the nonlinear coefficient. We define a position-dependent (modulated) nonlinear coefficient, $d(z)$, normalized such that $\chi^{(2)}(z) = 2d(z)d_{eff}$, where d_{eff} is the maximum effective nonlinearity. (i.e. d_{eff} is the maximum value of $(1/2)\chi^{(2)}(z)$ for any position z

within the nonlinear medium.) This definition results in the following form for the nonlinear polarization relevant to SHG

$$\widehat{P_{NL}}(z, \omega) = \varepsilon_0 d_{eff} d(z) \int_{-\infty}^{\infty} \hat{E}_1(z, \omega') \hat{E}_1(z, \omega - \omega') d\omega' . \tag{2.28}$$

In order to solve equation (2.25) explicitly for the SH output, we must assume a particular form for the input fundamental electric field. We will derive the SH envelope for three cases: continuous-wave fundamental input, wide-bandwidth fundamental input in the presence of group velocity dispersion (GVD), and wide-bandwidth fundamental input in the presence of GVD at the second harmonic, but not the fundamental, frequency. Pulsed inputs are a special case of wide-bandwidth inputs.

2.5 Continuous-wave SHG and tuning curves

For this section, we assume a monochromatic fundamental field with frequency ω_1. For convenience, we choose a real-valued envelope. Thus,

$$\hat{A}_1(z, \omega) = A_1 \delta(\omega - \omega_1) + \text{c.c.}, \tag{2.29}$$

where $\delta(\omega)$ is the delta function. Evaluating equation (2.28) for $\omega = \omega_2$, where the second harmonic frequency $\omega_2 = 2\omega_1$ and using equations (2.9) and (2.29) gives

$$\widehat{P_{NL}}(z, \omega_2) = \varepsilon_0 d_{eff} d(z) A_1^2 \exp[-i2k(\omega_1)z] . \tag{2.30}$$

We use the relations $\omega_i = (2\pi c)/\lambda_i$, where λ_i are the free-space wavelengths. We also define the nonlinear coupling coefficient

$$\Gamma \equiv -i2\pi d_{eff}/(\lambda_1 n_2) , \tag{2.31}$$

where n_i is the refractive index at the fundamental ($i = 1$) or SH ($i = 2$) frequency, respectively. The **k**-vector mismatch, Δk, is given by $\Delta k \equiv 2k(\omega_1) - k(\omega_2)$. Using this notation and substituting equation (2.30) into equation (2.25) we obtain

$$\hat{A}_2(L/2, \omega_2) = \Gamma A_1^2 \int_{-\infty}^{\infty} d(z') \exp(-i\Delta k z') dz' . \tag{2.32}$$

We note that the solution (2.32) contains the spatial Fourier transform of the normalized nonlinear coefficient, $d(z)$. Writing this explicitly,

$$\hat{A}_2(L/2, \omega_2) = \Gamma A_1^2 \hat{d}(\Delta k) . \tag{2.33}$$

We now evaluate the square magnitude of equation (2.33) in the case of homogeneous crystals, for which we have $d(z) = 1$ for $|z| < L/2$. We find

$$\left|\hat{A}_2(L/2, \omega_2)\right|^2 = |\Gamma|^2 L^2 \left[\frac{\sin(\Delta k L/2)}{(\Delta k L/2)}\right]^2 \equiv |\Gamma|^2 L^2 \mathrm{sinc}^2(\Delta k L/2) , \tag{2.34}$$

which is the familiar SHG tuning curve result.

2.6 Pulsed input fields and the derivation of the SHG transfer function

At this stage in the analysis, we allow the fundamental field $E_1(z, t)$ to have an extended bandwidth around the carrier frequency ω_1. Thus, it is described by the general form of equation (2.22). Substituting the envelope form of the fundamental field from equations (2.16) and (2.9) into equation (2.26) gives

$$\widehat{P_{NL}}(z, \omega) = \varepsilon_0 d_{eff} d(z) \int_{-\infty}^{\infty} \hat{A}_1(\omega') \hat{A}_1(\omega - \omega') \exp(-i[k(\omega') + k(\omega - \omega')]z) d\omega' . \tag{2.35}$$

As with the monochromatic SHG case, we use the relations $\omega_i = (2\pi c)/\lambda_i$ and define the nonlinear coupling coefficient $\Gamma \equiv -i2\pi d_{eff}/(\lambda_1 n_2)$. Substituting equation (2.35) into equation (2.25) gives

$$\hat{A}_2(L/2, \omega) = \Gamma \int_{-\infty}^{\infty} d(z') \left[\int_{-\infty}^{\infty} \hat{A}_1(\omega') \hat{A}_1(\omega - \omega') \exp(-i[k(\omega') + k(\omega - \omega')]z') d\omega' \right] \exp(ik(\omega)z') dz' . \tag{2.36}$$

In writing equation (2.36), we have replaced the ω^2 in the pre-factor in equation (2.25) with ω_2^2 because $\widehat{P_{NL}}(z, \omega)$ only has significant magnitude near $\omega = \omega_2$ (i.e. the field band-widths have been assumed to be small compared with the carrier frequencies). Changing the order of integration and defining the **k**-vector mismatch

$$\Delta k(\omega, \omega') \equiv k(\omega') + k(\omega - \omega') - k(\omega) \ , \tag{2.37}$$

we obtain

$$\hat{A}_2(L/2, \omega) = \Gamma \int_{-\infty}^{\infty} \hat{A}_1(\omega')\hat{A}_1(\omega - \omega')\left[\int_{-\infty}^{\infty} d(z')\exp(-i\Delta k(\omega, \omega')z')dz'\right]d\omega' . \tag{2.38}$$

We recognize that $\hat{A}_2(L/2, \omega)$ only has significant magnitude near the second harmonic carrier frequency ω_2, and that $\hat{A}_1(\omega)$ only has significant magnitude near the fundamental carrier frequency ω_1. Therefore, we are only interested in the case where $\omega \approx \omega_2$ and $\omega' \approx \omega_1$, so that $\omega - \omega' \approx \omega_1$. The further simplification of equation (2.38) requires a simple form of the dispersion relation for $\Delta k(\omega, \omega')$. In equation (2.37) we expand $k(\omega)$ around ω_2, using the notation $k_2(\omega)$. We also expand $k(\omega - \omega')$ and $k(\omega')$ around ω_1, using the notation $k_1(\omega)$. To second order,

$$k_i(\omega) = k_i + \left.\frac{dk_i}{d\omega}\right|_{\omega_i} (\omega - \omega_i) + \left.\frac{1}{2}\frac{d^2 k_i}{d\omega^2}\right|_{\omega_i} (\omega - \omega_i)^2 + \tilde{k}_i(\omega - \omega_i) , \tag{2.39}$$

where $\tilde{k}_i(\omega - \omega_i)$ denotes all terms in a Taylor series for $k_i(\omega - \omega_i)$ with order higher than two. We note that $k_i^2 = \omega_i^2 \varepsilon(\omega_i)/c^2$, that the group velocity at each frequency is defined as

$$v_{g,i} \equiv \left(\left.\frac{dk_i}{d\omega}\right|_{\omega_i}\right)^{-1} , \tag{2.40}$$

and that the intra-pulse group velocity dispersion (GVD) at each frequency is defined as

$$\beta_i \equiv \left.\frac{d^2 k_i}{d\omega^2}\right|_{\omega_i} . \tag{2.41}$$

Substituting equations (2.39) through (2.41) into equation (2.37), defining the detunings $\Omega \equiv \omega - \omega_2$ and $\Omega_a \equiv \omega' - \omega_1$ and using $\omega_2 = 2\omega_1$ results in the general form

$$\begin{aligned}\Delta k(\Omega, \Omega_a) = &\left[k_1 + v_{g1}^{-1}\Omega_a + \frac{1}{2}\beta_1\Omega_a^2 + \tilde{k}_1(\Omega_a)\right] \\ &+ \left[k_1 + v_{g1}^{-1}(\Omega - \Omega_a) + \frac{1}{2}\beta_1(\Omega - \Omega_a)^2 + \tilde{k}_1(\Omega - \Omega_a)\right] \\ &- \left[k_2 + v_{g2}^{-1}\Omega + \frac{1}{2}\beta_2\Omega^2 + \tilde{k}_2(\Omega)\right] \quad , \end{aligned} \tag{2.42}$$

We now rewrite $\Delta k(\Omega, \Omega_a)$ as the sum of two terms, a first term which depends only on Ω and which enters simply into our final result, and a second term which contains both Ω and Ω_a. We use the compact notation

$$\Delta k(\Omega, \Omega_a) = \Delta k'(\Omega) + \Delta k''(\Omega, \Omega_a), \quad \text{where} \tag{2.43}$$

$$\Delta k'(\Omega) \equiv \Delta k_0 + \delta v\Omega + \delta\beta\Omega^2 + \tilde{k}_2(\Omega) \quad \text{and} \tag{2.44}$$

$$\Delta k''(\Omega, \Omega_a) \equiv \beta_1(\Omega_a^2 - \Omega\Omega_a) + \tilde{k}_1(\Omega - \Omega_a). \tag{2.45}$$

The function $\Delta k'(\Omega)$ contains all Ω_a-independent dispersion terms, while the function $\Delta k''(\Omega, \Omega_a)$ depends on Ω_a. Here we have defined the **k**-vector mismatch $\Delta k_0 \equiv 2k_1 - k_2$, the group velocity mismatch (GVM) parameter $\delta v \equiv [1/v_{g1} - 1/v_{g2}]$, and a group velocity dispersion (GVD) mismatch parameter $\delta\beta \equiv (1/2)[\beta_1 - \beta_2]$.

Substituting equation (2.43) into (2.38), and explicitly separating the exponential into Ω_a-dependent and Ω_a-independent parts gives

$$\begin{aligned}\hat{A}_2(L/2, \Omega + \omega_2) = \Gamma\int_{-\infty}^{\infty} &\hat{A}_1(\Omega_a + \omega_1)\hat{A}_1(\Omega - \Omega_a + \omega_1) \\ &\times\left[\int_{-\infty}^{\infty}[d(z') + D(\Omega, \Omega_a, z')]\exp[-i\Delta k'(\Omega)z']dz'\right]d\Omega_a, \end{aligned} \tag{2.46}$$

where we have defined $D(\Omega, \Omega_a, z') \equiv d(z')[\exp(-i\Delta k''[\Omega, \Omega_a]z') - 1]$. We note that the second integral in equation (2.46) is in the form of a spatial Fourier transform. Writing this explicitly,

$$\hat{A}_2(L/2, \Omega + \omega_2) = \Gamma \int_{-\infty}^{\infty} \hat{A}_1(\Omega_a + \omega_1)\hat{A}_1(\Omega - \Omega_a + \omega_1) \times \{\hat{d}[\Delta k'(\Omega)] + \hat{D}[\Omega, \Omega_a, \Delta k'(\Omega)]\} d\Omega_a \ , \quad (2.47)$$

where $\hat{d}[\Delta k'(\Omega)]$ is the spatial Fourier transform of the normalized nonlinear coefficient distribution, $d(z)$, and $\hat{D}[\Omega, \Omega_a, \Delta k'(\Omega)]$ is the Ω- and Ω_a-dependent spatial Fourier transform of $D(\Omega, \Omega_a, z')$. For both terms, $\Delta k'(\Omega)$, not Ω, is the transform variable. Rearranging equation (2.47) and noting that $\widehat{A_1^2}(\Omega + \omega_2)$ is the self-convolution of $\hat{A}_1(\Omega + \omega_1)$,

$$\widehat{A_1^2}(\Omega + \omega_2) = \int_{-\infty}^{\infty} \hat{A}_1(\Omega_a + \omega_1)\hat{A}_1(\Omega - \Omega_a + \omega_1) d\Omega_a , \quad (2.48)$$

gives

$$\hat{A}_2\left(\frac{L}{2}, \Omega + \omega_2\right) = \Gamma \widehat{A_1^2}(\Omega + \omega_2)\hat{d}[\Delta k'(\Omega)] + \Gamma \int_{-\infty}^{\infty} \hat{A}_1(\Omega_a + \omega_1)\hat{A}_1(\Omega - \Omega_a + \omega_1)\hat{D}[\Omega, \Omega_a, \Delta k'(\Omega)] d\Omega_a \ . \quad (2.49)$$

With equations (2.10) and (2.48), we find

$$\widehat{A_1^2}(\Omega + \omega_2) = \widehat{[E_1(0, t)]^2} . \quad (2.50)$$

Therefore, $\widehat{A_1^2}(\Omega + \omega_2)$ is the Fourier transform of the square of the fundamental field at the center of the nonlinear crystal ($z = 0$). In writing equation (2.49), we have made no assumptions about the material dispersion at either of the fundamental or second harmonic wavelengths.

An important limit, for which there is a simple analytical solution for $\hat{A}_2(L/2, \Omega + \omega_2)$, is the case in which GVD and higher order dispersion terms at the fundamental wavelength can be ignored. Explicitly, we are interested in the case where $\beta_1(\Omega_a^2 - \Omega\Omega_a)L << \pi$ and $\tilde{k}_1(\Omega + \omega_1)L << \pi$ for all Ω for which $\widehat{A_1^2}(\Omega + \omega_2)$ has significant amplitude. Therefore, we set $\beta_1 = 0$ and $\tilde{k}_1(\Omega + \omega_1) = 0$; then $\hat{D}[\Delta k'(\Omega), \Omega_a + \omega_1] = 0$ and the second term in equation (2.49) vanishes. Thus, we have

$$\hat{A}_2(L/2, \Omega + \omega_2) = \Gamma\hat{d}[\Delta k'(\Omega)]\widehat{A_1^2}(\Omega + \omega_2). \tag{2.51}$$

In equation (2.51), the factor $\Gamma\hat{d}[\Delta k'(\Omega)]$ is a transfer function which relates the spectrum of the second harmonic envelope to the spectrum of the square of the fundamental field at the center of the nonlinear crystal. We note that this transfer function is essentially the tuning curve for CW-SHG given in equation (2.33). We also note that, since we have assumed that $\beta_1 = 0$ in writing the transfer function, we also have $\delta\beta \equiv -\beta_2/2$.

While significant physical intuition about the effects of the material parameters and of the QPM grating can be obtained from the transfer function relationship (2.51), the connection between the frequency-domain spatial envelopes and the pulses is not obvious. To clarify this connection, we replace our frequency-domain spatial envelopes, $\hat{A}_i(z, \omega)$, with the temporal envelopes commonly used in the ultrafast and nonlinear optics literature, for which we use the notation $B_i(z, t)$. (Here, $i = 1, 2$ for the fundamental and SH, respectively.) We use the definitions

$$E_i(z, t) \equiv B_i(z, t)\exp(i\omega_i t). \tag{2.52}$$

This temporal envelope can be related to the frequency-domain spatial envelope through its Fourier transform, $\hat{B}_i(z, \omega)$, by

$$\hat{B}_i(z, \omega - \omega_i) = \hat{A}_i(z, \omega)\exp(-ik(\omega)z). \tag{2.53}$$

Using equation (2.53) and the Fourier shift theorem, we rewrite equation (2.51) as

$$\hat{B}_2(L/2, \Omega) = \Gamma\hat{d}[\Delta k'(\Omega)]\widehat{B_1^2}(0, \Omega)\exp[-ik(\Omega + \omega_2)L/2]. \tag{2.54}$$

Equation (2.54) represents no loss of generality, compared with equation (2.51). We will use equation (2.54) in section 2.14.

Equation (2.54) includes the effects of arbitrary dispersion at the SH frequency. It can be approximated to second order in Ω using equations (2.39) and (2.44) and neglecting high-order terms. For simplicity, we assume phasematched interactions by taking $\Delta k_0 = 0$ and neglect an unimportant overall time delay (linear phase factor) on the SH pulse relative to the fundamental pulse. The result is

$$\hat{B}_2(L/2, \Omega) = \Gamma\hat{d}[\delta v\Omega - \beta_2\Omega^2/2]\widehat{B_1^2}(0, \Omega)\exp\left[-i\beta_2\Omega^2\frac{L}{4}\right], \tag{2.55}$$

in which GVD at the SH frequency appears explicitly in two places. The more obvious effect of GVD is as a quadratic phase factor with a magnitude equal to that which would be caused by simple GVD spreading within the nonlinear material over a distance of $L/2$. This can be interpreted physically as the weighted average GVD felt by the SH pulse which is generated as it propagates through the crystal of length L. The GVD at the SH wavelength also appears in the form of $\delta\beta$ in the **k**-vector mismatch $\Delta k'(\Omega)$, which scales the transfer function.

In order to elucidate the physics of group velocity mismatch (GVM) effects in SHG, and to simplify the discussion in sections 2.7 through 2.12, we return to equation (2.54), neglect GVD at both frequencies by taking $\delta\beta = \beta_2 = 0$ and, again, assume phasematched interactions by taking $\Delta k_0 = 0$. We also simplify the notation by defining $\hat{B}_2(\Omega) \equiv \hat{B}_2(L/2, \Omega)$ and $\widehat{B_1^2}(\Omega) \equiv \widehat{B_1^2}(0, \Omega)$. We find the following simplified SH solution for the case where GVD can be neglected:

$$\hat{B}_2(\Omega) = \Gamma\hat{d}(\Omega\delta v) \cdot \widehat{B_1^2}(\Omega), \tag{2.56}$$

which we recognize as similar in form to equation (2.51).

In summary, SHG in the absence of pump depletion and GVD at the fundamental can be accurately described by the transfer function relation (2.51) with the dispersion relation (2.44). This transfer function applies for second harmonic generation of (single- or multi-frequency) CW or (transform limited or chirped) pulsed inputs, in the presence of group velocity mismatch between the fundamental and second harmonic waves and in the presence of arbitrary dispersion at the second harmonic. Equation (2.56) accurately describes all of the experiments discussed in chapter 3.

2.7 Quasi-static and Nonstationary limits

We now explicitly evaluate the Fourier transform in equation (2.56) in the case of homogeneous crystals, for which we have $d(z) = 1$ for $|z| < L/2$. We find

$$\hat{B}_2(\Omega) = \Gamma L \frac{\sin(\Omega\delta\nu L/2)}{(\Omega\delta\nu L/2)} \widehat{B_1^2}(\Omega) \equiv \Gamma L \mathrm{sinc}(\Omega\delta\nu L/2) \widehat{B_1^2}(\Omega). \tag{2.57}$$

We note that $\Gamma L \mathrm{sinc}(\Omega\delta\nu L/2)$ is a constant-phase transfer function. The effects of transfer functions which have non-constant (and nonlinear in Ω) phase will be addressed in section 2.15.

Two important limiting cases are instructive. The *quasi-static* limit, in which the bandwidth of the tuning curve exceeds the bandwidth of the input pulse, applies to short crystals. In this limit, the second harmonic output pulse is simply proportional to the square of the fundamental input pulse. No effects related to dispersion (other than phasematching) are significant. We then have

$$\hat{B}_2(\Omega) = \Gamma L \widehat{B_1^2}(\Omega). \tag{2.58}$$

The *nonstationary* limit, in which the bandwidth of the input pulse exceeds the bandwidth of the tuning curve, applies to long crystals. In this limit, the SHG device acts like a spectral filter, resulting in spectral narrowing and pulse distortion. We then have

$$\hat{B}_2(\Omega) = \Gamma L \mathrm{sinc}(\Omega\delta\nu L/2) \widehat{B_1^2}(0). \tag{2.59}$$

where we use $\widehat{B_1^2}(0)$ because $\widehat{B_1^2}(\Omega)$ has nearly constant value over the range of Ω for which the tuning curve has significant magnitude. The sinc spectrum results in a flat-top, or square, SH pulse. The length of this pulse is proportional to the length of the crystal, because the width of the transfer function, and hence the width of the SH spectrum, is inversely proportional to the length of the crystal.

2.8 Optimum crystal length regime

Most practical implementations of ultrashort-pulse SHG use crystals with lengths that lie at the crossover between the quasi-static limit and the nonstationary limit. This compromise is made because of the desire for high efficiency (attained with long crystals) without significant pulse broadening (avoided with short crystals). In this crossover regime we use

$$\hat{B}_2(\Omega) = \Gamma L \mathrm{sinc}(\Omega \delta v L/2) \widehat{B_1^2}(\Omega), \tag{2.60}$$

where we allow $\widehat{B_1^2}(\Omega)$ to vary appreciably over the range of Ω for which the tuning curve has significant magnitude. Two quantities are of greatest interest: energy conversion efficiency and SH pulse duration. The energy conversion efficiency, η_E, is found by integrating the input and output spectral intensities over all frequencies. We have

$$\eta_E = \frac{\Gamma^2 L^2 \int |\mathrm{sinc}(\Omega \delta v L/2) \widehat{B_1^2}(\Omega)|^2 d\Omega}{\int |\hat{B}_1(\Omega)|^2 d\Omega}. \tag{2.61}$$

The SH pulse shape can be found from the inverse Fourier transform of $\hat{B}_2(\Omega)$. For convenience, we quantify bandwidths by the full width at half maximum (FWHM) of the relevant power spectrum (which, in the case of this plane-wave analysis, is proportional to intensity.) The FWHM bandwidth of the transfer function in equation (2.57) is given by $\Delta\Omega_{SHG} = 1.77\pi/\delta v L$ and scales inversely as the interaction length and the material GVM parameter. Because the transfer function in equation (2.60) describes the SH spectrum, $\Delta\Omega_{SHG}$ refers to a detuning in the SH spectrum. The corresponding detuning for the fundamental spectrum is $\Delta\Omega_{SHG}/2$. We now define a characteristic crystal length L_{max} as that length for which $\Delta\Omega_{SHG}/2 = \Delta\Omega_{Pulse}$, where $\Delta\Omega_{Pulse}$ is the FWHM bandwidth of the fundamental pulse. (We make this definition of L_{max} because the spectral width of the fundamental pulse and the bandwidth of the tuning curve for CW-SHG are the parameters an experimentalist is most likely to measure.) Thus,

$$L_{max} = \frac{0.886\pi}{\delta v \cdot \Delta\Omega_{Pulse}}. \tag{2.62}$$

Expressed in terms of the (FWHM) wavelength bandwidth of the fundamental pulse $\Delta\lambda_{Pulse}$,

$$L_{max} = \frac{0.44 \cdot \lambda^2}{\Delta\lambda_{Pulse} \cdot \delta v c}. \tag{2.63}$$

A normalized crystal length $\xi_{L_{max}}$ can be defined as $\xi_{L_{max}} \equiv L/L_{max}$. Note that L_{max} is, in general, not the same as the walkoff length, $L_{walkoff}$, defined in chapter 1. (However, as we

shall see in section 2.9, L_{max} and $L_{walkoff}$ are closely related for transform limited pulses.) We define L_{max} and $\xi_{L_{max}}$ in the frequency domain here both for consistency with the rest of our analysis and for generality. This definition for L_{max} is useful for non-transform-limited (defined in section 2.9) pulses and for finite-bandwidth non-pulse fields, whereas the conventional time-domain definition for $L_{walkoff}$ can lead to misleading results in these cases.

The efficiency can be written in the form

$$\eta_E(\xi) = \Gamma^2|B_{1,0}|^2 L_{max}^2 \xi_{L_{max}}^2 g(\xi_{L_{max}}), \tag{2.64}$$

where $B_{1,0}$ is the peak (with respect to time) fundamental field at the center of the crystal. The factor $g(\xi_{L_{max}})$ accounts for the time dependence of the conversion efficiency and for group velocity walkoff (spectral narrowing) effects. In general, $g(\xi_{L_{max}})$ is given by

$$g(\xi_{L_{max}}) \equiv \frac{1}{|B_{1,0}|^2} \cdot \frac{\int \left|\mathrm{sinc}(\Omega \delta v L_{max} \xi_{L_{max}}/2)\widehat{B_{1,0}^2}(\Omega)\right|^2 d\Omega}{\int |\widehat{B_{1,0}}(\Omega)|^2 d\Omega}. \tag{2.65}$$

We note that from equation (2.62) we have $\delta v L_{max} = 0.886\pi/\Delta\Omega_{Pulse}$, so

$$\Omega \delta v L_{max} \xi_{L_{max}}/2 = 0.443\pi\left(\frac{\Omega}{\Delta\Omega_{Pulse}}\right)\xi_{L_{max}} \tag{2.66}$$

in the argument of equation (2.65). In the quasi-static limit ($\xi_{L_{max}} << 1$), we can find a simpler expression for $g(\xi_{L_{max}})$. Taking sinc = 1 over the pulse bandwidth, and applying Parseval's theorem for Fourier transforms to equation (2.65), we find that $g(\xi_{L_{max}})$ is given by

$$g(\xi_{L_{max}} << 1) = \frac{1}{|B_{1,0}|^2} \cdot \frac{\int |\widehat{B^2_1}(t)|^2 dt}{\int |\hat{B}_1(t)|^2 dt}. \tag{2.67}$$

For most realistic pulse shapes $g(\xi_{L_{max}} << 1)$ is slightly less than unity. In the highly nonstationary limit $g(\xi_{L_{max}} >> 1)$, where the sinc function is narrow compared to the pulse bandwidth, the linear decrease in the width of the sinc with $\xi_{L_{max}}$ leads to a linear decrease in g.

2.9 Transform limited fundamental pulses

In order to investigate the crossover regime quantitatively, we must evaluate equation (2.65) or (2.67) numerically. In this section we consider only transform-limited pulses. We use the conventional definition for transform-limited pulses, that is, that the field spectrum of the pulse has constant (or linear) phase with respect to frequency. Transform-limited pulses are not compressible. Non-transform-limited pulses include those which are chirped (predictable and smoothly varying phase in the frequency domain), as well as noise bursts (randomly varying phase in the frequency domain). To simplify the interpretation of the results presented in this section, we will take advantage of the relationship between L_{max}, as defined in section 2.8, and the temporal group velocity walkoff length, $L_{walkoff} \equiv \tau_1 / \delta v$. Here, τ_1 is the FWHM pulse duration.

Assuming transform-limited pulses, the FWHM (radian frequency) bandwidth is given by

$$\Delta\Omega_{Pulse} = 2\pi \cdot \mathrm{TBP}/\tau_1 , \tag{2.68}$$

where TBP is the FWHM (physical frequency) time-bandwidth product for that pulse shape. Table 2.1 lists time-bandwidth products for several pulse shapes.

Table 2.1: Time-bandwidth products evaluated for various pulse shapes

Pulse Shape	Time-Bandwidth Product
Gaussian	0.441
Sech^2	0.315
Sinc^2	0.886
Square	0.886

Substituting equation (2.68) for the fundamental pulse into equation (2.62) gives the result

$$L_{max} = \frac{0.443}{\mathrm{TBP}} \cdot L_{walkoff} . \tag{2.69}$$

We may now define a second normalized crystal length, $\xi_{L_{wo}}$, relative to $L_{walkoff}$. We have

$$\xi_{L_{wo}} \equiv L / L_{walkoff} . \tag{2.70}$$

Combining equations (2.69) and (2.70), we find

$$\xi_{L_{wo}} = \xi_{L_{max}} \cdot \frac{0.443}{\mathrm{TBP}} . \tag{2.71}$$

Figure 2.1 shows g plotted against $\xi_{L_{wo}}$ for transform-limited pulses of several shapes. The $\xi_{L_{wo}} << 1$ limits quantify the effect of time dependent conversion efficiency for each pulse shape. Each curve has a knee near $\xi_{L_{wo}} \approx 1$, where spectral narrowing becomes important.

We now consider the duration of the output second harmonic pulses and define a normalized pulse length parameter $\tau_{nor} \equiv \tau_2 / \tau_1$, where τ_1 is the FWHM duration of the fundamental input pulse and τ_2 is the FWHM duration of the SH output pulse. There is no simple analytical expression for τ_{nor} in terms of $\xi_{L_{max}}$ or $\xi_{L_{wo}}$ for arbitrary pulse shapes. Instead, we find τ_{nor} by numerically evaluating equation (2.60) and inverse Fourier transforming the result to find the temporal shape of the SH pulse. Figure 2.2 shows τ_{nor} plotted against $\xi_{L_{wo}}$ for transform-limited pulses with the shapes investigated above. Figure 2.3 shows shapes of SH temporal waveforms for crystals of various lengths; for this example, sech^2 pulses are assumed. (Note that for crystals with $\xi_{L_{max}} = 1$, the SH pulse is similar in shape to a Gaussian pulse.) Finally, table 2.2 tabulates values of $\xi_{L_{max}} / \xi_{L_{wo}}$ and values of both g and τ_{nor} for $\xi_{L_{max}} << 1$, $\xi_{L_{max}} = 1$ and $\xi_{L_{wo}} = 1$.

From figures 2.1-2.3 we see the trade-off between conversion efficiency and SH pulse duration. Short crystals produce short SH pulses at the expense of conversion efficiency. Long crystals convert with high efficiencies, but at the cost of pulse broadening. It is for this reason that most applications for ultrashort-pulse SHG call for the use of nonlinear crystals with $\xi_{L_{wo}} \sim 1$. There are two situations in which $\xi_{L_{wo}} \sim 1$ is not a good compromise. First, when input pulses are sufficiently long (in the range of tens of picoseconds), crystals satisfying $\xi_{L_{wo}} \sim 1$ may not be available due to size limitations with crystal growth. Second, when input

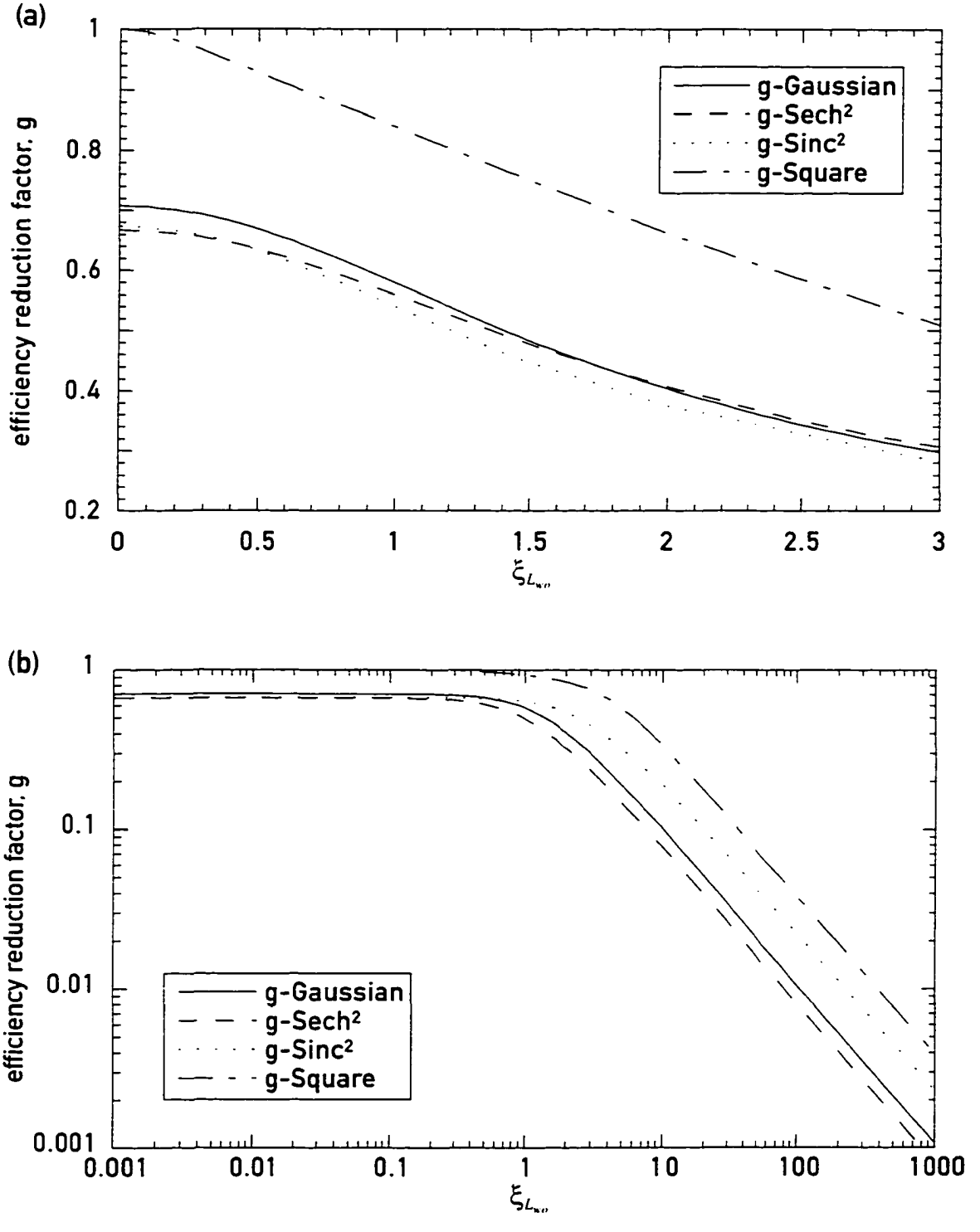

Figure 2.1: The efficiency reduction factor, g, depends on the normalized crystal length, $\xi_{L_{w_0}}$, and on the pulse shape. Values for Gaussian, sech^2, sinc^2 and square pulses are shown on linear (a) and log (b) scales.

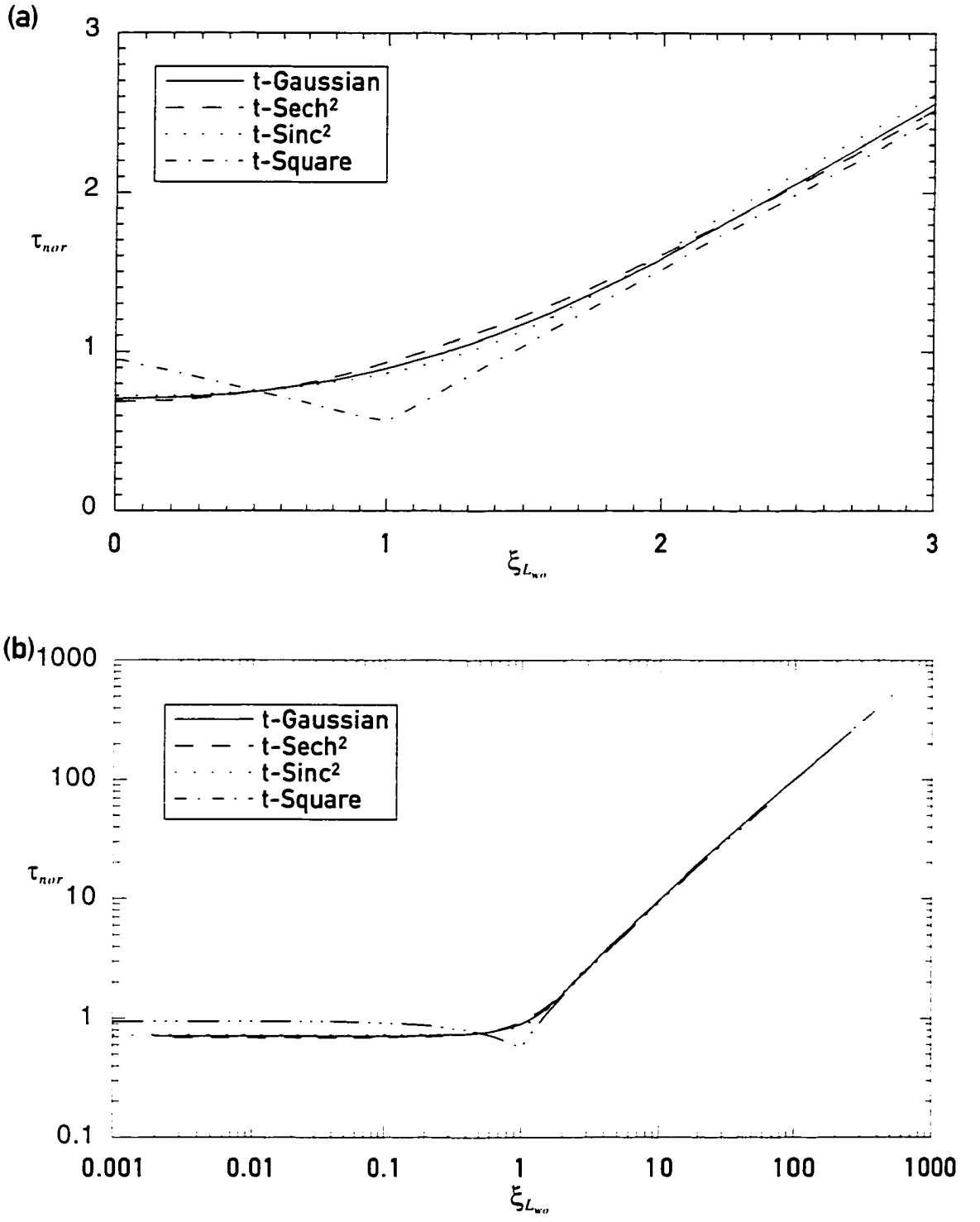

Figure 2.2: The normalized pulse length parameter, τ_{nor}, depends on the normalized crystal length, $\xi_{L_{wo}}$, and on the pulse shape. Values for Gaussian, sech^2, sinc^2 and square pulses are shown on linear (a) and log (b) scales.

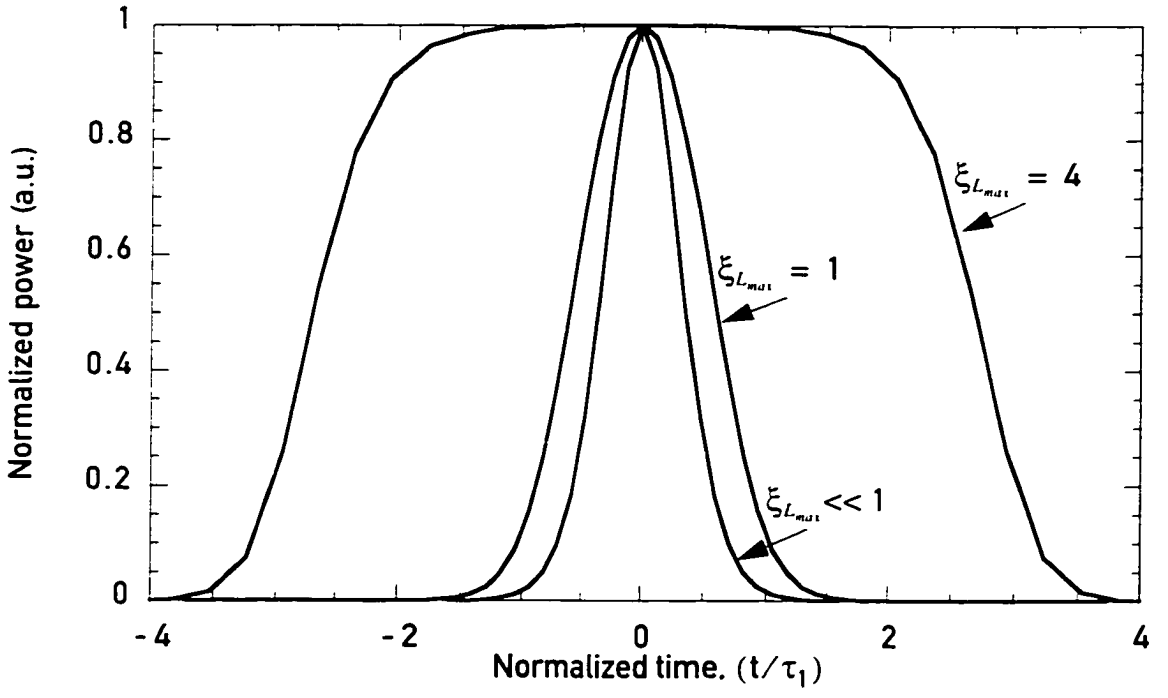

Figure 2.3: Temporal shapes of SH waveforms (shown on a linear scale) for sech^2 fundamental pulses and crystals of various lengths. Note that for crystals with $\xi_{L_{mat}} = 1$, the SH pulse is similar in shape to a Gaussian pulse.

pulses are sufficiently short (in the range of tens of femtoseconds,) crystals satisfying $\xi_{L_{wo}} \sim 1$ may exhibit enough GVD at the SH frequency to distort (chirp) the pulses. We will find in section 2.4 that this problem can be addressed with chirped QPM gratings in the nonlinear crystal.

Table 2.2: Numerical efficiency and pulse-length factors evaluated for various pulse shapes

Pulse Shape	$\frac{\xi_{L_{mat}}}{\xi_{L_{wo}}}$	g			τ_{nor}		
		$\xi_{L_{mat}} << 1$	$\xi_{L_{mat}} = 1$	$\xi_{L_{wo}} = 1$	$\xi_{L_{mat}} << 1$	$\xi_{L_{mat}} = 1$	$\xi_{L_{wo}} = 1$
Gaussian	1.00	0.707	0.579	0.579	0.707	0.893	0.893
Sech^2	0.712	0.667	0.493	0.564	0.688	1.156	0.931
Sinc^2	2.0	0.673	0.632	0.540	0.724	0.753	0.862
Square	2.0	1	0.928	0.839	1	0.753	0.597

Note that $g(\xi_{L_{walk}} = 1)$ and $\tau_{nor}(\xi_{L_{walk}} = 1)$ depend only weakly on pulse shape. This confirms our assumption that the group velocity walkoff length, $L_{walkoff}$, is a natural parameter for describing nonstationary interactions. We therefore rewrite equation (2.64) using $L_{walkoff}$, giving

$$\eta_E(\xi_{L_{walk}}) = \Gamma^2 |B_{1,0}|^2 L_{walkoff}^2 \xi_{L_{walk}}^2 g(\xi_{L_{max}}) \,. \tag{2.72}$$

An arbitrary, but useful, definition for the optimum crystal length L_{opt} is that value of L which for each pulse shape produces a SH pulse with the same FWHM duration as the fundamental pulse. We also define $\xi_{L_{max},opt} \equiv L_{opt}/L_{max}$ and $\xi_{L_{walk},opt} \equiv L_{opt}/L_{walkoff}$. These fixed parameters are the optimum values of $\xi_{L_{max}}$ and $\xi_{L_{walk}}$, respectively. (i.e. $\tau_{nor}(\xi_{L_{max}} = \xi_{L_{max},opt}) = 1$ and $\tau_{nor}(\xi_{L_{walk}} = \xi_{L_{walk},opt}) = 1$.)

Using these definitions, we can group together all unitless factors in equation (2.72) and find $\xi^2_{L_{walk},opt} \cdot g(\xi_{L_{max},opt})$. Table 2.3 tabulates values of $\xi_{L_{max},opt}$, $\xi_{L_{walk},opt}$, $g(\xi_{L_{max},opt})$ and $\xi^2_{L_{walk},opt} \cdot g(\xi_{L_{max},opt})$ for transform-limited pulses of several shapes. Table 2.3 also includes values of $\xi_{L_{walk},opt} \cdot g(\xi_{L_{max},opt})$ for use in section 2.11. Note that in table 2.3 we use both $\xi_{L_{max},opt}$ (because g is defined in terms of this bandwidth-matching length) and $\xi_{L_{walk},opt}$ (which is the natural parameter appearing in the efficiency expressions above), as appropriate.

Table 2.3: Optimum crystal length and efficiency evaluated for various pulse shapes

Pulse Shape	$\xi_{L_{max},opt}$	$\xi_{L_{walk},opt}$	$g(\xi_{L_{max},opt})$	$\xi^2_{L_{walk},opt} \cdot g(\xi_{L_{max},opt})$	$\xi_{L_{walk},opt} \cdot g(\xi_{L_{max},opt})$
Gaussian	1.22	1.22	0.538	0.801	0.656
$Sech^2$	0.815	1.14	0.535	0.695	0.610
$Sinc^2$	2.61	1.30	0.482	0.815	0.627
Square	2.92	1.46	0.758	1.62	1.11

From equation (2.72) and table 2.3, we can determine that the expected conversion efficiency is only a weak function of pulse shape, for a given FWHM pulse duration and choice of nonlinear material.

2.10 Uniform Quasi-phasematching

In general, SHG cannot be phasematched at all interesting wavelengths in any particular material. As described in chapter 1, the technique of quasi-phasematching (QPM) can be used to enable SHG in several materials over wide ranges of wavelengths.

We include QPM in the present analysis by allowing spatially inhomogeneous nonlinear coefficient distributions. In particular, we consider materials with a uniform periodic structure, whose positive spatial frequency part we write as

$$d(z) = \sum_m a_m \exp(ik_{g,m}z) \tag{2.73}$$

for $|z| < L/2$ and $d(z) = 0$ for $|z| > L/2$. In equation (2.73), a_m and $k_{g,m}$ are the amplitude and **k**-vector of the m-th Fourier component of the periodic nonlinear coefficient distribution. We find

$$\hat{d}[\Delta k'(\Omega)] = L\sum_m a_m \mathrm{sinc}([\Delta k'(\Omega) - k_{g,m}]L/2). \tag{2.74}$$

We return to the transfer function relation (2.56), which ignores GVD, and write

$$\hat{B}_2(\Omega) = \Gamma\hat{d}[\Delta k_0 + \delta v\Omega]\widehat{B_1^2}(\Omega). \tag{2.75}$$

Substituting equation (2.74) into equation (2.75) gives

$$\hat{B}_2(\Omega) = \left\{\Gamma L\sum_m a_m \mathrm{sinc}([(\Delta k_0 - k_{g,m}) + \delta v\Omega]L/2)\right\}\widehat{B_1^2}(\Omega). \tag{2.76}$$

We now assume that the QPM grating period Λ_{QPM} is chosen to satisfy $\Lambda_{QPM} = 2\pi m/\Delta k_0$ for some value of m (where m is the order of QPM), so that $k_{g,m} = \Delta k_0$. We also assume that the fundamental pulse spectrum overlaps the transfer function in a region due to only one order of the QPM grating. In other words, we assume that $|\delta v\Omega| << |\Delta k_0 - k_{g,m}|$ for all other values of m and for all values of Ω for which $\widehat{A_1^2}(\Omega)$ has non-negligible magnitude. Since the spacing (in frequency) between QPM-orders of the

transfer function is equal (i.e. $|k_{g,m+1} - k_{g,m}| = k_{g,1} = \Delta k_0$), we can rewrite this assumption as $|\delta v\Omega| << k_{g,1}$). This second assumption will become more significant when we discuss aperiodic gratings in section 2.4. We find

$$\hat{B}_2(\Omega) = \Gamma L a_m \mathrm{sinc}(\delta v \Omega L/2) \widehat{B_1^2}(\Omega). \tag{2.77}$$

In the case where $d(z)$ is a 50% duty-cycle unity-magnitude square wave, we have for mth-order QPM

$$a_m = \left\{ \begin{array}{cc} 2/m\pi & \text{if } m \text{ odd} \\ 0 & \text{if } m \text{ even} \end{array} \right\}. \tag{2.78}$$

If we lump a_m into d_{eff}, and therefore into Γ, we find the same general solution for QPM-SHG as we found with equation (2.57) for phasematched SHG.

2.11 Ultrashort-pulse Figure of Merit

In many applications, the conversion efficiency for SHG of ultrashort pulses is of primary importance. Hence, focussing of the fundamental beam to achieve high intensities is often employed. We will include the effects of focussing into the above analysis by generalizing the results of Boyd and Kleinman[14] for CW-SHG of Gaussian beams. We begin with the intensity conversion efficiency for Gaussian beams of power P_1 expressed as

$$\eta_I = P_1 \frac{16\pi^2 d_{eff}^2}{\varepsilon_0 c n_1 n_2 \lambda_1^3} L h, \tag{2.79}$$

where h is a dimensionless coefficient which quantifies the effects of focussing and birefringence on the SHG efficiency and is of order unity near optimal focusing for noncritically phasematched interactions. Equation (2.79) also applies exactly for SHG of square-shaped pulses in the quasi-static limit when P_1 is the peak fundamental power.

The dimensionless factor g analyzed in detail in sections 2.8 and 2.9 accurately quantifies the effects of the time dependence of the conversion efficiency for any focussing condition.

However, to exactly account for nonstationary (group velocity walkoff, or spectral narrowing) effects with g, the interaction must occur in the near-field limit. When an interaction occurs in neither the near-field nor the quasi-static limit, the numerical factors g and h become coupled. An exact treatment of this case is beyond the scope of this thesis. With this caveat, we may generalize equation (2.79) to describe focussed ultrashort-pulse SHG.

Grouping physical constants separately from experimental and material parameters, we have

$$\eta_E = \frac{16\pi^2}{\varepsilon_0 c}\left(\frac{d_{eff}^2}{n_1 n_2}\right)\left(\frac{P_{1.0}}{\lambda_1^3}\right)Lhg, \tag{2.80}$$

where we use the notation $P_{1.0}$ for the peak fundamental power. We now consider the case where the crystal length satisfies $L = L_{opt}$, (i.e. $\xi_{L_{walk}} = \xi_{L_{walk},opt}$). Using the substitutions $L_{walkoff} \equiv \tau_1/\delta v$, $\delta v = \Delta n_g/c$ and $\xi_{L_{walk}} \equiv L/L_{walkoff}$, we rewrite equation (2.80) as

$$\eta_{E,opt} = \frac{16\pi^2}{\varepsilon_0}\left[\frac{d_{eff}^2}{n_1 n_2 \Delta n_g}\right]\left[\frac{P_{1.0}\tau_1}{\lambda_1^3}\right]\xi_{L_{walk},opt}\, g(\xi_{L_{max},opt})h, \tag{2.81}$$

where $\Delta n_g \equiv n_{g,1} - n_{g,2}$ and where $n_{g,1} \equiv c/v_{g,1}$ and $n_{g,2} \equiv c/v_{g,2}$ are the group refractive indices for the fundamental and SH frequency, respectively.

We now interpret equation (2.81) for the case of noncritically phasematched interactions. Lumping together all of the materials-related factors (grouped in the first set of brackets in equation (2.81)) into a material figure of merit (FOM), gives

$$\text{FOM} \equiv \frac{d_{eff}^2}{n_1 n_2 \Delta n_g}. \tag{2.82}$$

The pulse-shape-related factors are grouped in the third set of brackets; this same collection of factors is tabulated in table 2.3 and is only weakly dependent on pulse shape. Finally, we note that the fundamental pulse energy $\mathcal{E}_p$ is given by $\mathcal{E}_p = \alpha P_{1.0}\tau_1$, where the proportionality constant α depends on the pulse shape. We define a pulse-shape efficiency parameter b as

$$b \equiv \frac{1}{\alpha}\xi_{L_{walk},opt}\, g(\xi_{L_{max},opt}). \tag{2.83}$$

With these substitutions, equation (2.81) becomes

$$\eta_{E,opt} = \frac{16\pi^2 bh}{\varepsilon_0 \lambda_1^3} \mathrm{FOM} \cdot \mathcal{E}_p . \tag{2.84}$$

Table 2.4 tabulates values of b for the pulse shapes considered above; we note that b can be approximated by 0.6 for most pulse shapes. For noncritically phasematched, confocally focussed interactions, $h = 0.8$. From equation (2.84), we find that the pulse energy, rather than the peak power or pulse length, is the natural quantity to consider when determining the conversion efficiency for focussed SHG of ultrashort pulses in noncritically-phasematched crystals with lengths chosen to avoid pulse broadening. Efficiency scales linearly with pulse energy and with the material figure of merit. Therefore, for a given wavelength and material, the SHG efficiency can be expressed in the convenient units of %-Energy^{-1}.

For critically phasematched, confocally focussed interactions, h depends on the crystal length. In the limit of significant Poynting vector walkoff (when $L > 2.7 w_0/\rho$, or in the case of crystal lengths limited by temporal group velocity walkoff of transform-limited Gaussian pulses, when $\tau_1 > 2.7\lambda_1 \Delta n_g / n_1 c \rho^2$), h can be well approximated[15] by $h \approx (1/\rho)\sqrt{\lambda_1/(\pi n_1 L)}$, where ρ is the Poynting vector walkoff angle and w_0 is the beam waist size. Again considering the case where the crystal length satisfies $L = L_{opt}$, we find

$$h \approx \frac{1}{\rho}\sqrt{\frac{1}{\xi_{L=L_{opt}}} \cdot \frac{\Delta n_g}{n_1} \cdot \frac{1}{\tau_1} \cdot \frac{\lambda_1}{\pi c}} . \tag{2.85}$$

Substituting equation (2.85) into equation (2.81) and, again, using $\mathcal{E}_p = \alpha P_{1,0} \tau_1$ results in

$$\eta_{E,opt} = \frac{16\pi^{1.5} b_{crit}}{\varepsilon_0 \lambda_1^3} \sqrt{\frac{\lambda_1}{\tau_1 c}} \mathrm{FOM}_{crit} \cdot \mathcal{E}_p , \tag{2.86}$$

where we have defined a figure of merit for critically-phasematched ultrashort-pulse SHG as

$$\mathrm{FOM}_{crit} \equiv \frac{d_{eff}^2}{n_1^{1.5} n_2 \sqrt{\Delta n_g}\rho} \tag{2.87}$$

and a pulse shape efficiency parameter for critically-phasematched ultrashort-pulse SHG as

$$b_{crit} \equiv \frac{\sqrt{\xi_{L_{max}\,opt}}}{\alpha} g(\xi_{L_{max}\,opt}) . \tag{2.88}$$

Table 2.4 tabulates values of b_{crit} for the pulse shapes considered above; we note that b can be approximated by 0.5 for most pulse shapes. From equation (2.86), we find that the pulse energy, as well as the pulse length, determine the conversion efficiency for focussed SHG of ultrashort pulses in critically-phasematched crystals. As with noncritically phasematched interactions, the efficiency scales linearly with the material figure of merit. Therefore, for a given wavelength and for a given material, the SHG efficiency can be expressed in the convenient units of $\%\text{-Pulselength}^{0.5} \cdot \text{Energy}^{-1}$.

Table 2.4: Pulse shape efficiency parameter for optimum crystal length for various pulse shapes

Pulse Shape	b	b_{crit}
Gaussian	0.617	0.558
$Sech^2$	0.541	0.506
$Sinc^2$	0.570	0.500
Square	1.11	0.916

It is important to note that the apparent divergence in η_E for critically phasematched pulses as $\tau_1 \rightarrow 0$ is limited in practice by the violation of the approximate form of h used to derive equation (2.84). In general, the efficiency of critically phasematched interactions will be less than or equal to (in the limit as $\tau_1 \rightarrow 0$) that of a noncritically phasematched interaction in materials with the same $d_{eff}^2 / n_1 n_2 \Delta n_g$.

2.12 Comparison of nonlinear materials

We now consider several technologically important nonlinear materials in the context of ultrashort-pulse SHG for both quasi-phasematched and phasematched interactions. Because

QPM interactions are not phase velocity matched, they typically exhibit a group velocity mismatch that is larger than that in phasematched interactions. However, the larger nonlinear coefficients made available with QPM often more than compensate for the requisite short interaction lengths. Table 2.5 lists Δn_g, FOM, FOM_{crit} and η for SHG of pulses with a free-space wavelength of 1.56 microns. The minimum pulse length for which FOM_{crit} and η for critically phasematched interactions are valid are also tabulated. For pulses shorter than these, the exact values for h must be taken from the Boyd and Kleinman analysis.

Table 2.5: Comparison of the ultrashort-pulse figure of merit (FOM) for several technologically important nonlinear materials. A fundamental wavelength of 1.56 μm is assumed for all calculations. For the efficiency, we also assume Gaussian pulses.

Material	Δn_g	FOM	FOM_{crit}	η for SHG	η Valid for
PPLN[15,16]	0.089	710 pm^2/V^2	-	165 %/nJ	-
PPLT[17]	0.068	320 pm^2/V^2	-	75 %/nJ	-
LiB_3O_5[15,18]	0.010	42 pm^2/V^2	-	10 %/nJ	-
$KNbO_3$[19,20]	0.053	-	800 pm^2/V^2	13 $\%\sqrt{ps}$/nJ	$\tau_l > 150$ fs
β-BaB_2O_4[15]	0.0029	-	330 pm^2/V^2	5 $\%\sqrt{ps}$/nJ	$\tau_l > 10$ fs
$LiIO_3$[15,21]	0.038	-	35 pm^2/V^2	0.6 $\%\sqrt{ps}$/nJ	$\tau_l > 100$ fs

It is clear from table 2.5 that QPM materials such as PPLN enable efficient frequency conversion; in addition, as we shall see in section 2.4, aperiodic-QPM materials also offer opportunities that are not available with non-QPM materials. However, a material's high performance at one wavelength does not necessarily imply that the same material is the best choice for other wavelengths. The GVM parameter, δv (or equivalently Δn_g), varies rapidly with wavelength. Also, the conversion efficiency, as in equation 2.80, depends explicitly on wavelength.

We now evaluate the FOM and the conversion efficiency for noncritically-phasematched ultrashort-pulse SHG in PPLN, PPLT and LBO for a range of wavelengths, as shown in figure 2.4. An interesting property of the dispersion of $LiNbO_3$ and $LiTaO_3$ is that it nearly can-

cels the explicit inverse-cubic wavelength-dependence in equation (2.80). Hence, the energy conversion efficiency for ultrashort-pulse SHG in PPLN and PPLT is nearly constant over all of the visible through near-infrared spectral region. The peak in efficiency for LBO near 1.26 μm (as well as near 2.3 μm for PPLN and PPLT) occurs because the GVM parameter vanishes at that wavelength, and therefore the optimum crystal length is infinitely long. Clearly, at this wavelength, either GVD or the realities of crystal growth would limit the usable crystal length to a more modest value.

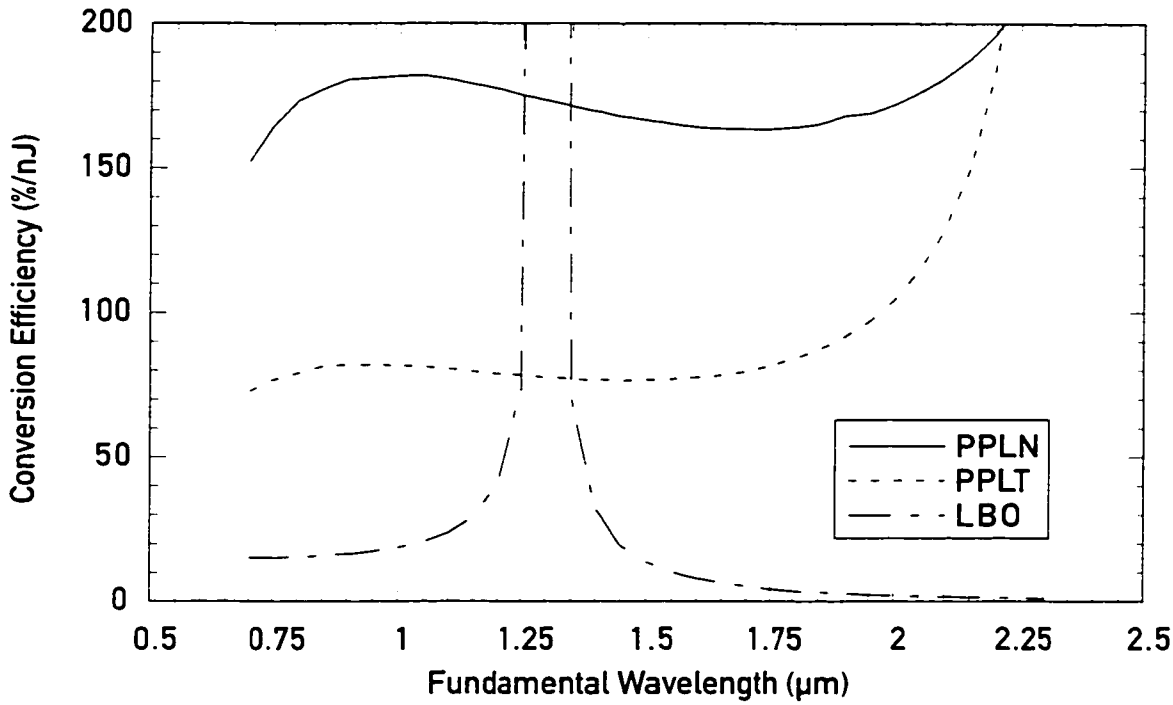

Figure 2.4: Conversion efficiency for ultrashort-pulse noncritically-phasematched SHG plotted against wavelength for three technologically important nonlinear materials. Transform-limited Gaussian pulses are assumed.

2.13 Aperiodic QPM gratings

The transfer function interpretation of equation (2.51) implies more than the spectral narrowing phenomenon considered in sections (2.7) through (2.9). Any arbitrary amplitude or phase structure on the SHG transfer function (tuning curve) will be imparted onto the SH output pulse. With quasi-phasematched interactions, both amplitude (through control of duty cycle) and phase (through variation of periodicity) structure can be engineered into the QPM grating. Then, both amplitude and phase structure can be engineered into the SHG transfer function because it is given by a Fourier transform of the QPM grating. In particular, a chirped QPM grating results in a transfer function with a phase structure that can cancel the phase of a chirped input pulse, or add any desired additional phase structure.

We begin an analysis of chirped QPM by assuming a grating with a slowly varying spatial frequency satisfying first-order quasi-phasematching at the center of the nonlinear material ($z = 0$) for the center frequency of the pulse, ω_1. The relevant component of this spatial distribution of the nonlinear coefficient can then be written in the form

$$d(z) = a_1 \exp[i\varphi(z)]\mathrm{rect}(z/L), \tag{2.89}$$

where the phase of the QPM grating is given by

$$\varphi(z) = \Delta k_0 z + D_{g2}z^2 + D_{g3}z^3 + \ldots \tag{2.90}$$

and where the prefactor a_1 represents the grating amplitude which was defined in equations (2.73) and (2.78). As we shall see shortly, compression of linearly chirped pulses can be obtained keeping only the first dispersive term in equation (2.90), in which case the local QPM period,

$$\Lambda_{local}(z) \equiv 2\pi\left[\frac{d}{dz}\varphi(z)\right]^{-1}, \tag{2.91}$$

is given by

$$\Lambda_{local}(z) = \frac{\Lambda_{QPM}}{1 + \Lambda_{QPM}D_{g2}z/\pi} \approx \Lambda_{QPM} - (\Lambda_{QPM})^2 D_{g2}z/\pi, \tag{2.92}$$

where $\Lambda_{QPM} = 2\pi m/\Delta k_0$ is the period of the carrier frequency of the QPM grating, as defined in section 2.10. Higher order terms in equation (2.90) can be used to correct higher order phase of the input pulse.

2.14 Linearly chirped QPM gratings

We will first analyze the simple case of QPM gratings with lowest-order chirp only. Hence $\Delta k_0 \neq 0$ and $D_{g2} \neq 0$, but all other chirp coefficients, $D_{g,l} = 0$. Substituting equations (2.89) and (2.90) into equation (2.54), we obtain

$$\hat{B}_2\left(\frac{L}{2}, \Omega\right) = \widehat{B_1^2}(0, \Omega) a_1 \Gamma \exp\left(\frac{-ik(\Omega + \omega_2)L}{2}\right) \int_{-\infty}^{\infty} \mathrm{rect}\left(\frac{z'}{L}\right) \exp(i[D_{g2} z'^2 - \Delta k_a(\Omega) z']) dz' \,, \tag{2.93}$$

with the definition $\Delta k_a(\Omega) \equiv \delta v \Omega + \delta\beta\Omega^2 + \tilde{k}_2(\Omega)$. We recognize the integral in equation (2.93) as the well known Fresnel integral. When the bandwidth of the tuning curve exceeds that of $\widehat{A_1^2}(\Omega)$, (i.e. when $L > L_{min}$, with $L_{min} \approx 3|\delta v / D_{g2}\tau_1|$), equation (2.93) can be accurately approximated over the spectrum of the pulse by the result for an infinitely long crystal,

$$\hat{B}_2(L/2, \Omega) = a_1 \Gamma \sqrt{\frac{\pi}{D_{g2}}} \exp\left(\frac{-ik(\Omega + \omega_2)L}{2}\right) \exp\left[i \frac{\Delta k_a^{\,2}(\Omega)}{4 D_{g2}}\right] \widehat{B_1^2}(0, \Omega), \tag{2.94}$$

where we have neglected a constant phase factor. We note that the first exponential term in equation (2.94) arises from dispersion at the SH frequency, while the second exponential term arises from the chirp of the QPM grating. In order to elucidate the role of group velocity mismatch (GVM) in the pulse compression mechanism, we will ignore GVD at both frequencies by taking $\delta\beta = \tilde{k}_2(\Omega) = 0$. (Note that the GVD at the fundamental frequency was assumed to be negligible by use of equations (2.51) and (2.54).) We also ignore constant and linear phase (time delay) factors on the spectrum, giving

$$\hat{B}_2(L/2, \Omega) = a_1 \Gamma \sqrt{\frac{\pi}{D_{g2}}} \exp\left[i \frac{\delta v^2 \Omega^2}{4 D_{g2}}\right] \widehat{B_1^2}(0, \Omega). \tag{2.95}$$

The form of equation (2.95) suggests an analogy between the chirp rate of the QPM grating, D_{g2}, and GVD. We find that for any input pulse shape, the second harmonic experiences an effective GVD of $-\delta v^2/2D_{g2}$ (and, therefore, can be compressed or stretched) relative to the fundamental pulse.

2.15 Compression of linearly chirped Gaussian pulses

As an example, we discuss the effect of the transfer function of equation (2.94) on a chirped Gaussian input pulse[22]. (We use equation (2.94) rather than (2.95) to fully account for the effects of GVD at the SH frequency.) In this section, we quantify pulse durations by the mathematically convenient $1/e$ power half-width, rather than the FWHM power duration that is conventional in the experimental literature and is used in section (2.9). We assume an input pulse which was created by dispersing a transform-limited Gaussian pulse with carrier frequency ω_1, $1/e$ power half-width τ_0 (and thus FWHM power duration of $\tau_1 = 2\sqrt{\ln 2}\tau_0$) and real (temporal peak) amplitude $B_{1,0}$ in a linear delay line with GVD of D_p. The electric field corresponding to this pulse at $z = 0$ is

$$E_1(z = 0, t) = B_{1,0}\frac{\tau_0}{\sqrt{\tau_0^2 - iD_p}}\exp\left[-\frac{t^2}{2(\tau_0^2 - iD_p)}\right]\exp(i\omega_1 t). \tag{2.96}$$

This pulse has a duration of

$$\tau = \sqrt{\tau_0^2 + (D_p/\tau_0)^2}. \tag{2.97}$$

Using equation (2.3) and defining a fundamental detuning as $\Omega_1 \equiv \omega - \omega_1$, we write the frequency domain envelope as

$$\hat{B}_1(0, \Omega_1) = \sqrt{2\pi}B_{1,0}\tau_0\exp[-\Omega_1^2(\tau_0^2 - iD_p)/2]. \tag{2.98}$$

Equations (2.94) and (2.95) call for $\widehat{B_1^2}(0, \Omega)$, which can be found from substituting equation (2.96) into equation (2.52) and Fourier transforming the square of the result, or from self-convolution of equation (2.98). In either case, we find

$$\widehat{B_1^2}(0,\Omega) = \sqrt{\pi}B_{1.0}^2\frac{\tau_0}{\tau}\sqrt{\tau_0^2 - iD_p}\exp\left[-\frac{1}{4}(\tau_0^2 - iD_p)\Omega^2\right]. \tag{2.99}$$

We substitute this expression for $\widehat{B_1^2}(0,\Omega)$ into equation (2.94) to find the second harmonic envelope at the output of the nonlinear crystal. We have, allowing for arbitrary dispersion at the SH frequency,

$$\hat{B}_2(L/2,\Omega) = a_1\pi\Gamma B_{1.0}^2\frac{\tau_0}{\tau}\sqrt{\frac{\tau_0^2 - iD_p}{D_{g2}}} \exp\left(-\frac{\tau_0^2\Omega^2}{4} + i\left[\frac{D_p\Omega^2}{4} + \frac{\Delta k_a^{\,2}(\Omega)}{4D_{g2}} - \frac{k(\Omega+\omega_2)L}{2}\right]\right). \tag{2.100}$$

The four terms in the exponential factor in equation (2.100) arise from the pulse shape, input pulse dispersion, chirp of the QPM grating and dispersion at the SH frequency, respectively. In order to find an analytical expression for the output second harmonic field in the time domain by inverse Fourier transformation of equation (2.100), we first drop all terms which depend on Ω with order higher than 2. Hence, we set $\tilde{k_2}(\Omega) = 0$ and, therefore, $\Delta k_a(\Omega) = \delta v\Omega + \delta\beta\Omega^2$. We also ignore the constant and linear phase (time delay) terms in $k(\Omega+\omega_2)$, as they do not affect the pulse shape. The frequency domain envelope (2.100) is then given by

$$\hat{B}_2(L/2,\Omega) = a_1\pi\Gamma B_{1.0}^2\frac{\tau_0}{\tau}\sqrt{\frac{\tau_0^2 - iD_p}{D_{g2}}}\exp\left(-\frac{\tau_0^2\Omega^2}{4} + i\left[\frac{D_p\Omega^2}{4} + \frac{(\delta v)^2\Omega^2 + 2\delta v\beta_2\Omega^3 + (\Delta\beta)^2\Omega^4}{4D_{g2}} - \frac{\beta_2\Omega^2 L}{2}\right]\right). \tag{2.101}$$

In equation (2.101) we note that terms which depend on Ω with order higher than 2 do not result from high-order dispersion terms, but rather from squaring $\Delta k_a(\Omega) = \delta v\Omega + \delta\beta\Omega^2$, as called for in equation (2.100). Although these terms represent real effects of GVD at the SH frequency, we desire a simple expression for the SH output pulse. We recognize that, for pulse lengths longer than ~10 fs, wavelengths in the near-IR and materials with GVD similar to that of PPLN, $2\beta_2\Omega/\delta v << 1$. (These conditions are met in all of the experiments described in this thesis.) Therefore, we drop the term which depends on Ω^4, as it is negligible for all frequencies Ω for which the pulse has significant Fourier amplitude when

$2\beta_2\Omega/\delta\nu << 1$. We also recognize that when the optimum QPM grating chirp, defined in equation (2.105), is used for D_{g2}, we can also drop the term which depends on Ω^3 under the same condition, $2\beta_2\Omega/\delta\nu << 1$. Finally, we inverse Fourier transform the result and find

$$B_2(L/2, t) = a_1\sqrt{\pi/D_{g2}}\Gamma B_{1.0}^2\frac{\tau_0}{\tau}\frac{\sqrt{\tau_0^2 - iD_p}}{\sqrt{\tau_0^2 - i2D_{SH}}}\exp\left\{\frac{t^2}{2[(\tau_0/\sqrt{2})^2 - iD_{SH}]}\right\}, \quad (2.102)$$

where

$$D_{SH} \equiv D_p/2 + (\delta\nu)^2/2D_{g2} - \beta_2 L. \quad (2.103)$$

We note that the chirp of the SH pulse depends on the chirp of the fundamental pulse, the chirp of the QPM grating and the GVD of the nonlinear material at the SH frequency. The length of the SH pulse is given by

$$\tau_{SH} = \sqrt{(\tau_0/\sqrt{2})^2 + (\sqrt{2}D_{SH}/\tau_0)^2}. \quad (2.104)$$

The result (2.104) is graphed in figure 2.5, where we have assumed that $\beta_2 = 0$. The durations of both the fundamental and the SH pulses are plotted against the chirp of the fundamental pulse (expressed in term of the delay line dispersion, D_p.) We see that the SH pulse is compressed when the fundamental pulse is highly chirped. The shift of the "v"-shaped pulse-duration curves represents the effective dispersion of the chirped QPM grating. An additional shift would arise from including the GVD of the nonlinear material at the SH frequency, as described by equation (2.103).

If the QPM grating is designed such that

$$D_{g2} = (\delta\nu)^2/(2\beta_2 L - D_p) \equiv D_{g2,opt}, \quad (2.105)$$

then the SH pulse has no chirp (is transform limited). The chirp on the input pulse, as well as the chirp caused by GVD at the SH frequency in the nonlinear material has been compensated. In this case, the SH is given, to within a constant phase factor, by

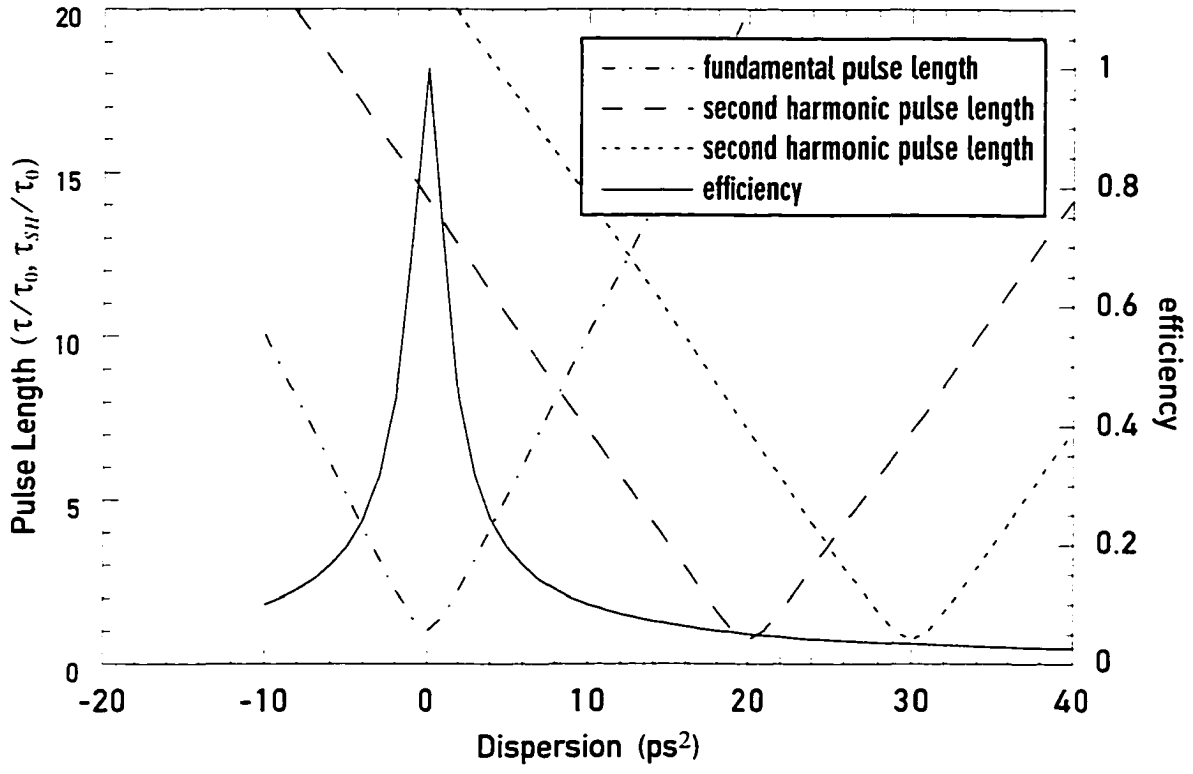

Figure 2.5: Normalized input (dashed-dotted curve, equation (2.97)) and output (equation (2.104)) pulse lengths plotted against the chirp of the input pulse (expressed in terms of the delay line dispersion) for plane-wave SHG in a chirped-QPM grating for $D_{g2} = -0.05(\delta\nu/\tau_0)^2$ (long-dashed curve) and for $D_{g2} = -0.033(\delta\nu/\tau_0)^2$ (short-dashed curve). Pulse lengths are normalized to the minimum fundamental pulse length, τ_0. The efficiency (solid curve, equation(2.109)) is normalized to its value for $D_p = 0$, which depends on the grating chirp, D_{g2}. Here, we have assumed $\beta_2 = 0$.

$$B_2(L/2, t) = a_1 \Gamma B_{1,0}^2 (\sqrt{\pi D_p}/\delta\nu)\sqrt{\tau_0/\tau}\exp(-t^2/\tau_0^2). \qquad (2.106)$$

2.16 Compression of arbitrary chirped pulses

The transfer function relation (2.54) implicitly gives the recipe for designing a QPM grating which compresses any input pulse for which GVD at the fundamental frequency can be neglected. (It also implicitly gives the recipe for pulse shaping examples other than pulse compression, though we will not discuss pulse shaping here. Pulse shaping using SHG in aperiodic QPM gratings is demonstrated in reference 23.) In general, the grating function required to

transform a given input to a desired output can be found by rearranging equation (2.54) and ignoring the irrelevant constant- and linear-phase (group delay) parts of $k(\Omega + \omega_2)$. We find

$$\hat{d}[\Delta k'(\Omega)] = \frac{1}{\Gamma}\exp\left[i\left(-\frac{\beta_2}{2}\Omega^2 + \tilde{k}_2(\Omega)\right)\frac{L}{2}\right]\frac{\hat{B}_2(L/2, \Omega)}{\hat{B}_1^2(0, \Omega)}, \tag{2.107}$$

where we are constrained by the maximum available nonlinear coefficient in any material (i.e. $|d[z]| \leq 1$). In equation (2.107), $\hat{B}_2(L/2, \Omega)$ is the Fourier transform of the envelope of the desired SH output pulse and $\widehat{B_1^2}(0, \Omega)$ is the Fourier transform of the square of the envelope of the known fundamental input pulse.

For compression, we require that the SH envelope has a constant phase, and therefore that

$$\angle\hat{d}[\Delta k'(\Omega)] = \angle\left[\frac{\exp(i[-(\beta_2/2)\Omega^2 + \tilde{k}_2(\Omega)]L/2)}{\widehat{B_1^2}[0, \Omega]}\right], \tag{2.108}$$

where $\angle F$ denotes the phase part of F. We must assume something about the magnitude of the transfer function to derive an explicit expression for $d(z)$ for any particular specific case of interest. A more detailed discussion of designing QPM gratings for compression of arbitrary pulses is beyond the scope of this thesis.

2.17 Efficiency of Pulse Compression

To calculate the efficiency of chirped-QPM-SHG, we return to equation (2.61), which gives the efficiency for plane-wave interactions in terms of the spectrum of the time-domain fundamental pulse envelope and the nonlinear material properties. (Note that the GVD at the SH frequency, β_2, is neglected in deriving equation (2.61).) Substituting equation (2.102) into equation (2.61), and using Parseval's theorem for Fourier transforms, we find

$$\eta_{E.PW} = \frac{\pi}{\sqrt{2}}\Gamma^2(B_{1.0}^2\tau_0)\frac{1}{\tau}\frac{1}{D_{g2}} = 1.4\eta_{E.0}\frac{(\delta\nu)^2}{\tau_0}\frac{1}{\tau}\frac{1}{D_{g2}}, \tag{2.109}$$

where

$$\eta_{E,0} = 1.6\Gamma^2(B_{1,0}^2\tau_0)[\tau_0/(\delta\nu)^2] \tag{2.110}$$

is the energy conversion efficiency for plane-wave SHG of unchirped pulses in a homogeneous (or periodic QPM) material of one group velocity walkoff length, $L_{walkoff} \equiv \tau_1/\delta\nu$. (Note that equation (2.110) is the same as equation (2.72), but in terms of the Gaussian pulses defined in this section and with all of the numerical factors evaluated explicitly.) The scaling of the efficiency depends on which experimental parameters are held constant. If the chirp on the QPM grating, D_{g2}, is fixed, $\eta_{E,PW}$ scales with the peak intensity of the stretched fundamental pulse, as shown in figure 2.6. However, if $D_{g2} \equiv D_{g2,opt}$ (with $\beta_2 = 0$) and $(\tau_0/\tau) << 1$, then $\eta_{E,PW} = 1.4\eta_{E,0}$, which no longer depends on the amount of stretching, τ/τ_0.

2.18 Efficiency of Pulse Compression with Focused Beams

Most applications for pulse compression require high efficiency and therefore confocal focusing of the fundamental beam in the nonlinear material. As in section 2.11, we approximate the efficiency for non-stationary confocally-focused SHG by treating temporal and spatial effects as independent. As discussed in section 2.11, this approximation is only valid in the quasi-static limit, or in the near-field limit, or both.

Equation (2.109) accounts for all of the temporal effects in which we are interested. In order to account for spatial effects, we begin by using Poynting's theorem,

$$I_p = \frac{1}{2} n_1 c \varepsilon_0 B_{1,0}^2, \tag{2.111}$$

to relate the (temporal) peak electric field, $B_{1,0}^2$, to the (temporal) peak fundamental intensity, I_p. We relate I_p to the (temporal) peak fundamental power, $P_{1,0}$, using an effective near-field beam area for confocally-focused Gaussian beams, a_{eff}, i.e. $I_p = P_{1,0}/a_{eff}$. We use the effective area for CW-SHG, $a_{eff} \equiv L\lambda_1/2hn_1$, where h is the Boyd & Kleinman[14] CW-SHG focusing factor. For confocally-focused Gaussian beams, $h = 0.8$. Thus we have

$$I_p = \frac{P_{1,0}}{L\lambda_1/1.6n_1}. \tag{2.112}$$

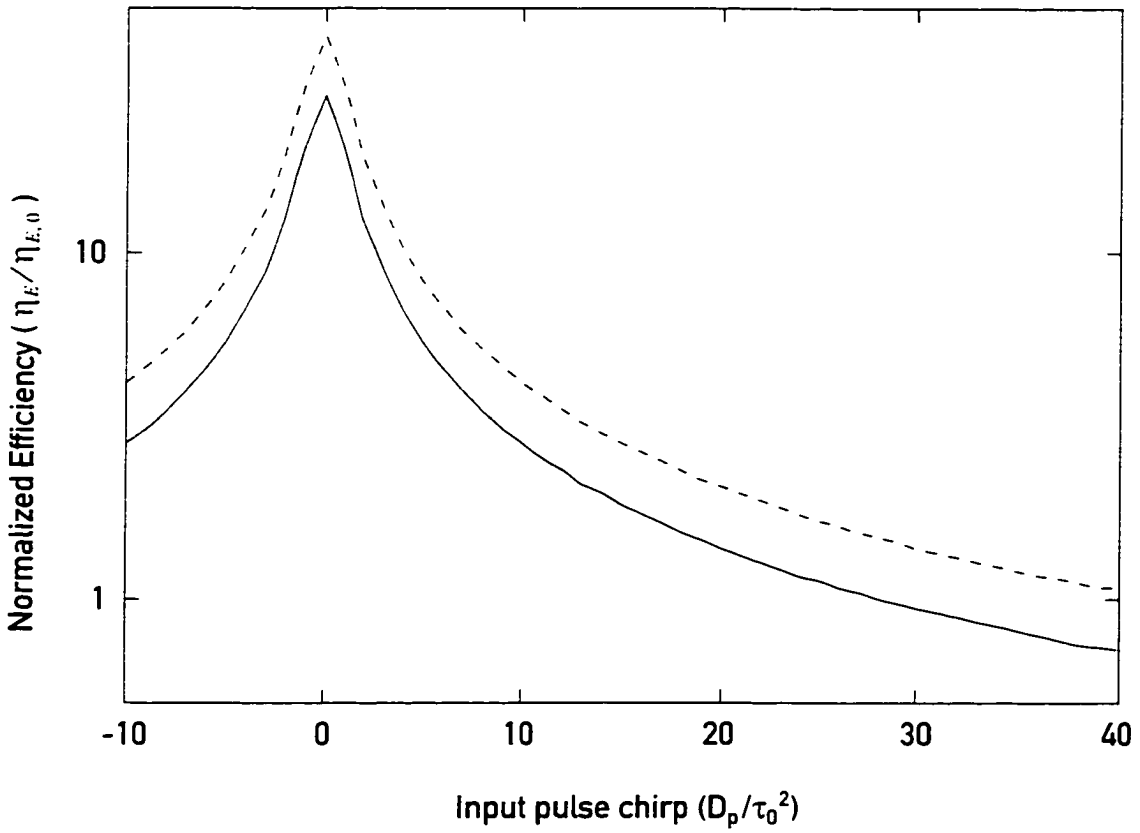

Figure 2.6: Normalized conversion efficiencies (equation (2.109)) plotted against the chirp of the input pulse (expressed in terms of the delay line dispersion) for plane-wave SHG in a chirped-QPM grating for $D_{g2} = -0.05(\delta\nu/\tau_0)^2$ (solid curve) and for $D_{g2} = -0.033(\delta\nu/\tau_0)^2$ (dashed-dotted curve). Here, efficiencies are normalized to that of unchirped pulses in homogeneous materials of optimum length, $\eta_{E,0}$.

Combining equations (2.111) and (2.112) to express $B_{1,0}^2$ in terms of $P_{1,0}$, and substitution into equation (2.109) gives the result for η_{conf}, the efficiency for confocal focusing,

$$\eta_{conf} = \frac{\pi}{\sqrt{2}}\Gamma^2\left(\frac{3.6P_p}{L\lambda_1 c\varepsilon_0}\right)\frac{\tau_0}{\tau}\frac{1}{D_{g2}}. \tag{2.113}$$

We now assume that the length of the crystal is chosen as the minimum length for which complete compression is possible, i.e. $L = L_{min} \approx 2|\delta\nu/(D_{g2}\tau_0)|$. Noting that $\Gamma^2 = 4\pi^2 d_{eff}^2/\lambda_1^2 n_2^2$ and $\delta\nu = \Delta n_g/c$ and using equation (2.82) we find

$$\eta_{conf} = 3.2\sqrt{2}\pi^3\left(\frac{1}{\varepsilon_0}\right)\mathrm{FOM}\left(\frac{P_p\tau_0}{\lambda_1^3}\right)\left(\frac{\tau_0}{\tau}\right). \tag{2.114}$$

We note that $\mathcal{E}_p = 1.77P_p\tau_0$ is the fundamental pulse energy for the Gaussian pulses we are considering here. (This relation is derived by integrating over time a Gaussian pulse with 1/e power half-width of τ_0 and peak power of P_p.) Therefore, we may write the conversion efficiency for confocally focused SHG of chirped Gaussian pulses in chirped-QPM materials of minimum length, L_{min}, as

$$\eta_{conf} = \frac{2.54\pi^3}{\varepsilon_0\lambda_1^3}\mathrm{FOM}\cdot\mathcal{E}_p\cdot\left(\frac{\tau_0}{\tau}\right). \tag{2.115}$$

Thus, in the confocally focused case, η_{conf} scales with the peak intensity of the stretched fundamental pulse, and therefore inversely with the stretch ratio, τ/τ_0. We recognize the similarity between equation (2.115) and equation (2.84), the result for confocally focused SHG of transform-limited Gaussian pulses in homogeneous materials of optimum length. A direct comparison reveals that, for the same fundamental pulse energy, the optimized chirped case ($L = L_{min}$) suffers an efficiency reduction of $0.8(\tau_0/\tau)$, as compared to the optimized unchirped case ($L = L_{opt}$, and $b = 0.617$.)

Recall that we have assumed that the crystal is long enough (given the QPM chirp rate, D_{g2}, which may or may not be appropriate for compression) such that its SHG transfer function has adequate bandwidth to match the fundamental pulse. We have also assumed that focusing is confocal over this length. However, it is important to note that in deriving equation (2.115), we have not assumed that $D_{g2} \equiv D_{g2,opt}$, (i.e. the SH pulse is not necessarily compressed relative to the fundamental).

From this analysis, we find the result that, for confocal focusing, the conversion efficiency depends significantly only on material constants (in proportion to the FOM) and on key input pulse properties (energy and stretching ratio, τ/τ_0). Surprisingly, the design of the chirped-QPM grating (for compression, stretching or neither) has little effect on the efficiency. While the above analysis was carried out only for chirped Gaussian pulses, we found in section 2.8 that for transform-limited pulses and homogeneous materials the pulse shape only

negligibly affects conversion efficiency. It is reasonable to expect similar pulse shape independence for the efficiency of chirped pulses and chirped-QPM materials.

With this observation in mind, using values from table 2.5 and noting the wavelength independence evident in figure 2.4, we may write the following approximate expression for the efficiency of ultrashort-pulse SHG in PPLN:

$$\eta \approx (\tau_0/\tau) \cdot E_p \cdot 100\%/\text{nJ}. \tag{2.116}$$

Many important laser systems which may be used as pump sources for the pulse compression process analyzed above have the property of being peak-power-limited. With such sources, the pulse energy increases linearly with pulse duration and, therefore, increases linearly with stretching for a fixed bandwidth. Thus, considering the result of equation (2.116), SHG of such sources has an energy conversion efficiency which is independent of stretching.

Laser systems which employ the chirped pulse amplification (CPA) technique for generation of high energy pulses are of great technological importance and typically operate in a peak-power-limited regime. CPA systems include a low power oscillator, a pulse stretcher, an amplifier and a pulse compressor. In most cases, the pulse compressor is inefficient and is one of the most expensive and most challenging components to implement. Use of chirped-QPM pulse compressors in CPA systems can offer solutions to all three of these problems. Because of the efficiency scaling rule described by equation (2.116), and because of the peak-power-limited nature of CPA systems, high conversion (and compression) efficiencies can be obtained over a wide range of stretched pulse durations.

2.19 Group velocity dispersion at the fundamental frequency

In highly dispersive materials, or with wide-bandwidth fundamental fields, the simple transfer function relationships (2.51) or (2.54) may no longer be accurate because they neglect GVD at the fundamental frequency. Instead, equation (2.49) may be used to describe the output SH envelope for any arbitrary fundamental field and QPM grating design. While this result is expressed in closed integral form, it is not expressible in an intuitively simple transfer function form.

It appears that equation (2.49) can be used in an iterative numerical algorithm to design an appropriate QPM grating for compression of chirped fundamental pulses. Discussion of a suitable numerical technique or further analytic investigation are beyond the scope of this thesis.

2.20 Summary of Chapter

In this chapter, we have developed a theory of quasi-phasematched ultrashort-pulse second harmonic generation in the undepleted-pump approximation. A frequency domain analysis has been used because it allows inclusion of arbitrary material dispersion properties. We have found that when GVD at the fundamental frequency can be neglected (a condition which easily is met for all experiments described in this thesis), a simple transfer function relationship describes the SHG process for arbitrary input pulses. This SHG transfer function depends only on material properties and on the QPM grating design.

The SHG transfer function relationship was applied to two important cases. First, we examined quantitatively the tradeoff between efficiency and pulse distortion when choosing the crystal length for ultrashort-pulse SHG. Second, we showed that chirped QPM gratings can be designed to generate transform-limited SH output pulses from arbitrarily chirped fundamental input pulses.

Finally, we analyzed the efficiency for ultrashort-pulse SHG that one can expect from various nonlinear materials with transform-limited input pulses and for chirped-QPM materials with chirped input pulses.

A table summarizing the notation used in this chapter is included in Appendix B.

References

[1]W. H. Glenn, "Second harmonic generation by picosecond optical pulses," IEEE Journal of Quantum Electronics **QE-5**, 284-290 (1969).

[2]E. Sidick, A. Knoesen and A. Dienes, "Ultrashort-pulse second harmonic generation in quasi-phasematched structures," Journal of the European Optical Society A: Pure and Applied Optics **5**, 709-722 (1996).

[3]J. Comly and E. Garmire, "Second harmonic generation from short pulses," Applied Physics Letters **12**, 7 (1968).

[4]S. A. Akhmanov, A. I. Kovrygin and A. P. Sukorukov, "Optical Harmonic Generation and Optical Frequency Multipliers," in *Quantum Electronics: A Tretise*, edited by H. Rabin and C. L. Tang (Academic Press, New York, 1975).

[5]S. A. Akhmanov, A. P. Sukhorukov and A. S. Chirkin, "Nonstationary Phenomena and Space-Time Analogy in Nonlinear Optics," Soviet Physics JETP **28**, 748-757 (1969).

[6]E. Sidick, A. Knoesen and A. Dienes, "Ultrashort-pulse second harmonic generation in quasi-phasematched dispersive media," Optics Letters **19**, 266-268 (1994).

[7]E. Sidick, A. Knoesen and A. Dienes, "Ultrashort-pulse second harmonic generation. I. Transform-limited fundamental pulses," Journal of the Optical Society of America B **12**, 1704-1712 (1995).

[8]E. Sidick, A. Knoesen and A. Dienes, "Ultrashort-pulse second harmonic generation. II. Non-transform-limited fundamental pulses," Journal of the Optical Society of America B **12**, 1713-1722 (1995).

[9]K. Mizuuchi, K. Yamamoto, M. Kato and H. Sato, "Broadening of the phase-matching bandwidth in quasi-phasematched second harmonic generation," IEEE Journal of Quantum Electronics **QE-30**, 1596 (1994).

[10]T. Suhara and H. Nishihara, "Theoretical analysis of waveguide second-harmonic generation phase matched with unifrom and chirped gratings," IEEE Journal of Quantum Electronics **QE-26**, 1265 (1990).

[11]M. L. Bortz, M. Fujimura and M. M. Fejer, "Increased acceptance bandwidth for quasi-

phasematched second harmonic generation in LiNbO3 waveguides," Electronics Letters **30**, 34 (1994).

[12]R. N. Bracewell, *The Fourier Transform and its Applications*, 2 ed. (McGraw-Hill, New York, 1986).

[13]S. K. Kurtz, "Measurement of Nonlinear Optical Susceptibilities," in *Quantum Electronics: A Tretise*, edited by H. Rabin and C. L. Tang (Academic Press, New York, 1975), Vol. I.

[14]G. D. Boyd and D. A. Kleinman, "Parametric interaction of focused Gaussian light beams," Journal of Applied Physics **39**, 3597-3639 (1968).

[15]P. F. Bordui and M. M. Fejer, "Inorganic Crystals for Nonlinear Optical Frequency Conversion," Annual Reviews of Material Science **23**, 321-379 (1993).

[16]D. H. Jundt, "Temperature-dependent Sellmeier equation for the index of refraction, n_e, in congruent lithium niobate," Optics Letters **22**, 1153 (1997).

[17]J.-P. Meyn and M. M. Fejer, "Tunable ultraviolet radiation by second harmonic generation in periodically poled lithium tantalate," Optics Letters **22**, 1214 (1997).

[18]D. N. Nikogosyan, "Lithium triborate (LBO): A review of its properties and applications," Applied Physics A **58**, 181-190 (1994).

[19]D. A. Roberts, "Simplified characterization of uniaxial and biaxial nonlinear optical crystals: a plea for standardization of nomenclature," IEEE Journal of Quantum Electronics **QE-28**, 2057-74 (1992).

[20]B. Zysset, I Biaggio and P. Gunter, "Refractive indices of orthorhombic $KNbO_3$. I. Dispersion and temperature dependence," Journal of the Optical Society of America B **9**, 380 (1992).

[21]V. G. Dmitriev, G. G. Gurzadyan and D. N. Nikogoysyan, *Handbook of Nonlinear Optical Crystals* (Springer-Verlag, Berlin, 1991).

[22]A. E. Siegman, *Lasers* (University Science Books, Mill Valley, CA., 1986).

[23]G. Imeshev, A. Galvanauskas, D. Harter, M. A. Arbore, M. Proctor and M. M. Fejer, "Engineerable femtosecond pulse shaping using second harmonic generation with Fourier synthetic quasi-phasematching gratings," to be published in Optics Letters **23**, (1998).

Chapter 3:Quasi-phasematched ultrashort-pulse second harmonic generation experiments

3.1 Introduction

In this chapter we describe efficient QPM-SHG of ultrashort (approximately 0.1-10 ps) pulses from modelocked erbium-doped fiber lasers using periodically-poled and chirped-period-poled lithium niobate (PPLN and CPPLN) as the nonlinear material. With these experiments, we demonstrate the high doubling efficiencies and the pulse compression predicted in chapter 2. We also demonstrate potentially simple and useful laser sources based on fiber lasers and QPM-SHG.

Diode-pumped passively modelocked erbium-doped fiber lasers (EDFLs) are compact and flexible sources of femtosecond pulses.[1-3] In contrast to bulk femtosecond lasers, erbium fiber lasers do not require bulk dispersion-compensating elements (because of the soliton pulses they support), enable the stable generation of pulses at low and adjustable repetition rates[4,5] (< 5 MHz - 2 GHz), and may easily be operated with broad-area diode pumps.[6-8] Two primary requirements for making fiber lasers attractive for many applications in ultrafast optics are pulse energy and wavelength compatibility with Ti:sapphire lasers.

The dominant limitation on the pulse energy that can be produced by fiber lasers is usually that imposed by self-phase-modulation. Typically, ~1 kW of peak power can be supported in single-mode fibers of realistic lengths (cm to meters). For sub-ps pulses, only sub-nJ pulse energies can therefore be realized. Chirped pulse amplification[9] (CPA) techniques have been used to generate nJ and μJ energies in all-fiber[10] and hybrid[11] systems, but at the cost of system complexity.

Because erbium lasers can produce femtosecond pulses in the wavelength range from 1530-1610 nm[12], frequency doubling can be used to reach 765-805 nm, a spectral region which spans the gain peak of Ti:sapphire and overlaps with the wavelengths commonly used

for several applications.[13] However, efficient frequency doubling is required for the production of the moderate-to-high pulse energies that some applications demand. Use of chirped-QPM in materials such as CPPLN for simultaneous SHG and pulse compression can be used to implement simple fiber-CPA systems which address both requirements described above without significantly increasing system complexity.

3.2 Efficient QPM-SHG with PPLN

Frequency-doubled EDFLs with output energies in the pJ range have been reported in the literature and are beginning to enter the commercial marketplace. However, these systems are limited by the low second harmonic generation (SHG) conversion efficiencies obtained with conventional nonlinear materials. For example, Lenz[14] reported a high-energy (1.8 nJ) externally-compressed stretched-pulse EDFL frequency-doubled in critically phasematched BBO generating 73 fs SH pulses with a conversion efficiency of 5%.

As discussed in chapter 2, we can improve on this efficiency using QPM-SHG in materials such as PPLN and PPLT. They can be used to provide noncritical phasematching anywhere within the transparency range of a material while taking advantage of the material's highest nonlinear coefficients. The advantages of QPM-SHG in the ps regime have been demonstrated by Pruneri.[15]

In our experiments we used a passively-modelocked erbium-doped fiber soliton oscillator, pumped with 150 mW (absorbed) from a 980 nm MOPA diode laser. The 1-meter-long single-mode fiber was doped with ~ 1000 ppm Er^{3+}. A large core diameter and high output coupling were chosen to keep circulating intensities low enough to minimize undesired nonlinear effects. The laser had a repetition rate of 88 MHz with an average output power of 50 mW.

The pulse spectrum, shown in figure 3.1, had a full width at half maximum (FWHM) bandwidth of 11.2 nm with characteristic secondary peaks indicating the presence of a pedestal. Figure 3.2 shows the oscillator pulse autocorrelation, indicating approximately $sech^2$-shaped pulses with FWHM durations of 230 fs, for a time-bandwidth product of 0.32. The autocorrelation (shown on a log scale) indicates that the pedestal component had low amplitude and therefore could not appreciably contribute to the SHG process. This pedestal, which was estimated to contain 14% of the total laser output using the technique of Dennis[16], can

be eliminated by operating at lower output power levels or with a stretched-pulse oscillator containing dispersion compensating components. However, in this experiment we could tolerate a small pedestal because the SHG process suppresses it at the SH wavelength, generating high quality pulses while retaining a simple overall system.

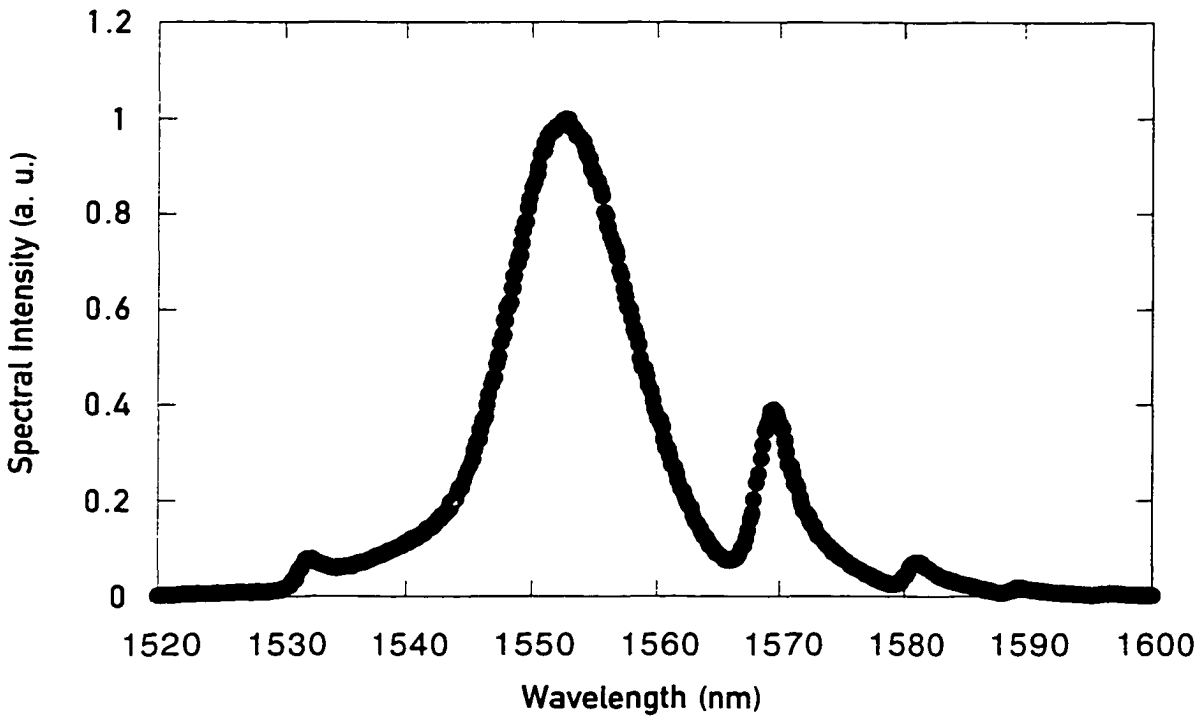

Figure 3.1: Measured fundamental pulse spectrum shown on a linear scale.

The 18.75-μm-period PPLN sample was fabricated by electric field poling[17] of a 0.5-mm-thick z-cut wafer of congruent lithium niobate. The laser output was focused with an achromatic doublet through a 1.1-mm-long ($\xi_{L_{max}} = 1$) polished sample cut from this wafer to a (1/e electric field radius) spot of 10 μm (verified at the focus with a knife-edge beam scan measurement). This focusing condition was slightly too tight for the interaction to occur in the near field because, despite the beam's single-mode fiber origin, the beam quality was not ideal. This non-ideal beam quality is most likely due to spherical aberration in the lens used to collimate the output of the fiber. (Confocally focused Gaussian beams in a crystal of this length would have an 11 μm spot.)

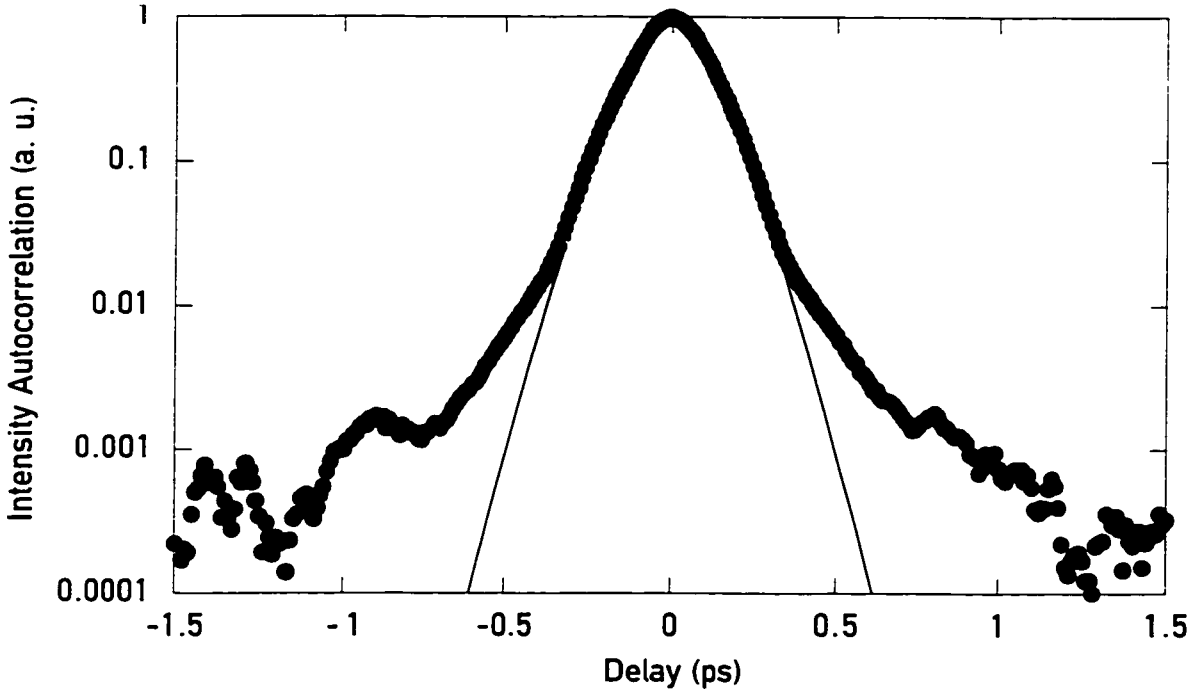

Figure 3.2: Measured fundamental pulse autocorrelation shown on a logarithmic scale. The solid line represents the theoretical autocorrelation of a pedestal-free sech^2 pulse with a FWHM duration of 230 fs.

The crystal was held at 80 degrees Celsius to eliminate small amounts of photorefractive damage observed at room temperature. All optical components, apart from the PPLN crystal and the doublet, were anti-reflection coated for the fundamental or second harmonic wavelength as appropriate. Of the 50 mW (0.49 nJ/pulse, plus pedestal) output of the oscillator, 37 mW (0.36 nJ/pulse, plus pedestal) was delivered inside the PPLN crystal. Average powers were measured with a calibrated germanium photodiode before the doublet for the fundamental and with a calibrated silicon photodiode after the crystal for the harmonic.

The spectrum of the frequency-doubled pulses, measured at the highest fundamental power levels and shown in figure 3.3, had a FWHM bandwidth of 4.7 nm. The autocorrelation is shown in figure 3.4; interpretation of the autocorrelation requires an assumption of the pulse shape. The results of chapter 2 indicate that the SH pulse shape which is generated, in the case of a sech^2 fundamental, depends on the length of the nonlinear crystal and varies smoothly between sech^4 (in the quasi-static limit) to square (in the highly non-stationary

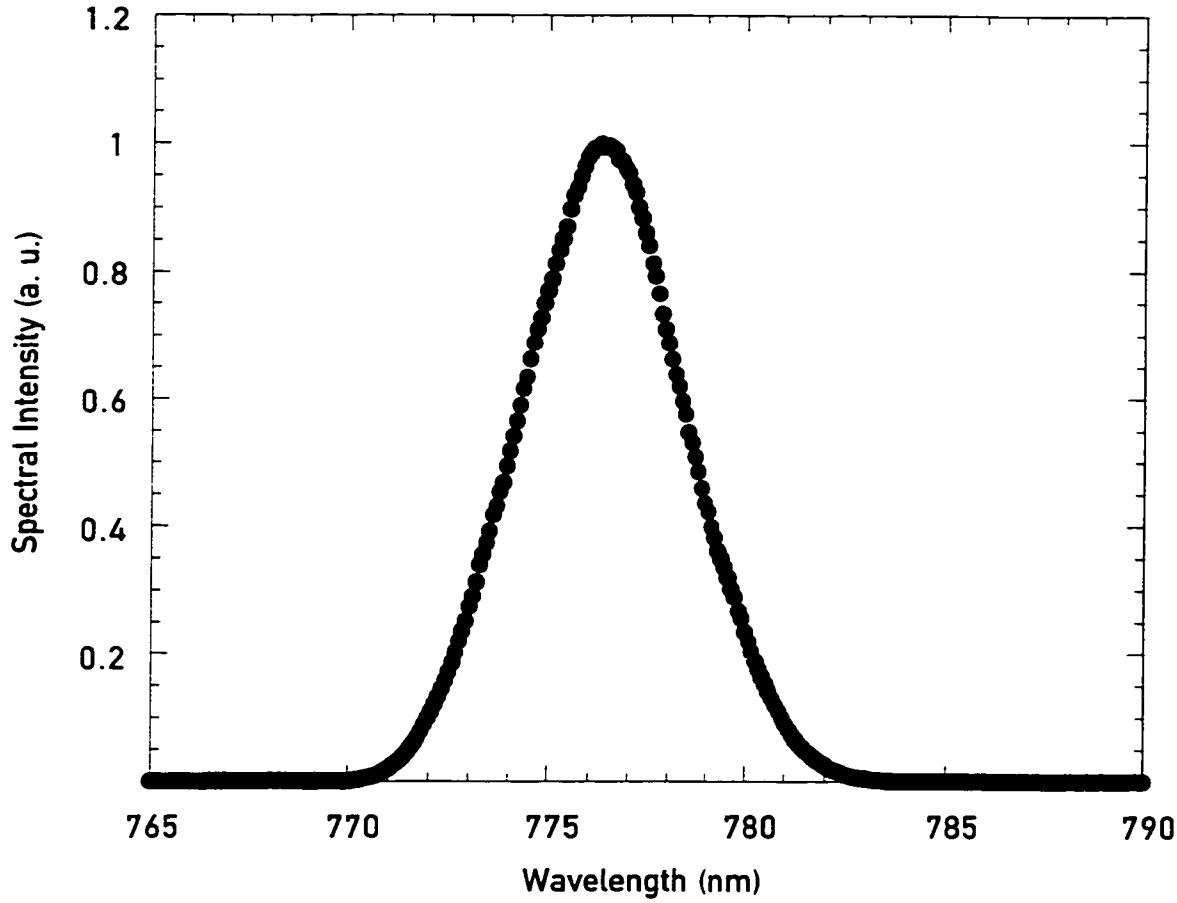

Figure 3.3: Measured SH pulse spectrum shown on a linear scale. Note that the spectrum is significantly "cleaner" than that of the fundamental.

limit). Because of our desire for high efficiency and limited pulse distortion, this experiment was performed in the crossover regime between the quasi-static and the non-stationary limits.

The spectrum and autocorrelation of the frequency-doubled pulses are similar (within the central peak, down to powers below 5% of the peak) to that of Gaussian pulses, which have a theoretical time-bandwidth product of 0.44. Using the Gaussian deconvolution factor of 0.707, we infer a FWHM pulse duration of 190 fs, giving an experimental time-bandwidth product of 0.44, confirming our assumed pulse shape. The measured SH-to-fundamental pulse length ratio of $\tau_{nor} = 0.83$ is consistent with a crystal length of 0.6 mm ($\xi_{L_{max}} = 0.55$), not with the actual crystal length of 1.1mm ($\xi_{L_{max}} = 1$).

Recalling the analysis of section 2.11, the transfer function interpretation requires that the interaction occurs in either the quasi-static limit or the near-field (no diffraction) limit, or

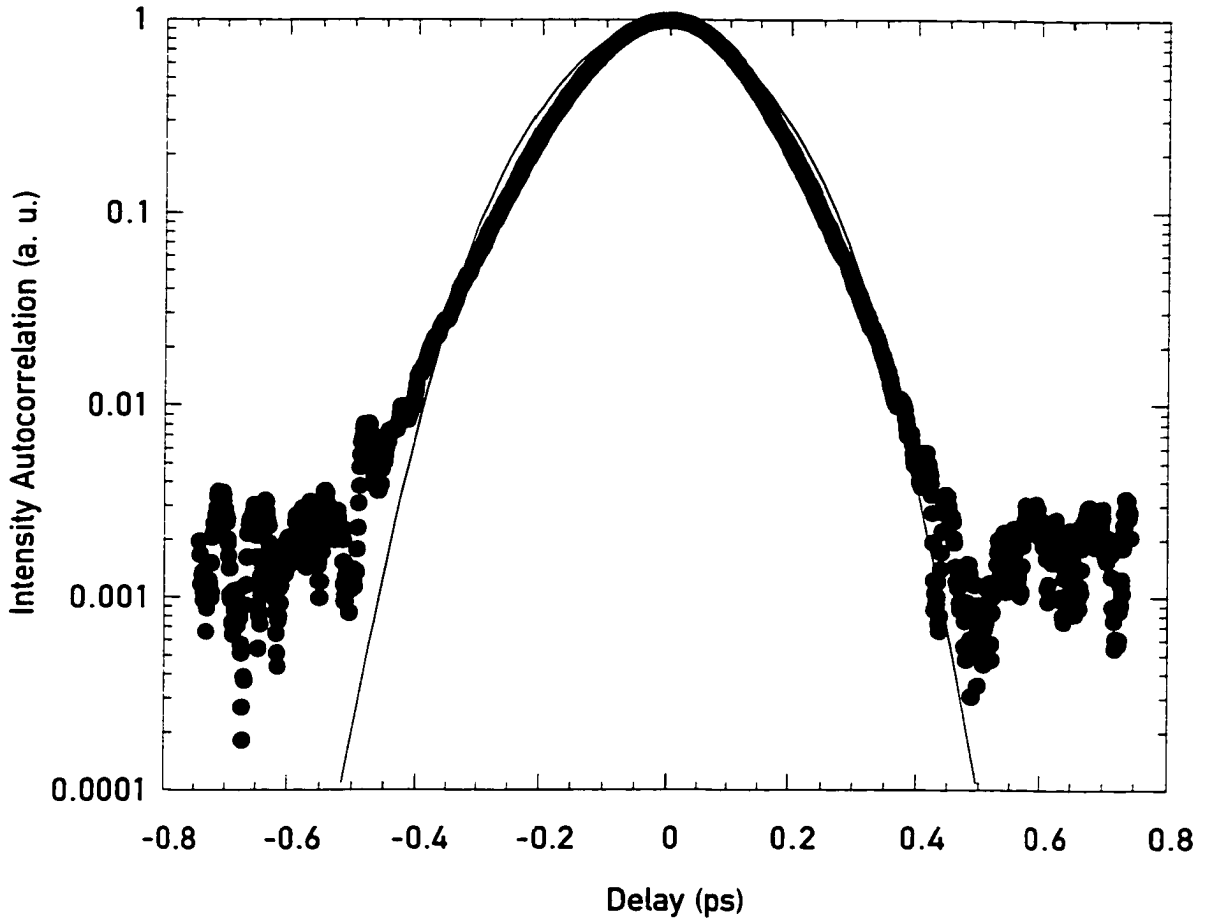

Figure 3.4: Measured SH pulse autocorrelation shown on a logarithmic scale. The solid line represents the theoretical autocorrelation of the second harmonic of the pulse in Figures 3.1 and 3.2 generated in a crystal with $\xi_{L_{max}} = 0.55$.

both. The transfer function is also based on the assumption of negligible pump depletion. In the experiment described above, none of these three requirements is met, though all are nearly met. An exact analysis of the experimental results would require a more sophisticated theory than that developed in chapter 2. Rather, we now assume that, for the purposes of interpreting our measured autocorrelation traces and spectra, we can model SHG in the PPLN crystal using an effective crystal length of 0.6 mm ($\xi_{L_{max}} = 0.55$).

The transfer function analysis of chapter 2 indicates that, with $\xi_{L_{max}} = 0.55$, there should be small, but non-negligible, group velocity walkoff. The SHG transfer function implies that the pulse shape should be transformed from sech^2 to a form which is approximately Gaussian within the central portion of the pulse, consistent with observations. Rather than use one of

these approximate forms, the theoretical curve plotted in figure 3.4 shows the numerically evaluated autocorrelation of the pulse shape predicted for $sech^2$ pulses and $\xi_{L_{max}} = 0.55$; this approximate autocorrelation agrees very well with the experimental data.

The average conversion efficiency was measured as a function of average power (adjusted with a waveplate-polarizer variable attenuator) in the PPLN crystal and is shown in figure 3.5. The small-signal internal conversion efficiency (obtained by accounting for reflection losses at the PPLN and doublet surfaces) observed was 0.77%/mW. The maximum second harmonic observed, for 37 mW internal pump power, was 7.0 mW for an internal efficiency of 22% and corresponded to 8.1 mW generated inside the crystal. As the low-amplitude pedestal is neither useful for most applications requiring the fundamental wavelength nor for second harmonic generation, only the energy content (approximately 86% of the total) in the ultrashort pulse itself is relevant. Therefore, it is more useful to evaluate the internal small-signal normalized conversion efficiency, $\eta_{E,ss}$, and internal maximum conversion efficiency of fundamental pulse energy, excluding the pedestal component, to harmonic pulse energy, which were 1.0%/mW (85 %/nJ) and 25%, respectively.

The small-signal efficiency predicted by equation (2.84) for confocally-focused SHG of $sech^2$ pulses in crystals of optimum length ($\xi_{L_{max}} = \xi_{L_{max,opt}} = 0.82$ and $\tau_{nor} = 1$) is 145 %/nJ. (See table 2.5). Alternatively, using the effective crystal length of ($\xi_{L_{max}} = 0.55$), which was proposed above, and using equation (2.80) to predict efficiency gives 95%/nJ, which is consistent with the experiment. The remaining discrepancy between the observed and the predicted efficiency for the limited effective crystal length ($\xi_{L_{max}} = 0.55$) can be explained by the imperfect domain structure of the PPLN sample used and by experimental error. The 25% average efficiency observed is high enough that the temporal and spatial peak of the pulse experienced significant pump depletion, as is evident in the efficiency saturation displayed in figure 3.5.

We can approximate the magnitude of the efficiency saturation by radially and temporally averaging the theoretical output intensity at each radius and time and assuming quasi-static, near-field interactions. For this calculation we use the expression for the efficiency of saturated plane wave SHG, $\tanh^2(\sqrt{\eta_{I,unsat}})$, averaged over the spatial and temporal profile of the fundamental pulse,

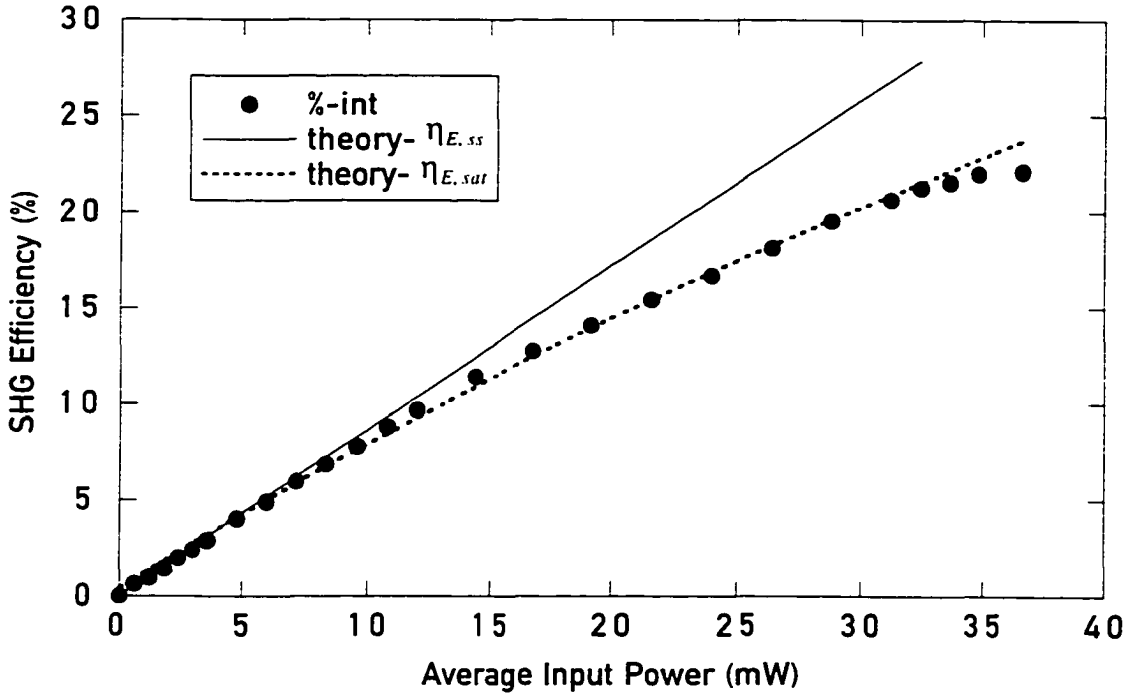

Figure 3.5: Internal SHG conversion efficiency plotted against internal average power at 1.56 μm. The solid line represents the small-signal conversion efficiency, $\eta_{E,ss}$, of 1.0%/mW (85 %/nJ). The dashed line was obtained using equation (3.1) and (3.4).

$$\eta_{E,sat} = \frac{\iiint I(x,y,t)\tanh^2(\sqrt{\eta_{I,unsat}[I(x,y,t)]})dxdydt}{\iiint I(x,y,t)dxdydt}. \tag{3.1}$$

where $\eta_{E,sat}$ is the average saturated energy conversion efficiency, $I(x, y, t)$ is the time- and position-dependent fundamental intensity and $\eta_{I,unsat}[I(x, y, t)]$ is the time- and position-dependent unsaturated intensity conversion efficiency. The time-domain analog of the analysis leading to equation (2.61) gives for $\eta_{I,unsat}$

$$\eta_{I,unsat}[I(x,y,t)] = [2/(nc\varepsilon_0)]\cdot\Gamma^2L^2I(x,y,t). \tag{3.2}$$

Before inserting equation (3.2) into equation (3.1), it is convenient to relate the unsaturated intensity conversion efficiency, $\eta_{I,unsat}$, to the small signal average energy conversion efficiency, $\eta_{E,ss}$. In order to proceed, we must specify $I(x, y, t)$. We assume that $I(x, y, t)$ has a

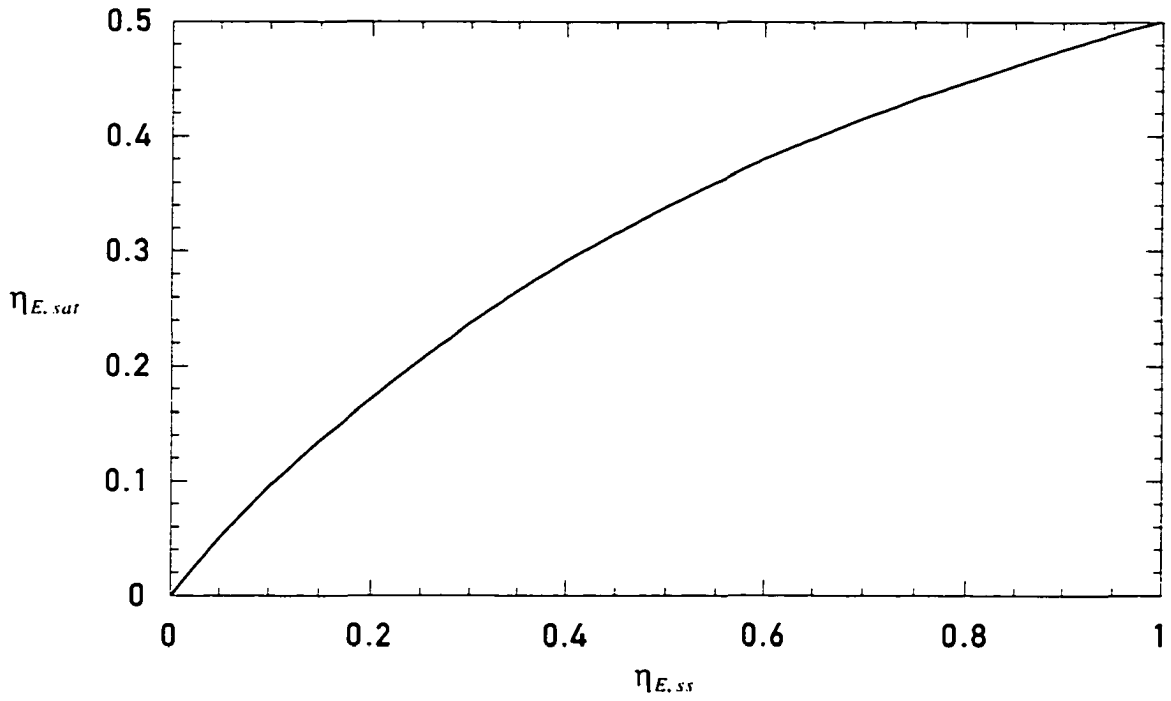

Figure 3.6: Approximation to the saturated conversion energy efficiency, $\eta_{E.sat}$, based on equation (3.1) and the assumption of sech^2 pulses and Gaussian beams. $\eta_{E.ss}$ is the small-signal (unsaturated) approximation to the energy conversion efficiency.

sech^2 temporal form and a Gaussian spatial form. Evaluating equation (3.1) in the small-signal limit ($\tanh^2\sqrt{\eta} \to \eta$ and $\eta_{E.sat} \to \eta_{E.ss}$) allows for analytical integration of equation (3.1) and yields the relation

$$\eta_{E.ss} = \frac{1}{\pi}\left[\frac{2}{(nc\varepsilon_0)}\right] \cdot \Gamma^2 L^2 . \tag{3.3}$$

Therefore, we find with equations (3.2) and (3.3)

$$\eta_{I.unsat}[I(x, y, t)] = \pi \cdot \eta_{E.ss} \cdot I(x, y, t) . \tag{3.4}$$

Finally, we note that equation (3.1) is exact for the case of quasi-static, loosely focused interactions.

The dashed line in figure 3.5 was obtained using equation (3.1) with the assumed sech^2 temporal form and Gaussian spatial form, equation (3.4) and $\eta_{E.ss} = 85\%/\text{nJ} \cdot \mathcal{E}_p\,(\text{nJ})$.

Since the experimental data agrees well with this calculation, we conclude that at least for conversion efficiencies below 25%, the approximation described in equation (3.1) is reasonably accurate, even for confocal focusing. In figure 3.6, $\eta_{E,sat}$ is plotted against $\eta_{E,ss}$ over a wider range of small-signal conversion efficiencies. We find that when the "small-signal" energy conversion efficiency approaches 100%, the conversion efficiency predicted by equation (3.1) is only 50%.

3.3 Pulse compression with chirped-QPM SHG

As we discussed in sections 2.13 through 2.18, chirped-QPM SHG can be used to simultaneously frequency double and compress ultrashort pulses. To experimentally demonstrate this physical phenomenon, we used a 5-cm-long sample of electric-field-poled CPPLN with local QPM periods varying linearly from 18.2-19.8 μm ($D_{g2} \cong 0.28$ mm^{-2}). The SHG acceptance bandwidth was measured with a tunable CW source to be about 50 nm at the fundamental wavelength; thus the sample is capable of generating SH pulses with up to a 25 nm bandwidth.

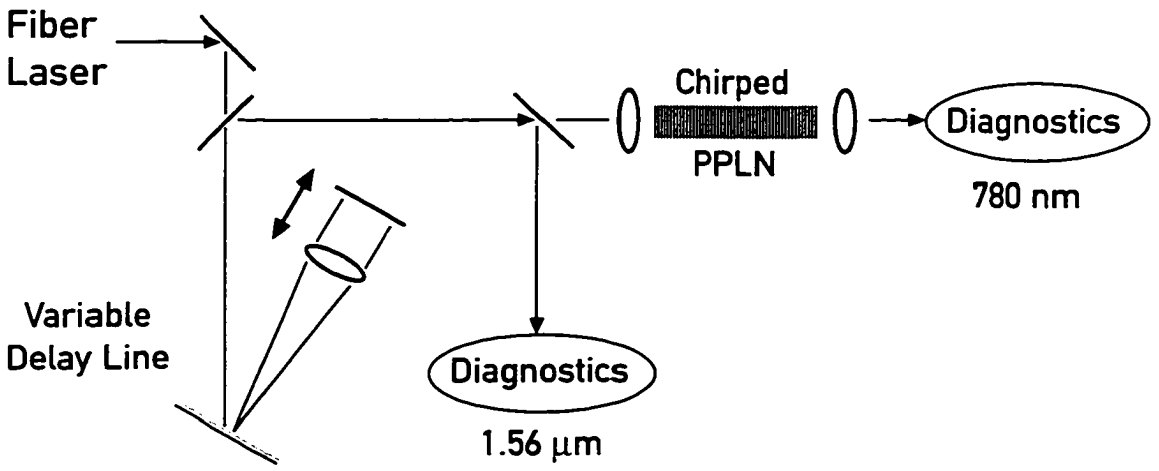

Figure 3.7: Experimental apparatus for demonstrating pulse compression during chirped-QPM SHG. A diffraction-grating-based variable delay line served the function of providing fundamental pulses with adjustable positive or negative chirp. Diagnostics included measurements of average power, spectra and autocorrelations.

The output from an amplified erbium-doped fiber laser was self-phase-modulated to produce pulses at a 20 MHz repetition rate and with 75-nm-wide, approximately square spectra with a center wavelength of 1560 nm and negligible high-order dispersion. These pulses were stretched with a diffraction-grating delay line containing a telescope in the Martinez[18] configuration to provide continuously variable GVD. The delay line had negligible high-order dispersion. The fundamental beam was loosely focused through the sample to a spot with 1/e electric-field radius of approximately 100 μm (confocal focusing for this crystal length requires a 75 μm 1/e electric-field radius). The autocorrelations and spectra of the fundamental and SH pulses were measured before and after the CPPLN crystal, respectively. The SH spectra typically had a 16-nm-wide square-like shape for various pulse lengths, consistent with the observed triangular autocorrelations for the stretched SH pulses.

Figure 3.8(a) shows an autocorrelation trace of the SH pulses for D_p = 0.29 ps^2, giving an autocorrelation width of 150 fs. The square-shaped SH spectrum has a deconvolution factor of 0.75, implying pulse durations of 110 fs (FWHM). The theoretical FWHM pulse duration for transform-limited, 16-nm-wide (at 780 nm) spectra is 105 fs, indicating that, at least in the low conversion efficiency limit investigated by this experiment, negligible undesired high order chirp is introduced by the nonlinear interaction. The fundamental pulses input to the CPPLN sample under these conditions had durations (and autocorrelation widths) of 17 ps (FWHM). An autocorrelation trace for the fundamental pulses for D_p = 0.29 ps^2 is shown in figure 3.8(b).

In order to demonstrate more clearly the effective GVD properties of chirped QPM gratings, we measured autocorrelation widths for the input fundamental pulses and the output SH pulses for various delay line positions; the results are shown in figure 3.9(a). The fundamental pulse FWHM duration was varied from 1 ps (with net negative chirp) to 95 fs at zero dispersion to 19 ps (with net positive chirp). The solid lines matching the autocorrelation data are the numerically evaluated autocorrelation widths for square (75 nm wide at 1560 nm and 16 nm wide at 780 nm) spectra with negligible high-order chirp. Figure 3.9(b) shows the SH autocorrelation widths near the maximum compression point.

The width of the SH spectrum (16 nm) is approximately 65 % of that allowed by the phasematching bandwidth of the CPPLN sample (25 nm). We attribute this spectral narrowing to the non-ideal chirp in the wings of the fundamental pulse spectrum (resulting from the

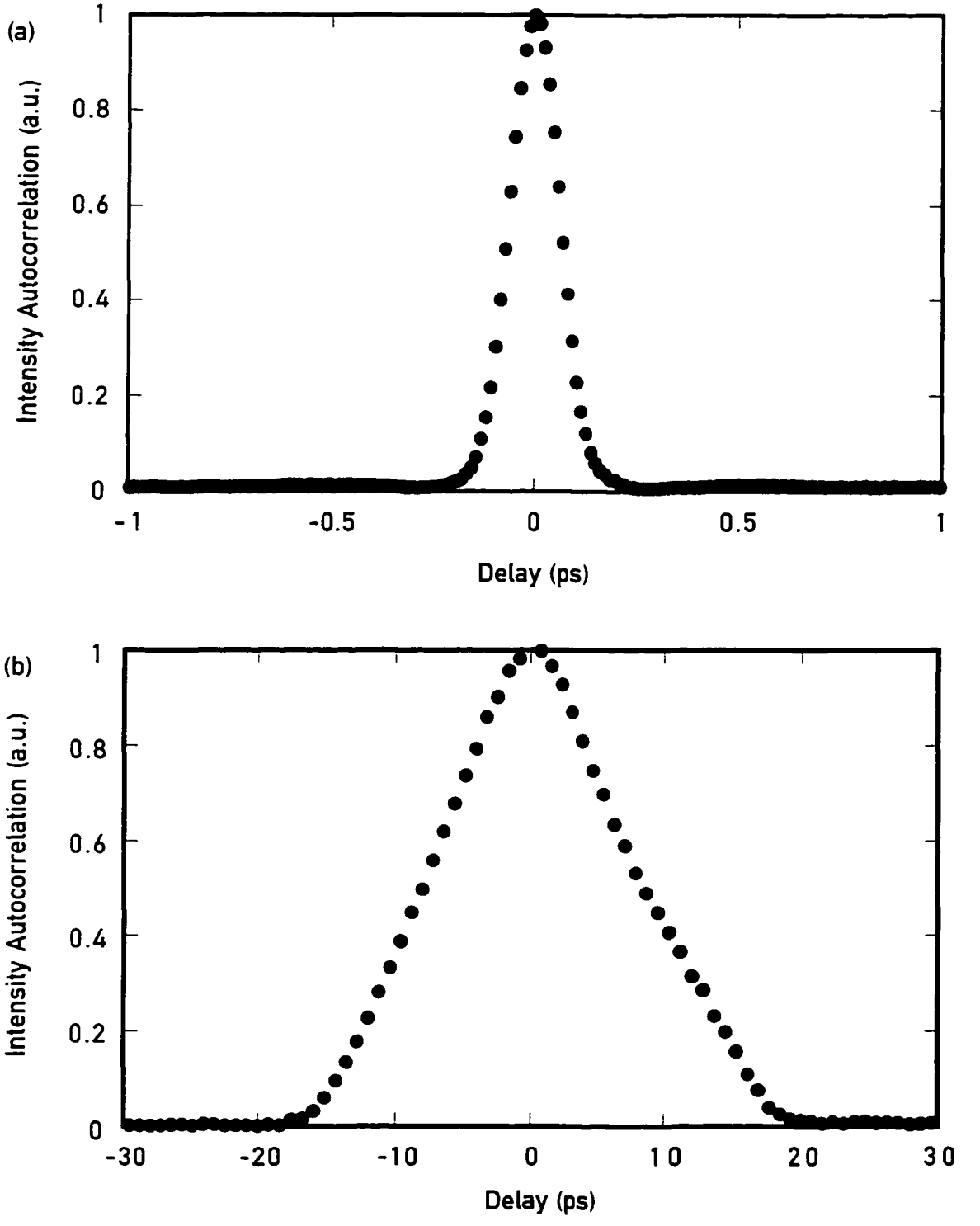

Figure 3.8: (a) Autocorrelation trace of the SH pulses at maximum compression (D_p = 0.29 ps^2), giving an autocorrelation duration of 150 fs and a pulse width of 110 fs (FWHM). (b) Autocorrelation trace of the fundamental pulses for D_p = 0.29 ps^2, giving an autocorrelation width of 17 ps and a pulse width of 17 ps (FWHM).

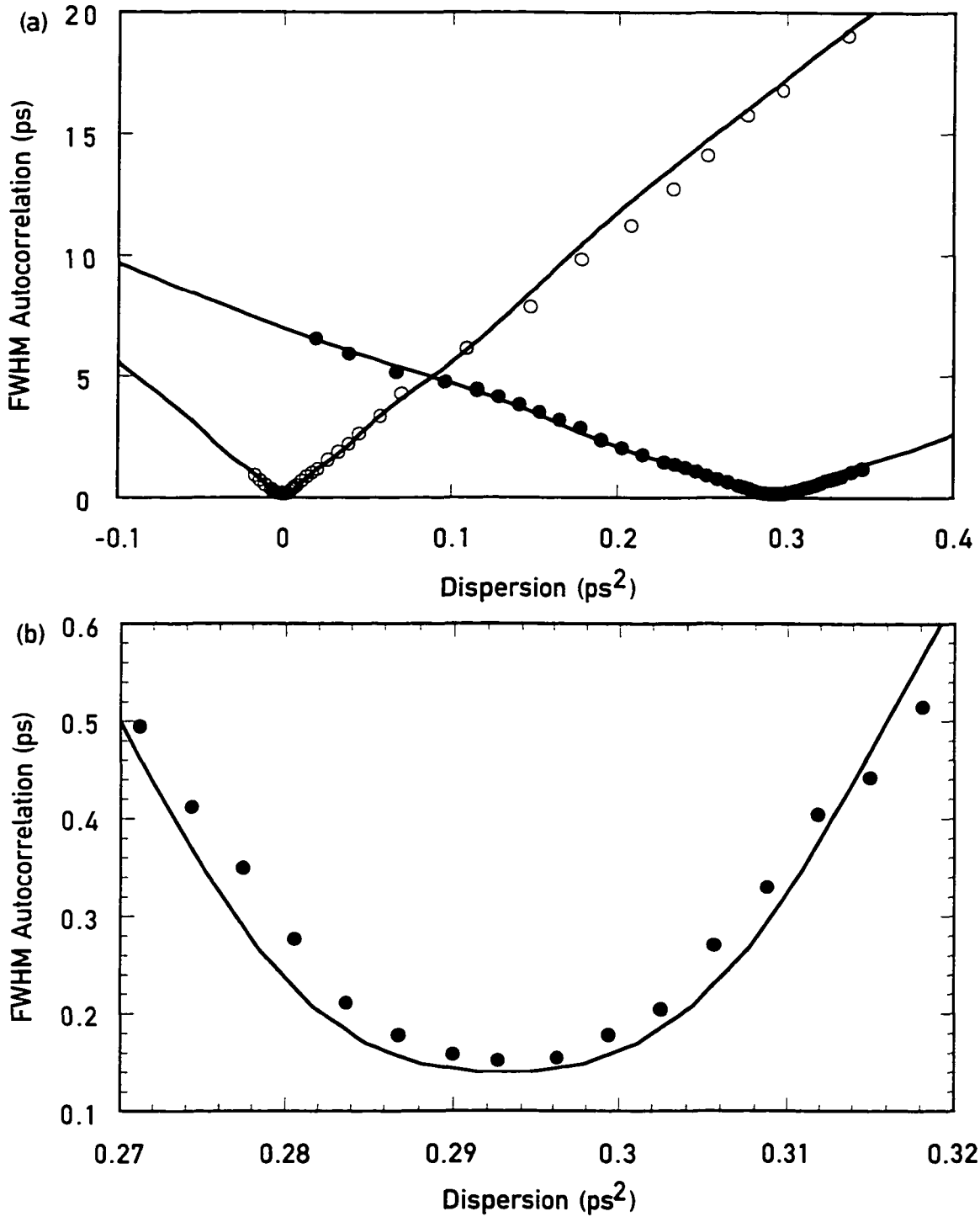

Figure 3.9: (a) Input (circles) and output (dots) autocorrelation widths plotted against the chirp of the input pulse (expressed in terms of delay line GVD) for SHG in a chirped QPM grating with $D_{g2} \cong 0.28$ mm^{-2}. Lines are theoretical predictions based on square spectra with 75 nm width at 1560 nm and 16 nm width at 780 nm. (b) Expanded plot of the SH pulse autocorrelations near maximum compression for the conditions described in (a).

use of self-phase-modulation in a fiber to increase the pulse bandwidth) and to the spatial chirp in one transverse dimension of the fundamental beam (resulting from the simple single-grating design of the variable delay line). In section 3.3, we demonstrate that the use of cleaner input fundamental pulses stretched in an optical fiber alleviates both of these experimental limitations. The difference in the slope of the SH autocorrelation curve relative to the slope of the fundamental autocorrelation curve reflects the fact that the SH spectrum did not have precisely twice (half) of the frequency (wavelength) bandwidth of the fundamental pulse.

To find the optimum input pulse chirp, $1/D_{p,opt}$, we rearrange equation (2.105) to define

$$D_{p,opt} \equiv -\frac{(\delta\nu)^2}{D_{g2}} + 2\beta_2 L. \tag{3.5}$$

The SH pulses had a minimum duration when D_p = 0.29 ps^2 (experimental uncertainty of ~5%), which is in exact agreement with $D_{p,opt}$ = 0.29 ps^2 predicted by equation (3.5) using the CPPLN material constants $\delta\nu$ = –0.3 ps/mm and β_2 = –0.0004 ps^2/mm for 1560 nm SHG and using $D_{g2} \equiv -0.28$ mm^{-2} for the crystal oriented to give compression. The sign of $D_{p,opt}$ depended, as expected, on the sample orientation, and the magnitude of $D_{p,opt}$ scaled approximately with D_{g2} when alternate CPPLN crystals were substituted.

Figure 3.10 shows the normalized average-power conversion efficiency measured at low absolute efficiencies (i.e. low-energy pump) and plotted against the chirp of the input pulses. The solid line in figure 3.10 is a fit (with the bandwidth of the fundamental pulse, expressed as $1/\tau_0$, as the fit parameter) to equation (2.109), the theoretical efficiency for a dispersed Gaussian pulse. This simple analytical form was used because the experimental conditions described above (non-ideal input spectra and beams with spatial chirp) precluded more detailed calculation of the efficiency. The SH bandwidth extracted from this fit is 18 nm FWHM, (corresponding to 50 fs FWHM Gaussian pulses or 100 fs FWHM square-spectrum pulses) in reasonable agreement with the 16 nm FWHM that was measured. The highest energy conversion efficiency observed was 110 %/nJ, comparable to that which can be obtained with transform-limited pulses and unchirped PPLN and consistent with that expected for these experimental conditions.

In these experiments, the pulse energy was held fixed as the GVD of the delay line used to prepare the pulses was adjusted. In the next section, we describe an experimental situation

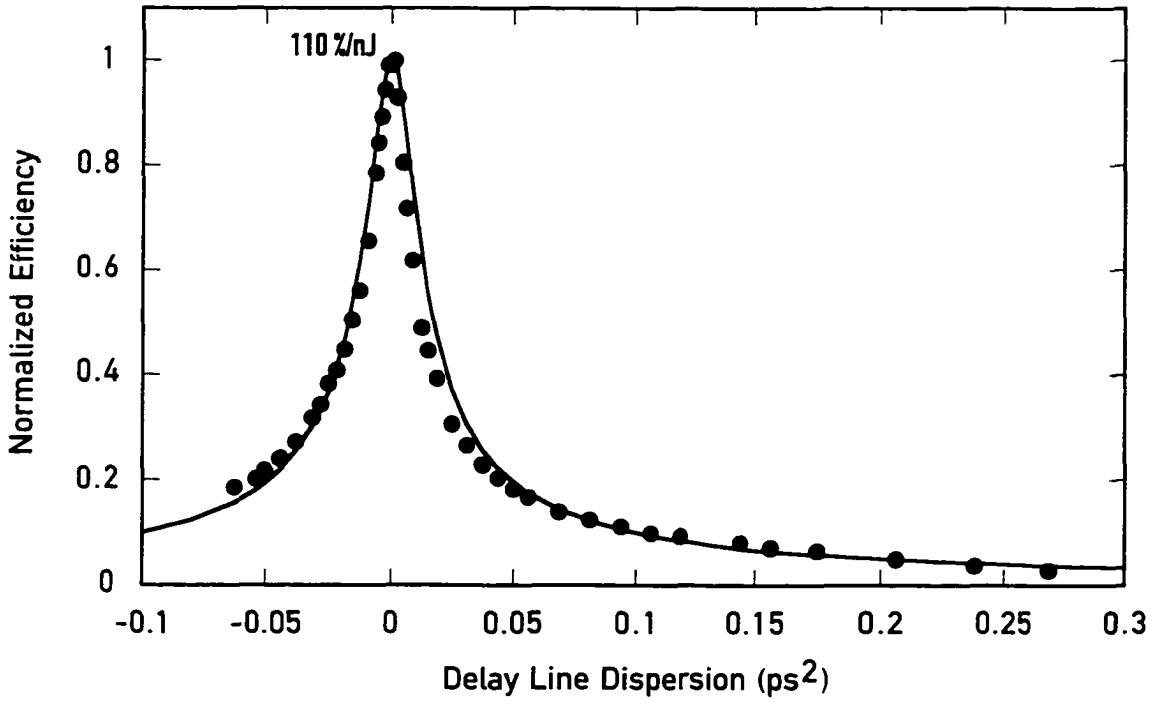

Figure 3.10: Efficiency plotted against delay line dispersion. The solid line is a plot of theoretical efficiency approximated by that for pulses with a 25 nm (FWHM) Gaussian fundamental spectrum (18 nm SH spectrum), normalized to the peak experimental value.

where we were able to increase the pulse energy roughly in proportion to the stretching ratio (τ/τ_0) of the fundamental pulses. This situation maintains constant (and high) conversion efficiency despite the changes in normalized (with respect to pulse energy) conversion efficiency that accompany pulse stretching.

3.4 Fiber-CPA system experiments using chirped-QPM SHG

In this section we describe a practical system which combines the results of section 3.2 (highly efficient SHG using PPLN) and section 3.3 (pulse compression using chirped-QPM) to address the practical issues regarding ultrashort-pulse fiber lasers described in section 3.1 (need for moderate-high pulse energies and wavelength compatibility with applications).

The experimental system was comprised of an erbium-doped fiber oscillator, a short length of single-mode fiber serving as a pulse stretcher, a large-core erbium-doped fiber amplifier and

a chirped-PPLN pulse compressor, as shown in figure 3.11. The oscillator produced 200 fs (FWHM) pulses with 250 pJ of energy at a 20 MHz repetition rate. The stretcher consisted of 3 meters of positive-dispersion fiber with a GVD at 1560 nm of $\beta_2 = 0.108\ ps^2/m$. The pulses were amplified in a 1.2 meter long erbium-doped fiber with a GVD at 1560 nm of $\beta_2 \approx -0.02\ ps^2/m$, for a net system dispersion of $D_p \approx 0.30 ps^2$. The pulses exiting the amplifier had durations of 2.2 ps (FWHM).

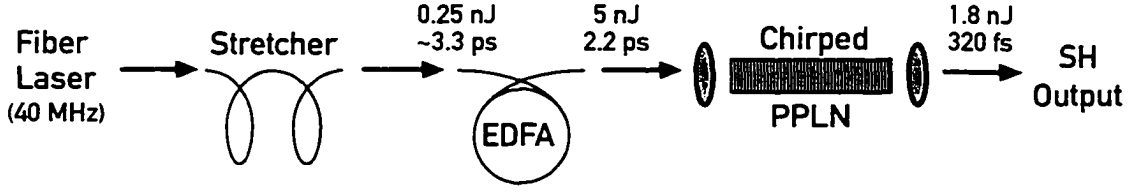

Figure 3.11: Schematic diagram of a simple fiber-CPPLN chirped pulse amplification system which produced 70 mW of average power 320 fs pulses at 780 nm.

The amplifier fiber was in-core pumped at 980 nm using a 750 mW single-mode beam from a master-oscillator-power-amplifier diode laser. The amplifier fiber length was chosen as a compromise between minimizing nonlinear effects (requiring short lengths) and maximizing pump light absorption and output power (requiring long lengths). With the 1.2 meter long amplifier fiber, we obtained 200 mW of average power (10 nJ/pulse) at 1560 nm. The pulses exiting the amplifier had narrower bandwidth than those exiting the oscillator because of a mismatch between the oscillator and amplifier gain spectra.

The CPPLN compressor was 2 cm long, with a QPM grating period chirped linearly from 18.68-19.32 μm ($D_{g2} \cong 0.28 mm^{-2}$). Equation (3.5) predicts $D_{p,opt} = 0.31 ps^2$. The fundamental beam was focused confocally through the CPPLN sample. Figure 3.12 shows the average internal (corrected for Fresnel reflections at the uncoated endfaces) SH power plotted against the average internal fundamental power. Nearly transform-limited pulses with a FWHM duration of 320 fs and an average power of 70 mW (3.5 nJ/pulse) were generated with a (saturated) 35 % conversion efficiency. The small-signal conversion efficiency of 14 %/nJ is in exact agreement with equation (2.116) for the pulse stretching ratio used in this experiment, $\tau/\tau_0 \cong 2.2/0.32 = 7$.

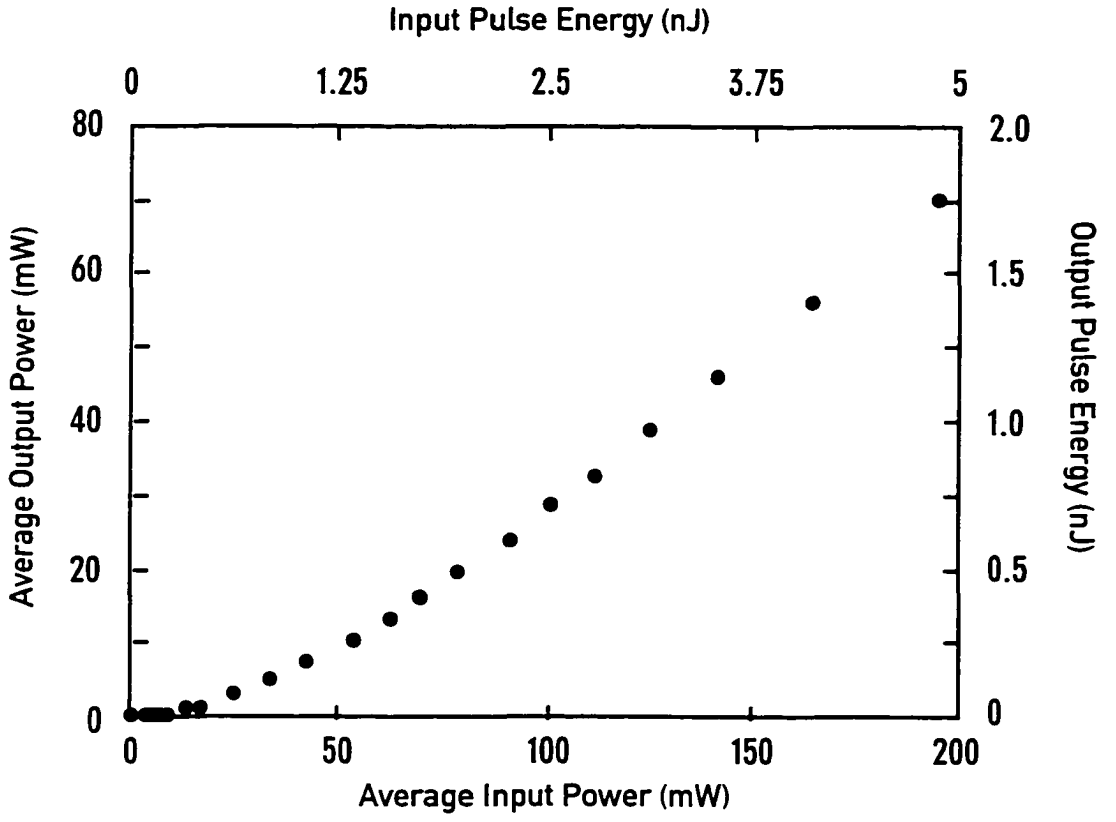

Figure 3.12: Average internal (corrected for Fresnel reflections at the uncoated endfaces) SH power plotted against the average internal fundamental power.

More recent experiments[19] using CPPLN pulse compressors and optimized (double-clad, Yb/Er co-doped, very large core) amplifier fibers have demonstrated generation of 500 mW of average power, 780 nm femtosecond pulses. Laser systems similar to these may offer a simple, compact, robust, efficient, and potentially inexpensive alternative to Ti:Sapphire oscillators.

3.5 Advantages of chirped-QPM

To put the above experiments into context, we list several reasons why CPPLN-based pulse compressors are superior to conventional prism-based or diffraction-grating-based pulse compressors. CPPLN devices are monolithic, alignment-free and extremely compact. (The device used in the experiment described in section 3.4 occupied a volume of only 0.5 mm x 0.5 mm x 20 mm.) CPPLN devices are mass producible and potentially very inexpensive. Correction of arbitrary high-order dispersion is as easy to implement as simple GVD correc-

tion. Finally, SHG conversion efficiencies can be comparable to the transmission efficiency of typical diffraction-grating-based compressors and higher than that of the conventional combination of a compressor followed by a nonlinear crystal.

3.6 Summary of Chapter

In this chapter, we have described experiments which demonstrate that quasi-phasematched ultrashort-pulse second harmonic generation is both efficient and versatile. Diode-pumped erbium-doped fiber lasers (EDFLs) generating femtosecond pulses with a 1560 nm wavelength were combined with PPLN and CPPLN frequency doublers to demonstrate simple and practical laser systems.

In particular, we demonstrated generation of 8.1 mW of 190 fs, 777 nm pulses at an 88 MHz repetition rate at an energy conversion efficiency of 25% using direct frequency doubling of a passively mode-locked fiber oscillator.

We have also shown that chirped quasi-phasematching gratings can be used for simultaneous second harmonic generation and ultrashort pulse compression. We have generated 110 fs (FWHM) near-transform-limited pulses with 150-fold compression relative to the input pulses; output pulse duration and efficiency results are in good agreement with expectations.

Finally, we showed that the combination of an erbium-doped fiber oscillator, a single-mode fiber pulse stretcher, an erbium-doped fiber amplifier and a chirped-PPLN pulse compressor can comprise a simple and robust source of moderate-energy (several nJ) ultrashort (~250 fs) pulses.

References

[1]M. E. Fermann, A. Galvanauskas, G. Sucha and D. Harter, "Fiber-lasers for ultrafast optics," Applied Physics B (Lasers and Optics) **B65**, 259-275 (1997).

[2]M. E. Fermann, A. Galvanauskas and D. Harter, "All-fiber source of 100-nJ subpicosecond pulses," Applied Physics Letters **64**, 1315 (1994).

[3]A. Galvanauskas, M. E. Fermann, P. Blixt and D. Harter, "Microjoule ultrashort pulses from a hybrid diode laser-fiber amplifier system," in Conference on Lasers and Electro-Optics, Vol. 8, 1994 OSA Technical Digest Series (Optical Society of America, Washington, D.C.), 72-73, (1994).

[4]B. C. Collings, K. Bergman, S. T. Cundiff, S. Tsuda, J. N. Kutz, J. E. Cunningham, W. Y. Jan, M. Koch and W. H. Knox, "Short cavity erbium/ytterbium fiber lasers mode-locked with a saturable Bragg reflector," IEEE Journal of Selected Topics in Quantum Electronics **3**, 1065-1075 (1997).

[5]S. Gray and A. B. Grundinin, Optics Letters **21**, 967-969 (1996).

[6]M. E. Fermann, D. Harter, J. D. Minelly, and G. G. Vienne, Optics Letters **21**, 967 (1996).

[7]A. Galvanauskas, M. E. Fermann, D. Harter, J.D. Minelly, G. G. Vienne, and J. E. Caplen, "Broad-area diode-pumped 1 Watt femtosecond fiber system," in Conference on Lasers and Electro-Optics, Vol. 9, 1996 OSA Technical Digest Series (Optical Society of America, Washington, D.C.), 495-496, (1996).

[8]J. D. Minelly, A. Galvanauskas, M. E. Fermann, D. Harter, J. E. Caplen, Z. J. Chen and D. N. Payne, "Femtosecond pulse amplification in cladding-pumped fibers," Optics Letters **20**, 1797 (1995).

[9]D. Strickland and G. Mourou, "Compression of amplified chirped optical pulses," Optics Communications **56**, 219 (1985).

[10]A. Galvanauskas, M. E. Fermann, D. Harter, K. Sugden and I. Bennion, "All-fiber femtosecond pulse amplification circuit using chirped Bragg gratings," Applied Physics Letters **66**, 1053-1055 (1995).

[11]A. Galvanauskas, "Compact ultrahigh-power laser systems," Proc. SPIE **2377**, 117 (1995).

[12]K. Tamura, Y. Kimura and M. Nakazawa, "Femtosecond pulse generation over 82 nm wavelength span from passively modelocked erbium-doped fibre laser," Electronics Letters **31**, 1063 (1995).

[13]See chapter #1 for references to several applications requiring near-IR ultrashort pulses.

[14]G. Lenz, S. B. Fleischer, L. E. Nelson, D. J. Dougherty and E.P. Ippen, "91-pJ, 73-fs pulses from a frequency-doubled stretched-pulse additive-pulse mode-locked fiber laser," in Conference on Lasers and Electro-Optics, Vol. 9, 1996 OSA Technical Digest Series (Optical Society of America, Washington, D.C.), 30, (1996).

[15]V. Pruneri, S. D. Butterworth and D. C. Hanna, "Highly efficient green light generation by quasi-phase-matched frequency doubling of picosecond pulses from an amplified mode-locked Nd:YLF laser," Optics Letters **21**, 390 (1996).

[16]M. L. Dennis and I. N. Duling, "Experimental study of sideband generation in femtosecond fiber lasers," IEEE Journal of Quantum Electronics **QE-30**, 1469-1477 (1994).

[17]L. E. Myers, R. C. Eckardt, M. M. Fejer, R. L. Byer, W. R. Bosenberg, and J. W. Pierce, "Quasi-phasematched optical parametric oscillators in bulk periodically poled $LiNbO_3$," Journal of the Optical Society of America B **12**, 2102 (1995).

[18]O. E. Martinez, "3000 times grating compressor with positive group velocity dispersion: Application to fiber compensation in 1.3-1.6 μm region," IEEE Journal of Quantum Electronics **QE-23**, 59 (1987).

[19]A. Galvanauskas, M. E. Fermann, M. A. Arbore, J. D. Minelly, J. E. Caplen, M. M. Fejer and D. Harter, "High-energy high-average-power femtosecond fiber system using a QPM-grating pulse compressor," in Conference on Lasers and Electro-Optics, Vol. 6, 1998 OSA Technical Digest Series (Optical Society of America, Washington, D.C.), 364, (1998).

Chapter 4:Quasi-phasematched ultrashort-pulse optical parametric generation: theory and experiments

4.1 Introduction

Efficient, low power, compact sources of tunable ultrashort near- and mid-infrared pulses are necessary for many applications. Parametric frequency converters offer extremely wide tunability, (intrinsically limited only by material transparency), require only a single pump laser, and offer very high energy conversion efficiencies. An extensive review of current theoretical and experimental aspects of parametric frequency conversion appears in reference 1. A detailed treatment of the theory of gain, threshold, efficiency, tuning and spectral properties of parametric frequency conversion can be found in references 2 and 3.

The single-pass optical parametric generator (OPG) offers inherent simplicity and robustness when compared with other parametric conversion configurations, such as the synchronously-pumped optical parametric oscillator (OPO)[4,5] and the continuum-seeded optical parametric amplifier[6,7]. However, most ultrashort-pulse OPG systems reported to date have had threshold pump energies of several μJ[8] and higher, necessitating the use of complex pump lasers, outweighing the simplicity offered by the OPG configuration.

One current challenge for practical OPG systems is reducing the threshold to levels attainable directly from laser oscillators or simple oscillator-amplifier systems such as those described in chapter 3. In the present chapter, we describe two OPG systems with record low threshold energies. Both are based on quasi-phasematched parametric amplification in the nonlinear material PPLN and on erbium-fiber-based pump sources.

We begin with a theoretical analysis of the threshold for OPG. We show that the appropriate material figure of merit (FOM) for nearly-degenerate ultrashort-pulse OPG is the same as

that for ultrashort-pulse second harmonic generation (SHG), as defined in chapter 2. We then describe experiments which demonstrate OPG in both bulk and waveguide geometries.

4.2 Theory of ultrashort-pulse optical parametric generation (OPG)

Parametric optical interactions are those which are non-dissipative and, therefore, obey phasematching and Manley-Rowe constraints. For the second-order nonlinear media considered here, parametric interactions, in general, involve three fields. The highest frequency field is termed the "pump", while the lower frequency fields are termed "signal" and "idler". Conventionally, "signal" is used to describe either the intermediate frequency field, or the field of interest for the particular application. Usually, "idler" is used to describe the lowest frequency field. Second harmonic generation, as discussed in Chapters 2 and 3, is a special case of a degenerate (signal and idler frequencies are identical) parametric interaction. In the presence of strong pump fields, the signal and idler waves experience gain.

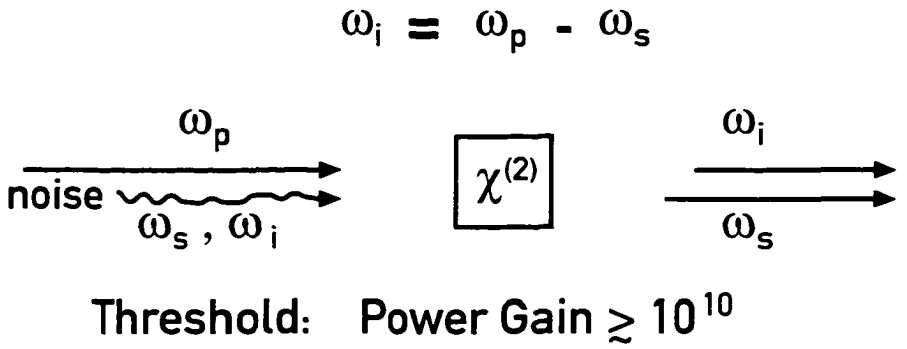

Figure 4.1: Schematic of the OPG process. A strong pump field (ω_p) incident on a nonlinear medium generates gain for signal (ω_s) and idler (ω_i) fields. The signal and idler frequencies are tunable, but constrained by conservation of energy (Manley-Rowe) and phasematching requirements. With adequate gain, vacuum noise can be amplified to macroscopic levels.

Optical parametric generation is the amplification of vacuum noise to macroscopic levels, typically to powers which are comparable to the pump power. The gain required to reach threshold (i.e. to reach macroscopic output levels) depends on the bandwidth of the parametric amplifier, as this bandwidth determines the total vacuum noise power present at the ampli-

fier input. For most parametric amplifiers, which typically have very wide parametric gain bandwidths, the threshold for OPG can be estimated from the pump power needed to produce ~100 dB of single-pass parametric gain. As we shall see shortly, the exact definition of threshold is not very important, as our final result will depend only logarithmically on this gain figure.

The single-pass power gain, G, for a phasematched parametric amplifier in the absence of pump depletion (an approximation which is valid at and below threshold) with input only at the signal frequency is given by[3]

$$G = \cosh(\Gamma L)^2, \tag{4.1}$$

where Γ is the parametric gain coupling coefficient and is similar to the SHG coupling coefficient defined in equation (2.31). As before, L is the length of the nonlinear material. For an amplifier operated near degeneracy, (the signal and idler frequencies are similar), Γ is given by

$$\Gamma^2 = \frac{8\pi^2 d_{eff}^2}{\lambda_1^2 n_1 n_2}|E_2|^2. \tag{4.2}$$

As before, d_{eff} is the effective nonlinear coefficient of the material, n_i is the refractive index and λ_i is the free-space wavelength at the signal ($i = 1$) or pump ($i = 2$) frequency. Here, we analyze the case of near-degenerate operation, rather than the more general off-degenerate case, for consistency of notation with the SHG analysis in chapter 2.

Equation (4.2) gives Γ^2 in terms of electric field. From Poynting's theorem, we have

$$I = \frac{1}{2} n_2 c \varepsilon_0 |E_2|^2, \tag{4.3}$$

where I is the pump intensity. Therefore,

$$\Gamma^2 = \frac{4\pi^2 d_{eff}^2}{c\varepsilon_0 \lambda_1^2 n_1 n_2^2} I. \tag{4.4}$$

In the limit of low gain, equation (4.1) approaches $G = 1 + \Gamma^2 L^2$. From this result and from equation (4.4), we see that parametric gain initially scales linearly with pump intensity

(or power) and quadratically with crystal length. For this reason, gain is often expressed in units of $\%/\mathrm{W cm}^2$. In the limit of high gain, equation (4.1) approaches

$$G = \frac{1}{4}\exp(2\Gamma L). \tag{4.5}$$

While OPG is strictly speaking an exponential rather than a threshold process, it is useful to define the OPG threshold as the condition for which $G \approx 10^{10}$. We find that

$$\Gamma_{thr} L \approx 12, \tag{4.6}$$

where Γ_{thr} is the value of Γ at threshold.

As with ultrashort-pulse SHG, the interaction length for ultrashort-pulse OPG is also limited by group velocity walkoff. Therefore, for nearly degenerate interactions, we require that

$$L = L_{walkoff} = \tau_2/\delta v = \tau_2 \Delta n_g / c, \tag{4.7}$$

where $\delta v \equiv [1/v_{g1} - 1/v_{g2}]$ is the group velocity mismatch parameter, τ_2 is the FWHM duration of the pump pulse and $v_{g,i}$ is the group velocity at the signal ($i = 1$) or pump ($i = 2$) frequency.

To achieve the lowest possible threshold in a bulk interaction, one typically focuses the pump beam tightly. We approximate the intensity for a confocally-focused beam by taking the effective area of a plane-wave beam to be $L\lambda/2n$. (In this case, we require the pump beam to be $\sqrt{2}$ larger in diameter than the size of a confocally focused Gaussian signal beam. Then, the generated signal will diffract only negligibly within the crystal.) We then have

$$I = \frac{P}{2L\lambda_2/n_2}, \tag{4.8}$$

where P is the pump power.

To solve for the OPG threshold power, P_{OPG}, we use equations (4.4) and (4.6) - (4.8), and we use the approximation $\lambda_1 \approx 2\lambda_2$ for near-degenerate operation. Thus,

$$P_{thr} = \left(\frac{72\varepsilon_0}{\pi^2}\right)\left(\frac{\lambda_2^3}{\tau_2}\right)\frac{1}{\mathrm{FOM}}, \tag{4.9}$$

where FOM is the same material figure of merit, $\mathrm{FOM} \equiv d_{eff}^2/(n_1 n_2 \Delta n_g)$, that we defined in chapter 2. Expressing the threshold condition in terms of the pump pulse energy $\mathcal{E}_{thr} \approx P_{thr}\tau_2$, we find

$$\mathcal{E}_{thr} = \left(\frac{72\varepsilon_0}{\pi^2}\right)\left(\frac{\lambda_2^3}{\mathrm{FOM}}\right). \tag{4.10}$$

We note that the near-degenerate OPG threshold, expressed in terms of pulse energy, does not depend on the pulse duration as long as the crystal length is chosen to be the maximum allowed by group velocity walkoff and the focusing is confocal. For 780-nm-pumped OPG in

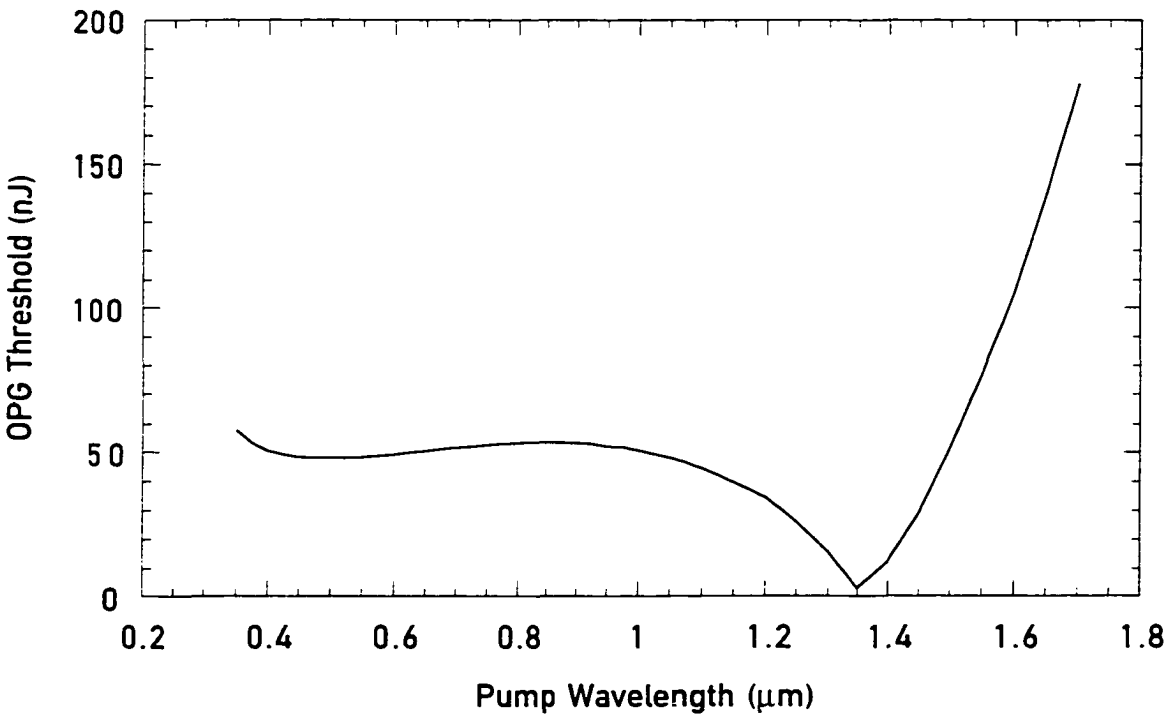

Figure 4.2: Nearly-degenerate OPG threshold for bulk PPLN devices with optimum length, as predicted by equation (4.10).

PPLN, equation (4.10) gives a threshold of 44 nJ. We will find in section 4.4 that with waveguide devices, substantially lower thresholds are possible.

Finally, we estimate the dependence of the near-degenerate OPG threshold with pump wavelength. The only factor in equation (4.10) which depends implicitly on wavelength is the GVM parameter, $\delta\nu$. In chapter 2 we found that for several materials, within much of the transparency window, $\delta\nu$ scales approximately as $\delta\nu \propto 1/\lambda^3$. Therefore, for wavelengths within this range, the threshold for near-degenerate OPG in bulk crystals is approximately independent of pump wavelength.

Figure 4.2 shows the numerically calculated near-degenerate OPG threshold for bulk PPLN as a function of pump wavelength, taking into account the exact material dispersion. We note that for pump wavelengths near 1.34 μm, the GVM parameter vanishes and therefore the OPG threshold is extremely low.

4.3 Bulk OPG experiment

The experimental setup is shown in figure 4.3. The pump source was a CPA erbium-fiber laser which was frequency doubled in bulk PPLN to generate 500 fs, 200 nJ and 777 nm pulses at a 200 kHz repetition rate. Lower repetition rates were used to generate higher pulse energies, but these were not necessary to reach the low threshold for OPG in PPLN. These 777 nm pulses were separated from the residual 1554 nm fundamental pulses by transmission through several cascaded absorptive glass filters and dichroic mirrors. Complete removal of residual 1554 nm light (i.e. attenuation by approximately 80 dB) was necessary to prevent unwanted seeding of the OPG process. However, near degeneracy (within ~ 50 nm), the device still operated as a parametric amplifier for the residual 1554 nm light.

Several PPLN crystals with lengths between 1 and 5 mm and QPM periods between 19 and 21 μm, including a multi-grating sample with 12 parallel grating sections, were investigated. The pump pulses were focused approximately confocally through the PPLN. We found that a 3 mm long device (1.6 pump-signal group velocity walkoff lengths) was optimum in terms of power conversion efficiency and threshold.

The dependence of the conversion efficiency on the pump energy in this 19-μm-period, 3-mm-long sample is shown in figure 4.4. The internal conversion efficiency (with Fresnel

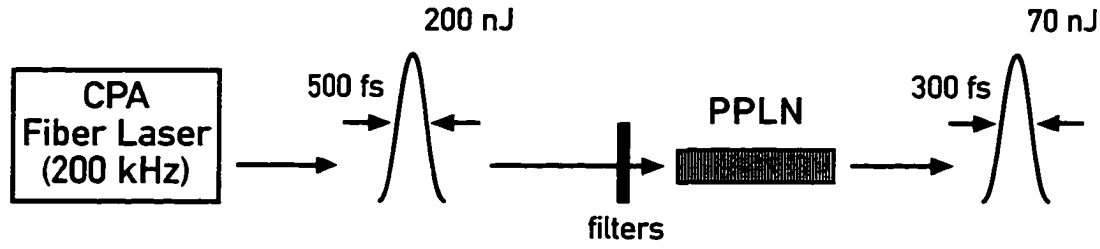

Figure 4.3: Experimental setup for demonstration of 54-nJ-threshold OPG in bulk PPLN.

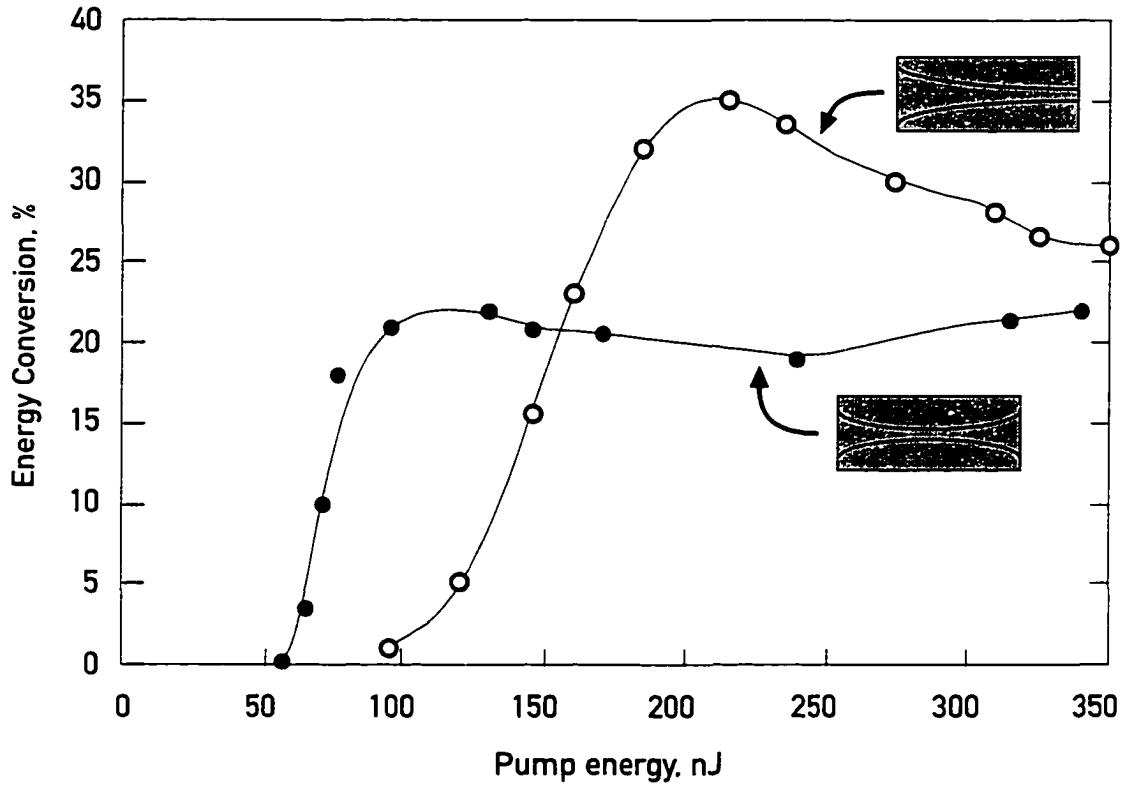

Figure 4.4: The dependence of the internal conversion efficiency on the pump energy in a 3-mm-long sample of PPLN. The curve with circles represents symmetric focusing, while the curve with open circles represents focusing with the pump beam waist on the output facet of the PPLN crystal.

energy losses at each of the uncoated facets of the PPLN crystal taken into account) is shown here. The signal wavelength for these measurements was 1.2 μm, and the signal pulses had FWHM durations of 300 fs. The efficiency was characterized for two focusing conditions.

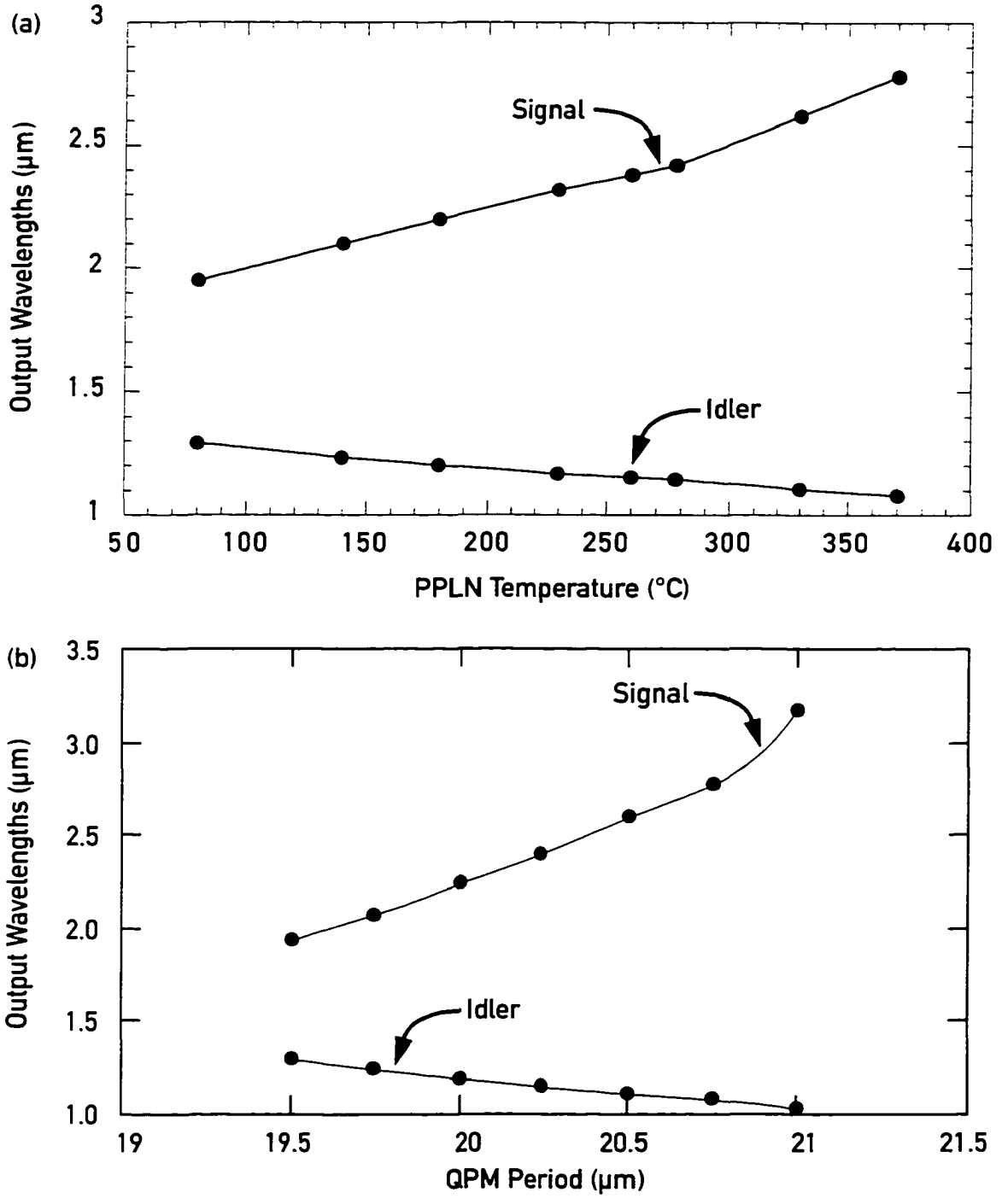

Figure 4.5: (a) Output signal and idler wavelengths plotted against the temperature of an 19.0-μm-period PPLN OPG device pumped at 777 nm. (b) Output signal and idler wavelengths for the multi-grating OPG device. In (b), tuning was accomplished by translating the PPLN chip so that the pump beam passed through different QPM grating periods. This device was pumped at 777 nm.

We were able to observe either the lowest threshold (dots) or the highest saturated conversion efficiency (circles). With symmetric focusing (minimum pump beam waist in the center of the crystal), we observed an OPG threshold of 54 nJ and a saturated conversion efficiency of 23% with 100 nJ of pump light inside the PPLN crystal. This threshold is in close agreement with equation (4.10). With the minimum waist located at the back facet of the PPLN crystal, the OPG threshold was 100 nJ and the maximum total (signal plus idler) energy conversion efficiency was 38%, with 220 nJ of pump inside the PPLN crystal.

Tuning of the OPG device was accomplished in two ways. First, we adjusted the PPLN temperature from 60 degrees to 375 degrees Celsius, resulting in tuning from 1 to 3 μm for the signal and the idler. Temperature tuning is shown in figure 4.5(a). Then we used the multiple-grating PPLN sample with QPM periods between 19.5 and 21 μm to observe a comparable tuning range. The latter tuning results are shown in figure 4.5(b).

The bulk PPLN OPG devices described in this section worked well over a wide range of operating conditions, including output wavelength, temperature, pulse energy and pulse repetition rate.

4.4 Waveguide OPG theory

For practical OPG systems, it is desirable to further reduce the threshold to levels attainable directly from laser oscillators. To this end, waveguide geometries can increase conversion efficiencies (or the parametric gain) of nonlinear devices by tightly confining the optical fields over long interaction lengths. The trade-off between focusing tightly for high intensities and focusing loosely for avoiding diffraction is thereby eliminated. Thus, the scaling rules governing OPG in waveguide geometries differ from those discussed in section 4.2.

Rather than calculate the threshold pulse energy from the threshold intensity, as we did for bulk interactions, we take an alternate approach here. The relationship between parametric gain and pump intensity for waveguide devices is somewhat complicated by modal overlaps and by the degraded nonlinear properties which sometimes accompany waveguide fabrication techniques. This relationship is covered in detail by Bortz[9-11]. Instead, we will use a single lumped parameter to describe waveguide designs.

Here we use the normalized (with respect to power and waveguide length) parameter η_0, which describes SHG conversion efficiency and near degenerate parametric gain; η_0 is often expressed in units of %/Wcm^2 in the guided-wave nonlinear optics literature. We note that the normalized (with respect to fundamental power) SHG efficiency for single-frequency inputs is the same as the near-degenerate normalized (with respect to pump power) parametric gain in the low-gain limit.

We use the following relation for low parametric gains

$$G = \eta_0 P L^2 \equiv \Gamma^2 L^2, \tag{4.11}$$

while for high gain

$$G = \frac{1}{4}\exp(2\sqrt{\eta_0 P L^2}). \tag{4.12}$$

The normalized gain parameter, η_0, is related to details of the waveguide design by[9]

$$\eta_0 = \frac{8\pi^2}{c\varepsilon_0\lambda_1\lambda_2 n_1 n_2^2}\left|\int_{-\infty}^{\infty}\int d(x, y)\bar{E}_1^2(x, y)\bar{E}_2^*(x, y)dxdy\right|^2, \tag{4.13}$$

where $\bar{E}_1(x, y)$ and $\bar{E}_2(x, y)$ are the normalized spatial distributions of the modal field for the signal and pump frequencies, respectively. Again, we have assumed near-degenerate interactions.) Here we allow the nonlinear coefficient of the waveguide material, $d(x, y)$, to vary with transverse position. Here, $d(x, y)$ is an effective nonlinear coefficient which accounts for the reductions due to QPM, if appropriate. In equation (4.13), the fields are normalized according to

$$\int_{-\infty}^{\infty}\int \bar{E}_i^2(x, y)dxdy = 1. \tag{4.14}$$

where $i = 1, 2$.We note that the squared magnitude of the overlap integral in equation (4.13) has units of inverse area.

To solve for the OPG threshold condition in terms of the pump pulse energy $\mathcal{E}_{thr} \approx P\tau_2$, we use equations (4.6), (4.7) and (4.11). Then,

$$\mathcal{E}_{thr} \approx 150\frac{(\delta\nu)^2}{\eta_0\tau_2}. \tag{4.15}$$

Thus, we see that for waveguide devices, the threshold energy decreases as the duration of the pump pulse increases. This contrasts with optimally-focused bulk devices, where the threshold energy is independent of the duration of the pump pulse.

We also note that the group velocity mismatch (GVM) parameter appears as the square in equation (4.15), while for bulk OPG, GVM only appears linearly in the material FOM. Therefore, we can conclude that materials which have a good balance between nonlinearity and GVM for bulk interactions (as quantified by the FOM) may not necessarily be such good materials for guided-wave interactions. In the case of PPLN, the availability of mature waveguide technologies such as APE is a far more compelling advantage than the relatively large GVM at technologically important wavelengths is a disadvantage.

It is interesting to compare the threshold predicted by equation (4.15) for waveguide OPG with that predicted by equation (4.10) for bulk OPG. The normalized gain parameter, η_0, for an optimized annealed proton exchanged (APE)-PPLN device operating near $\lambda_1 \approx 1560$ nm is approximately 100 %/Wcm^2. [12] Therefore, the reduction in threshold for 780-nm-pumped OPG that can be expected with APE-PPLN devices, relative to bulk-PPLN devices, is $40 \cdot (\tau_2/1\,\mathrm{ps})$. For example, for OPG with $\tau_2 = 15$ ps (i.e. $L = 5$ cm, which is a practical length given current APE-PPLN fabrication technology), equation (4.15) predicts a threshold of $\mathcal{E}_{thr} \approx 90$ pJ, which is well within the range available directly from ultrashort-pulse fiber oscillators. In the next section we demonstrate that the expected threshold reduction does indeed occur.

Finally, we estimate the dependence of waveguide-OPG threshold with pump and/or output wavelength. The two factors in equation (4.15) which depend on wavelength are the GVM parameter, $\delta\nu$, and the normalized gain parameter, η_0.

For several materials, within much of the transparency window, $\delta\nu$ scales approximately as $\delta\nu \propto 1/\lambda^3$. For near-degenerate waveguide designs, equation (4.13) predicts that η_0 scales approximately as $\eta_0 \propto 1/\lambda^4$, where we have assumed that the waveguide area scales

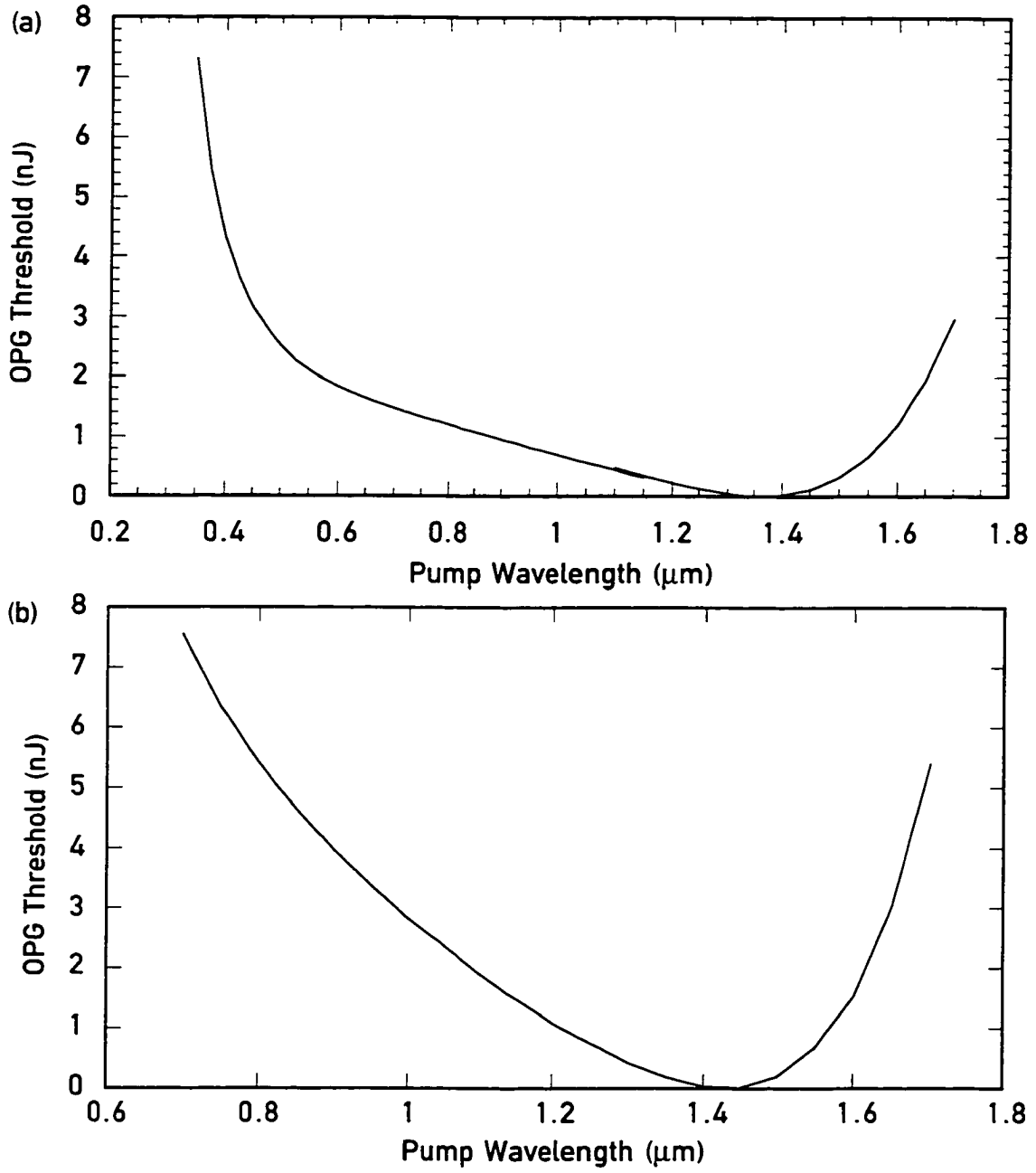

Figure 4.6: (a) Nearly-degenerate OPG threshold for APE-PPLN waveguide devices with optimum length for pump pulses with 1 ps duration. The dispersion of bulk PPLN was used to approximate the waveguide modal index dispersion. The simple $\eta_0 \propto 1/\lambda^4$ scaling rule for waveguide gain was also used. (b) Off-degenerate OPG threshold for λ_{idler} = 3.2 μm and assuming APE-PPLN waveguide devices with optimum length for pump pulses with 1 ps duration. The dispersion of bulk PPLN was used to approximate the waveguide modal index dispersion. The simple $\eta_0 \propto 1/\lambda_{pump}$ scaling rule for waveguide gain was also used.

approximately as area $\propto 1/\lambda^2$. Therefore, the OPG threshold for near-degenerate operation in waveguides scales approximately as $\mathcal{E}_{thr} \propto 1/\lambda^2$. Figure 4.6(a) shows the numerically calculated near-degenerate OPG threshold for APE-PPLN as a function of pump wavelength. (The scaling $\mathcal{E}_{thr} \propto 1/\lambda^2$ applies reasonably well for pump wavelengths in the range of 0.4 - 1.2 μm.)

For some applications where laser-OPG systems are of interest, there exists a specific idler wavelength which must be generated, but there are several available choices for the pump wavelength. In this case, the waveguide area is fixed by the idler wavelength and η_0 scales approximately as $\eta_0 \propto 1/\lambda_{pump}$. However, in this case the crystal length allowed by GVM does not approximate a simple scaling rule, and it depends both on the pump-signal GVM as well as the signal-idler GVM. Signal-idler GVM can be neglected, however, in low dispersion spectral regions within the transparency range of the nonlinear material. Figure 4.6(b) shows an example of the pump wavelength scaling of the OPG threshold in APE-PPLN waveguides with the idler wavelength in such a spectral region

4.5 Waveguide OPG background

High parametric gain (and therefore low threshold) is not the only advantage of waveguide geometries for parametric interactions. Waveguide geometries can also eliminate several problematic spatial effects such as gain-induced diffraction, spatially-nonuniform pump depletion and spatially-nonuniform back-conversion. In particular, waveguide OPG is expected to produce excellent beam quality, as compared to the poor beams often observed for bulk OPG.

Of several available material systems, annealed proton exchanged (APE) waveguides in PPLN offer high nonlinearities, tight confinement, moderate losses and a mature fabrication technology. Several guided-wave interactions, including highly efficient SHG[13], parametric fluorescence[14] and parametric oscillation[12,15], have been demonstrated in APE-PPLN. However, parametric superflorescence (OPG) has not, before this thesis work, been observed in waveguides in any material system.

One inherent difficulty with implementing parametric interactions in waveguides stems from the large disparity between input and output wavelengths. A waveguide that supports modes at the longest wavelength is of necessity multimoded at the shortest wavelength. It is

difficult to robustly couple the short-wavelength pump radiation into the fundamental mode of such a multimoded structure. (This problem is avoided in guided-wave SHG devices, which are typically single-moded at the input wavelength.) Only the fraction of the pump power present in the phasematched mode can contribute to the frequency conversion process.

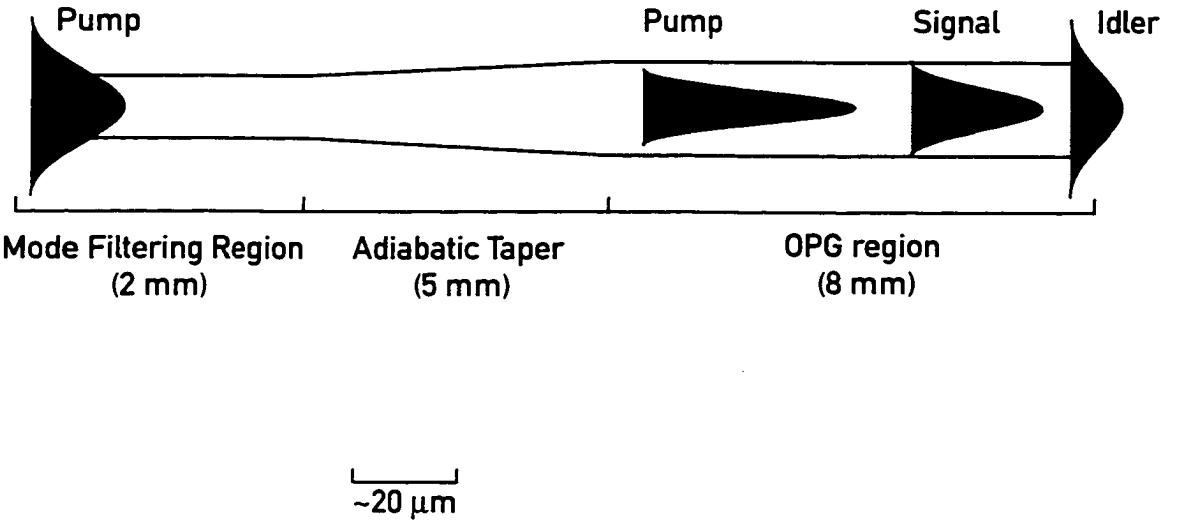

Figure 4.7: Integrated structure for robust coupling of pump light into a parametric frequency conversion waveguide device. The mode filtering region allows robust coupling of pump light into a single mode, while the adiabatic taper transforms this mode into the fundamental mode of the highly-multimoded OPG region. Ideally, all of the parametric gain is experienced in the uniform OPG region, which has a length of approximately $L_{walkoff}$.

For applications with only short-wavelength inputs (such as off-degenerate DFG or quantum-noise-seeded OPG), this mode-coupling problem can be solved with the tapered waveguide structure shown in figure 4.7. This integrated structure, implemented with periodically segmented waveguides, is described in detail by Chou, et. al[16]. Briefly, the pump (and, if present, the off-degenerate signal) light is coupled into a single-mode waveguide that acts as a mode filter. This pump mode is then adiabatically transformed into the fundamental mode of the highly-multimoded (at the pump wavelength) waveguide in which the parametric interaction takes place. For OPG devices, no special attention is required to couple signal light into the waveguide because an OPG device is seeded with quantum (vacuum) noise, which is always present.

4.6 Waveguide OPG experiment

For the OPG experiments described here, we chose annealed proton exchanged (APE) waveguides in PPLN as the material system. The channel waveguide device was designed using the model given by Bortz[9-11] to have a normalized parametric gain of 60 %/W-cm^2 and a single transverse mode for the output wavelengths near 1560 nm. The mode filter, adiabatic taper and OPG regions were 2 mm, 5 mm, and 8 mm long, respectively. The substrate had a QPM period of 14.5 μm and the waveguides were proton exchanged at 177 °C for 3.9 hours through 5.5-μm-wide SiO_2 mask openings and were annealed in flowing O_2 at 325 °C for 12 hours. SHG tuning curves for similar nearby waveguides without tapers exhibited near-sinc^2 shapes, indicating homogeneous processing and normalized conversion efficiencies, η_0, of 55 %/W-cm^2. Mode imaging of the waveguide output facet confirmed single-mode excitation of the pump light both below and above OPG threshold.

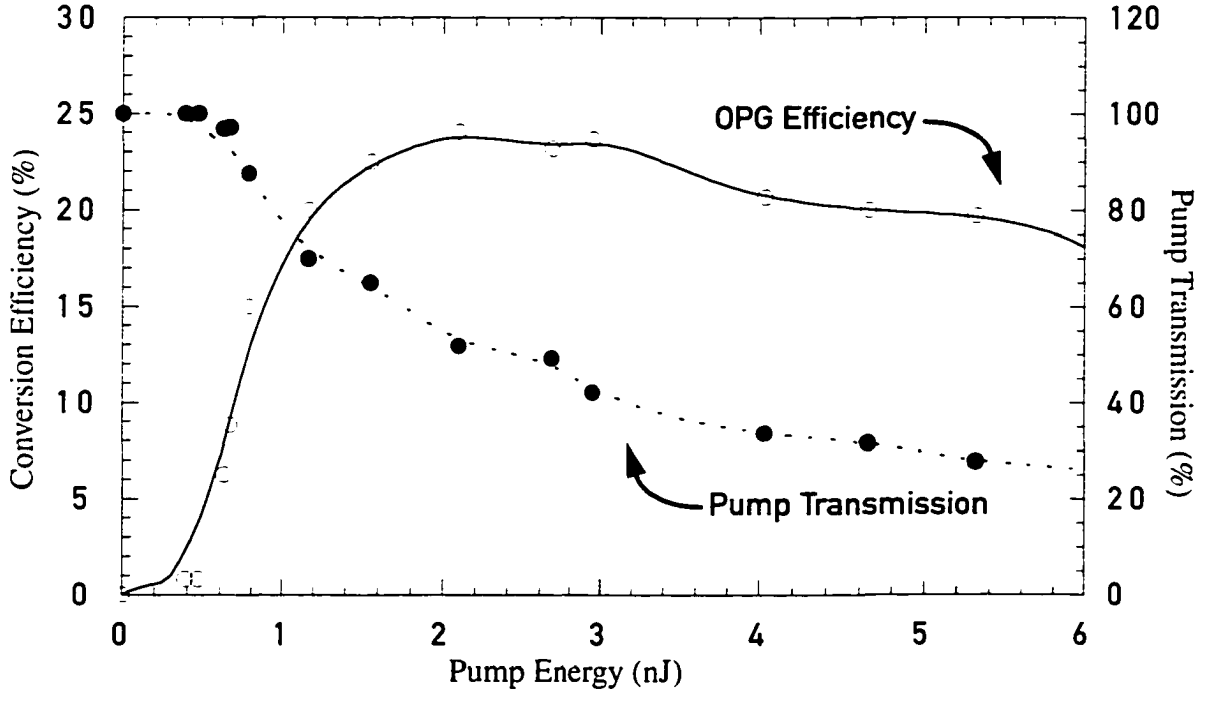

Figure 4.8: Energy conversion efficiency from pump to signal plus idler and pump transmission for waveguide-OPG plotted against input pump energy. Threshold was observed for 380 pJ of pump energy exiting the waveguide, after correcting for Fresnel losses.

We pumped our waveguide OPG device with 2 ps, 775-780 nm pulses from a frequency-doubled, tunable amplified erbium doped fiber laser. The waveguide was held at 100 degrees Celsius to avoid photorefractive damage. Equation (4.15) predicts a threshold near 1 nJ under these conditions. Near degeneracy, measurable output was observed for pump energies of 380 pJ exiting the waveguide, while significant depletion of the pump was observed at 1 nJ, as shown in figure 4.8. The observed threshold is consistent with the threshold calculation in equation (4.15), given that the OPG region is longer than one pump-signal group velocity walkoff length (6 mm).

At high pump energies (>1 nJ), spurious high-order quasi-phasematched interactions such as SHG and sum frequency mixing began generating visible and UV light at the expense of the signal and idler outputs. We were unable to quantitatively estimate the visible/UV power generated because much of it was scattered out of the waveguides.

The tuning behavior of the waveguide-OPG device is shown in figure 4.9.

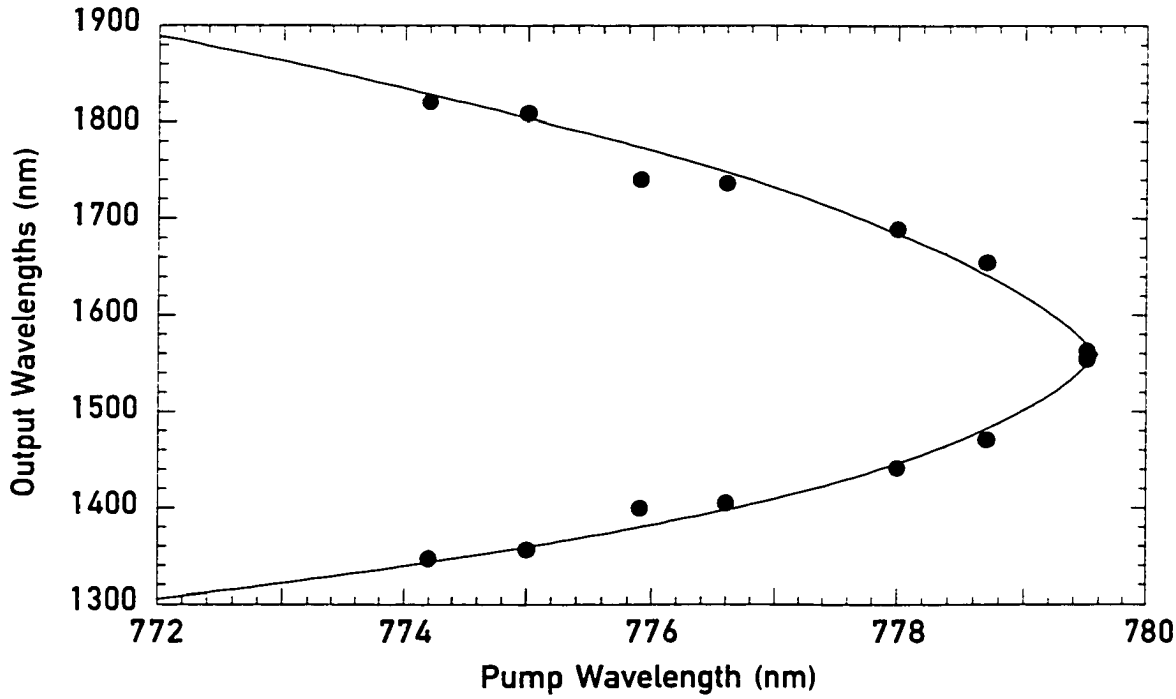

Figure 4.9: Tuning of waveguide-OPG device (100 °C). The output wavelengths ranged from 1350-1800 nm for pump wavelengths of 774-779 nm. The solid line is a prediction based on theoretical waveguide dispersion, with degeneracy set to the measured wavelength.

The solid line is a prediction based on the theoretical waveguide dispersion[10], with the degeneracy wavelength set to the measured value. The bandwidths of the signal and idler pulses were typically ~20 nm. The durations of the output pulses were not measured, but they are expected to be ~2.5 ps because of small amounts of pump-signal and pump-idler group velocity walkoff in the 8 mm OPG region.

4.7 Summary of Chapter

In summary, in this chapter we analyzed theoretically the threshold of optical parametric generators in both bulk and waveguide geometries. For bulk devices, the threshold is related to the ultrashort-pulse SHG material figure of merit (FOM) described in chapter 2 and is independent of pulse duration. For waveguide devices, the threshold decreases linearly as the pump pulse duration is increased.

Experimentally, we demonstrated single-pass optical parametric generation (OPG) with record low thresholds in both bulk PPLN and waveguide APE-PPLN configurations. The bulk device exhibited a 54 nJ threshold, a 38% energy conversion efficiency, a 1-3 μm tuning range and output pulse energies up to 200 nJ. The waveguide device exhibited a 380 pJ threshold, a 25 % energy conversion efficiency and a 1350-1800 nm tuning range. The latter result is, to our knowledge, the first demonstration of OPG in a waveguide geometry. The thresholds of these bulk and waveguide devices are approximately 2 and 4 orders of magnitude, respectively, below that which had previously been demonstrated in any OPG system.

Future work on guided-wave parametric interactions may explore the quasi-continuous-wave regime of high-gain OPA or OPG. Also, engineering of the waveguide dispersion may enable shifting of the wavelength for which GVM vanishes to values significantly other than that of the bulk material. This zero-GVM wavelength is of interest because it enables extremely low threshold waveguide-OPG devices.

References

[1]See the special issue on parametric devices, Journal of the Optical Society of America B **12** (1995).

[2]R. L. Byer, "Parametric Oscillators and Nonlinear Materials," in *Nonlinear Optics*, edited by P. G. Harper and B. S. Wherrett (Academic Press, London, 1975).

[3]R. L. Byer, "Optical Parametric Oscillators," in *Quantum Electronics: A Tretise*, edited by H. Rabin and C. L. Tang (Academic Press, New York, 1975), Vol. I.

[4]K. C. Burr, C. L. Tang, M. A. Arbore and M. M. Fejer, "Broadly tunable mid-infrared femtosecond optical parametric oscillator using all-solid-state-pumped periodically poled lithium niobate," Optics Letters **22**, 1458 (1997).

[5]P. E. Powers, R. J. Ellingson, W. S. Pelouch, and C. L. Tang, "Recent advances of the Ti:sapphire-pumped high-repetition-rate femtosecond optical parametric oscillator," Journal of the Optical Society of America B **10**, 2162 (1993).

[6]M. K. Reed, M. K. Steiner-Shepherd, M. S. Armas, and D. K. Negus, "Microjoule-energy ultrafast optical parametric amplifiers," Journal of the Optical Society of America B **12**, 2229 (1995).

[7]T. Wilhelm, J. Piel and E. Ridle "Sub-20-fs pulses tunable across the visible from a blue-pumped single-pass noncollinear parametric converter," Optics Letters **22**, 1494-1496 (1997).

[8]R. Danielius, A. Piskarskas, A. Stabinis, G. P. Banfi, P. Di. Trapani, and R. Righini, "Traveling-wave parametric generation of widely tunable, highly coherent femtosecond light pulses," Journal of the Optical Society of America B **10**, 2222 (1993).

[9]M. L. Bortz, "Quasi-Phasematched Optical Frequency Conversion in Lithium Niobate Waveguides," Ph.D. Dissertation, Stanford University, 1994.

[10]M. L. Bortz and M. M. Fejer, "Annealed proton-exchanged $LiNbO_3$ waveguides," Optics Letters **16**, 1844 (1991).

[11]M. L. Bortz, L. A. Eyres and M. M. Fejer "Depth profiling of the d_{33} nonlinear coefficient in annealed proton exchanged LiNbO3 waveguides," Applied Physics Letters **62**, 2012

(1993).

[12]M. A. Arbore and M. M. Fejer, "Singly resonant optical parametric oscillation in lithium niobate waveguides," Optics Letters **22**, 151 (1997).

[13]K. Kintaka, M. Fujimura, T. Suhara, and H. Nishihara, "High-efficiency $LiNbO_3$ waveguide second harmonic generation devices with ferroelectric-domain-inverted gratings fabricated by applying voltage," Journal of Lightwave Technology **14**, 462-468 (1996).

[14]P. Baldi, P. Aschieri, S. Nouh, M. De Micheli, D. Ostrowsky, D. Delacourt and M. Papuchon, "Modeling and experimental observation of parametric fluorescence in periodically poled lithium niobate waveguides," IEEE Journal of Quantum Electronics **QE-31**, 997-1008 (1995).

[15]M. L. Bortz, M. A. Arbore and M. M. Fejer, "Quasi-phasematched optical parametric amplification and oscillation in periodically poled $LiNbO_3$ waveguides," Optics Letters **20**, 49-51 (1995).

[16]M. H. Chou, M. A. Arbore and M. M. Fejer, "Adiabatically tapered periodic segmentation of channel waveguides for mode-size transformation and fundamental mode excitation," Optics Letters **21**, 794 (1996).

Chapter 5:Conclusion

5.1 Summary of dissertation

This dissertation discussed frequency conversion of ultrashort pulses, including second harmonic generation (SHG) and tunable optical parametric generation (OPG). We proposed, analyzed and demonstrated an entirely new nonlinear optical process. This interaction, which relies on aperiodic quasi-phasematching (QPM) structures, is capable of simultaneous frequency conversion and compression of optical pulses. We also demonstrated that PPLN makes possible practical coherent sources which are pumped by low-power diode-pumped fiber-lasers.

5.2 Summary of results

In chapter 2, we showed that when GVD at the fundamental frequency can be neglected, a simple transfer function relationship describes the SHG process for arbitrary input pulses. This SHG transfer function depends only on material properties and the design of the QPM grating.

The SHG transfer function relationship was applied to two important cases. First, we examined quantitatively the trade-off between efficiency and pulse distortion when choosing the crystal length for ultrashort-pulse SHG. Second, we showed that chirped QPM gratings can be designed to generate transform-limited SH output pulses from arbitrarily chirped fundamental input pulses.

In chapter 3, we described experiments which demonstrate that QPM ultrashort-pulse SHG is both efficient and versatile. Diode-pumped erbium-doped fiber lasers (EDFLs) generating femtosecond pulses with a 1560 nm wavelength were combined with PPLN and CPPLN frequency doublers to demonstrate simple and practical laser systems. In particular,

we demonstrated generation of 8.1 mW of 190 fs, 777 nm pulses at an 88 MHz repetition rate at an energy conversion efficiency of 25% using direct frequency doubling of a passively mode-locked fiber oscillator.

We also showed that chirped QPM gratings can be used for simultaneous second harmonic generation and ultrashort pulse compression. We efficiently generated 110 fs (FWHM) near-transform-limited 780 nm pulses with 150-fold compression relative to the input pulses.

Finally, we showed that the combination of an erbium-doped fiber oscillator, a single-mode fiber pulse-stretcher, an erbium-doped fiber amplifier and a chirped-PPLN pulse compressor can comprise a simple and robust source of moderate-energy (several nJ) ultrashort (~250 fs) pulses.

In chapter 4, we demonstrated single-pass OPG with record low thresholds in both bulk PPLN and waveguide APE-PPLN configurations. The bulk device exhibited a 54 nJ threshold, a 38% energy conversion efficiency, a 1-3 μm tuning range and output pulse energies up to 200 nJ. The waveguide device exhibited a 380 pJ threshold, a 25 % energy conversion efficiency and a 1350-1800 nm tuning range. The latter result is, to our knowledge, the first demonstration of OPG in a waveguide geometry. The thresholds of these bulk and waveguide devices are approximately 2 and 4 orders of magnitude, respectively, below that which had previously been demonstrated in any OPG system[1].

5.3 Future directions

Future work on aperiodic-grating QPM-SHG may address the limits of conversion efficiency and SH pulse duration. The transfer function derived in chapter 2 is strictly valid only in the limit of no pump depletion (zero efficiency) and no GVD at the fundamental frequency.

High conversion efficiency is obviously desirable for most applications. While preliminary experiments demonstrated up to 40% efficient SHG of high quality compressed pulses, it is unclear how much further this efficiency can be pushed. Both theoretical and experimental studies are needed to determine the trade-off between efficiency and pulse quality under these

conditions. It is possible that this trade-off can be favorably affected by more subtle aperiodic-grating designs.

Several commercially available[2-6] laser systems can generate pulses with durations less than 100 fs, while laboratory systems[7-9] have been reported with pulse durations significantly below 10 fs. It is clear that GVD at the fundamental frequency will be important in designing aperiodic-QPM gratings for these lasers. A better theoretical understanding of the effects of fundamental GVD, which are non-transfer-function in nature, will be needed.

Future work on QPM-OPG devices may address the spectral properties of the OPG output. Because the gain bandwidth of a parametric amplifier is typically much larger than that required to support the ultrashort pulses which are generated, and because OPG devices are seeded by wide-bandwidth vacuum noise, OPG output pulses are typically 5-20 times transform limited. It is possible that the combination of chirped pump pulses and chirped QPM gratings can be used to limit the gain bandwidth of the OPG device. It is also possible that one can integrate a two-stage OPG seed-amplifier[1,10] system onto a single nonlinear crystal using the lithographic nature of QPM device fabrication, much like has been done recently for cascading multiple frequency conversion steps into single PPLN crystals[11].

References

[1]R. Danielius, A. Piskarskas, A. Stabinis, G. P. Banfi, P. Di. Trapani, and R. Righini, "Traveling-wave parametric generation of widely tunable, highly coherent femtosecond light pulses," Journal of the Optical Society of America B **10**, 2222 (1993).

[2]MIRA and Vitesse spec sheets, (Coherent, Inc., Santa Clara, CA).

[3]Tsunami spec sheet, (Spectra Physics, Mountain View, CA).

[4]FPL-01 femtosecond Er:fiber laser spec sheet, (Calmar Optcom, Mountain View, CA).

[5]Femtolite 1550 femtosecond fiber laser spec sheet, (IMRA America, Ann Arbor, MI).

[6]SErF femtosecond fiber laser spec sheet, (Clark-MXR, Dexter, MI).

[7]M. Nisoli, S. Stagira, S. De Silvestri, O. Svelto, S. Sartania, Z. Cheng, M. Lenzner, C. Spielmann and F. Krausz, "A novel nigh-energy pulse compression system: generation of multigigawatt sub-5-fs pulses," Applied Physics B (Lasers and Optics) **B65**, 189-196 (1997).

[8]S. Sartania, Z. Cheng, M. Lenzner, G. Tempea, C. Spielmann, F. Krausz and K. Ferencz, "Generation of 0.1-TW 5-fs optical pulses at a 1-kHz repetition rate," Optics Letters **22**, 1562-1564 (1997).

[9]I. D. Jung, F. X. Kartner, N. Matuschek, D. H. Sutter, F. Morier-Genoud, G. Zhang, U. Keller, V. Scheuer, and M. Tilsch and T. Tschudi, "Self-starting 6.5-fs pulses from a Ti:sapphire laser," Optics Letters **22**, 1009-1011 (1997).

[10]V. Petrov, F. Seifert and F. Noack "High repetition rate traveling wave optical parametric generator producing nearly bandwidth limited 50 fs infrared light pulses," Applied Physics Letters **65**, 268-270 (1994).

[11]W. R. Bosenberg, J. I. Alexander, L. E. Myers and R. W. Wallace, "2.5-W, continuous-wave, 629-nm solid-state laser source," Optics Letters **23**, 207-209 (1998).

Appendix A: Alternate derivation of the second harmonic generation (SHG) transfer function: Time domain approach

A.1 Introduction

In chapter 2, we derived the SHG transfer function using a frequency domain analysis which describes naturally the concepts of nonlinear optics. In this appendix, we derive the same result using a time domain analysis analogous to treatments of the nonlinear Schrodinger equation common in the ultrafast literature. Though the frequency domain analysis is simpler to generalize for arbitrary material dispersion (especially inclusion of GVD at the fundamental frequency), this time domain analysis may be more intuitive for some readers. It is the method that was used in reference 1, the first analysis of this process.

A.2 Slowly varying envelope approximation

We begin with the one-dimensional scalar wave equation

$$\frac{\partial^2 E}{\partial z^2} = \mu_0 \varepsilon_0 \varepsilon \frac{\partial^2 E}{\partial t^2} + \mu_0 \frac{\partial^2 P_{NL}}{\partial t^2}, \tag{A.1}$$

and consider the case of second harmonic generation of ultrashort pulses. Though ultrashort pulses intrinsically have significant bandwidths, we restrict this analysis to pulses with bandwidths that are small compared to their optical carrier frequency. This simplification allows us to derive a distinct pair of slowly varying envelope equations for the fundamental and second harmonic waves. We begin by assuming that the electric field can be written in the form

$$E = E_1(z,t) + E_2(z,t), \tag{A.2}$$

where

$$E_i(z,t) = \frac{1}{2}C_i(z,t)\exp[i(\omega_i t - k_i z)] + \text{c. c.}, \tag{A.3}$$

$i = 1, 2$ indicates the fundamental (1) or second harmonic (2) frequency, ω_i is the carrier frequency and $\omega_2 = 2\omega_1$. The functions $C_i(z,t)$, which contain both amplitude and phase information, describe the temporal and spatial evolution of the field envelopes. The k-vector in the medium is given by $k^2 = [\omega^2\varepsilon(\omega)]/c^2$, which we will approximate with series expansions around the two carrier frequencies. To second order,

$$k(\omega-\omega_i) = k_i + \left.\frac{\partial k}{\partial\omega}\right|_{\omega_i}(\omega-\omega_i) + \left.\frac{1}{2}\frac{\partial^2 k}{\partial\omega^2}\right|_{\omega_i}(\omega-\omega_i)^2. \tag{A.4}$$

We note that $k_i^2 = (\omega_i^2\varepsilon(\omega_i))/c^2$, that the group velocity at each frequency is defined as

$$v_{g,i} = \left(\left.\frac{\partial k}{\partial\omega}\right|_{\omega_i}\right)^{-1} \tag{A.5}$$

and that the intra-pulse group velocity dispersion (GVD) at each frequency is defined as

$$\beta_i = \left.\frac{\partial^2 k}{\partial\omega^2}\right|_{\omega_i}. \tag{A.6}$$

Substituting equations (A.2)-(A.6) into (A.1) and assuming that the envelopes vary slowly compared to the carrier frequencies, we obtain the usual slowly varying envelope equations

$$\frac{\partial}{\partial z}C(z,t) + v_{g,i}^{-1}\frac{\partial}{\partial t}C_i(z,t) - \frac{i}{2}\beta_i\frac{\partial^2}{\partial t^2}C_i(z,t) = -i\left(\frac{\mu_0 c\omega_i}{2n_i}\right)P_{NL}. \tag{A.7}$$

We need only consider the nonlinear polarization that is quadratic in electric field. We also assume that the nonlinear coefficient is non-dispersive in frequency. We write the nonlinear coefficient as $d(z)d_{eff}$, where d_{eff} is the maximum effective nonlinearity and $d(z)$ is the normalized, position-dependent nonlinear coefficient. With these definitions, we may write the nonlinear polarization in the form

$$P_{NL} = 2d(z)d_{eff}\varepsilon_0 E^2 = 2d(z)d_{eff}\varepsilon_0[E_1(z,t) + E_2(z,t)]^2. \quad \text{(A.8)}$$

In equation (A.8), we note that E_i are complex valued electric fields, as defined by equation (A.3). In subsequent analysis, we drop mixing terms other than those responsible for SHG.

We consider separately the polarization components with carrier frequencies ω_1 and ω_2, yielding two equations. We use the relation $\omega_i = (2\pi c)/\lambda_i$, where λ_i are the free-space wavelengths. We can now write the slowly varying envelope equations in the form

$$\frac{\partial}{\partial z}C_1(z,t) + v_{g1}^{-1}\frac{\partial}{\partial t}C_1(z,t) - \frac{i\beta_1}{2}\frac{\partial^2}{\partial t^2}C_1(z,t) = \frac{n_1}{n_2}\Gamma d(z)C_1^*(z,t)C_2(z,t)\exp(i\Delta k_0 z) \quad \text{(A.9)}$$

and

$$\frac{\partial}{\partial z}C_2(z,t) + v_{g2}^{-1}\frac{\partial}{\partial t}C_2(z,t) - \frac{i\beta_2}{2}\frac{\partial^2}{\partial t^2}C_2(z,t) = \Gamma d(z)C_1^2(z,t)\exp(-i\Delta k_0 z), \quad \text{(A.10)}$$

where we have defined $\Gamma \equiv -i2\pi d_{eff}/(\lambda_1 n_2)$ and $\Delta k_0 \equiv 2k_{1,0} - k_{2,0}$.

A.3 The depletion-free and dispersion-free pump limit

Two simplifications to equation (A.9) allow us to derive a useful solution. We first assume that the overall conversion efficiency is low, and therefore, that there is no depletion of the fundamental (pump). In equation (A.9) the nonlinear polarization at the fundamental frequency, which drives pump depletion, is set to zero. We also require that GVD does not sig-

nificantly distort the fundamental pulse by setting $\beta_1 = 0$. This physical condition is automatically satisfied for quasi-monochromatic (continuous-wave, or CW) inputs. For pulsed inputs, this condition limits the bandwidth of the input pulse as well as the length of the nonlinear material. We now have

$$\frac{\partial}{\partial z}C_1(z,t) + v_{g1}^{-1}\frac{\partial}{\partial t}C_1(z,t) = 0 \text{ and} \tag{A.11}$$

$$\frac{\partial}{\partial z}C_2(z,t) + v_{g2}^{-1}\frac{\partial}{\partial t}C_2(z,t) - \frac{i\beta_2}{2}\frac{\partial^2}{\partial t^2}C_2(z,t) = \Gamma d(z)C_1^2(z,t)\exp(-i\Delta k_0 z). \tag{A.12}$$

In equation (A.12) we retain GVD at the second harmonic frequency for two reasons. First, many interactions in most materials exhibit greater GVD at the second harmonic frequency than at the fundamental frequency. Second, retaining GVD for the second harmonic does not appreciably complicate the subsequent analysis.

A.4 Derivation of the SHG transfer function

We assume a nonlinear material of length L and centered about $z = 0$. Then, by definition, $d(z) = 0$ for $|z| > L/2$. The boundary conditions $C_1(0,t) = C_1(t)$ and $C_2(-L/2,t) = 0$ apply, where $C_1(t)$ is the fundamental pulse envelope at the center of the nonlinear material. We now define local time variables

$$\eta_1 \equiv t - z/v_{g1} \text{ and} \tag{A.13}$$

$$\eta_2 \equiv t - z/v_{g2} \ , \tag{A.14}$$

and we substitute equation (A.13) into equation (A.11). We confirm the solution

$$C_1(z,t) = C_1(\eta_1), \tag{A.15}$$

implying that the fundamental pulse experiences no pulse distortion, stretching or compression, consistent with the neglect of intra-pulse GVD and pump depletion.

Having a solution for C_1, we can find a solution for C_2 by substituting C_1 into equation (A.12) and changing variables using equation (A.15) and the normalized coordinate $\zeta \equiv z\delta v$. Here we normalize the coordinate variable using the group velocity mismatch (GVM) parameter $\delta v \equiv [1/v_{g1} - 1/v_{g2}]$. These substitutions yield

$$\delta v \frac{\partial}{\partial \zeta} C_2(\zeta, \eta_2) - \frac{i\beta_2}{2} \frac{\partial^2}{\partial \eta_2^2} C_2(\zeta, \eta_2)$$
$$= \Gamma d(\zeta/\delta v) C_1^2(\eta_2 - \zeta) \exp(-i\Delta k_0 \zeta/\delta v) \quad . \tag{A.16}$$

We now move to the spectral domain by taking the Fourier transform of equation (A.16) with respect to local time η_2, where $\Omega = \omega - \omega_{1,2}$ is the transform variable. (i.e. $C(\eta_2) \Rightarrow \hat{C}(\Omega)$). Then,

$$\left[\delta v \frac{\partial}{\partial \zeta} + \frac{i\beta_2 \Omega^2}{2}\right] \hat{C}_2(\zeta, \Omega)$$
$$= \Gamma \int_{-\infty}^{\infty} \exp\left[-i\left(\frac{\Delta k_0 \zeta}{\delta v} + \Omega \eta_2\right)\right] d\left(\frac{\zeta}{\delta v}\right) C_1^2(\eta_2 - \zeta) d\eta_2 \quad , \tag{A.17}$$

where $\hat{C}_2(\zeta, \Omega)$ is the Fourier transform of $C_2(\zeta, \eta_2)$. We note that this ordinary differential equation has an exact solution for any location ζ. This solution is

$$\hat{C}_2(\zeta, \Omega) = \hat{C}_2(\zeta = -L\delta v/2, \Omega) + \frac{\Gamma}{\delta v} \exp\left(-\frac{i\Omega^2 \beta_2 \zeta}{2\delta v}\right) \times$$
$$\int_{-\frac{L\delta}{2}}^{\zeta} \left[\int_{-\infty}^{\infty} \exp\left[-i\left(\frac{\Delta k_0 \zeta'}{\delta v} + \Omega \eta_2\right)\right] d\left(\frac{\zeta'}{\delta v}\right) C_1^2(\eta_2 - \zeta') d\eta_2\right] \exp\left(\frac{i\Omega^2 \beta_2 \zeta'}{2\delta v}\right) d\zeta' \quad , \tag{A.18}$$

where ζ' is a dummy integration variable and $\hat{C}_2(\zeta = -L\delta v/2, \Omega)$ is the spectrum of the second harmonic pulse envelope at the input of the nonlinear material. Since the output pulse is the quantity of greatest interest, we evaluate $\hat{C}_2(\zeta = L\delta v/2, \Omega)$. We then increase the integration bounds from $[-L\delta/2, L\delta/2]$ to $[-\infty, \infty]$, recognizing that this cannot affect the

solution (A.18) because $d(\zeta') = 0$ outside $|\zeta'| > L\delta v/2$. Changing the order of factors in equation (A.18) and making the definition

$$H(\zeta',\Omega) \equiv \frac{\Gamma}{\delta v} d\left(\frac{\zeta'}{\delta v}\right) \exp\left[i\frac{\zeta'}{\delta v}\left(-\Delta k_0 + \frac{\Omega^2 \beta_2}{2} \right)\right] \tag{A.19}$$

gives

$$\hat{C}_2(L\delta v/2, \Omega) = \hat{C}_2(-L\delta v/2, \Omega)$$

$$+ \exp\left(-\frac{i\Omega^2 \beta_2 L}{4} \right) \cdot \int_{-\infty}^{\infty} H(\zeta',\Omega) \int_{-\infty}^{\infty} C_1^2(\eta_2 - \zeta') \exp(-i\Omega\eta_2) d\eta_2 d\zeta' \quad . \tag{A.20}$$

Applying the Fourier shift theorem to the inner integral in the second term in the right hand side of equation (A.20) gives

$$\hat{C}_2(L\delta v/2, \Omega) = \hat{C}_2(-L\delta v/2, \Omega)$$

$$+ \widehat{C_1^2}(\Omega) \times \exp\left(-\frac{i\Omega^2 \beta_2 L}{4} \right) \cdot \int_{-\infty}^{\infty} H(\zeta',\Omega) \exp(-i\Omega\zeta') d\zeta' \ , \tag{A.21}$$

where $\widehat{C_1^2}(\Omega)$ is the Fourier transform of $C_1^2(\eta_2)$. Finally, we apply the boundary condition for the second harmonic field. The time domain boundary condition $C_2(-L\delta v/2, \eta_2) = 0$ becomes $\hat{C}_2(-L\delta v/2, \Omega) = 0$ in the frequency domain. The solution can then be written in the form

$$\hat{C}_2(L\delta v/2, \Omega) = \widehat{C_1^2}(\Omega) \cdot F(\Omega), \tag{A.22}$$

where

$$F(\Omega) = \frac{\Gamma}{\delta\nu}\exp\left(-\frac{i\Omega^2\beta_2 L}{4}\right)\cdot\int_{-\infty}^{\infty}\bar{d}\left(\frac{\zeta'}{\delta\nu}\right)\exp\left[i\left(-\frac{\Delta k_0}{\delta\nu-\Omega}+\frac{\Omega^2\beta_2}{2\delta\nu}\right)\zeta'\right]d\zeta' \qquad (A.23)$$

is a transfer function which relates the spectrum of the second harmonic field to the spectrum of the square of the fundamental field. The transfer function (A.23) is explicitly determined from the material properties and nonlinear coefficient distribution. In many cases it would also be useful to have an explicit expression for the material properties and nonlinear coefficient distribution that yield a desired SHG transfer function. In order to derive this relationship, we return to the position coordinate $z = \zeta'/\delta\nu$ and use the definition

$$\Delta k = \Delta k_0 + \Omega\delta\nu + \Omega^2\beta_2/2 \qquad (A.24)$$

to find

$$F(\Omega) = \Gamma\exp(-i\Omega^2\beta_2 L/4)\cdot\int_{-\infty}^{\infty} d(z)\exp[i\Delta kz]dz. \qquad (A.25)$$

The notation of equation (A.25) for the SHG transfer function can be simplified to

$$F(\Omega) = \Gamma\exp(-i\Omega^2\beta_2 L/4)\cdot\hat{d}(\Delta k), \qquad (A.26)$$

where $\hat{d}(\Delta k) = \hat{d}(\Delta k_0 + \Omega\delta\nu - \Omega^2\beta_2/2)$ is the spatial Fourier transform of the normalized nonlinear coefficient distribution $d(z)$. We note that $\hat{d}(\Delta k)$ is essentially the tuning curve for CW-SHG. Equation (A.26) is the same result as derived in equation (2.55) of chapter 2.

References

[1]M. A. Arbore, O. Marco and M. M. Fejer, "Pulse compression during second harmonic generation in aperiodic quasi-phasematching gratings," Optics Letters, **22**, 865 (1997).

Appendix B: Summary of notation used in chapter 2

Table B. 1: Summary of notation used in chapter 2, listed in alphabetical order.

Symbol	Definition	Description	Reference
$\widehat{\tilde{A_1^2}}(\omega)$	$\widehat{\tilde{A_1^2}}(\omega) = \int_{-\infty}^{\infty} \hat{A}_1(\omega')\hat{A}_1(\omega-\omega')d\omega'$	Self-convolution of $\hat{A}_1(\omega)$	eq. (2.48)
$\widehat{\tilde{A_1^2}}(\omega)$	$\widehat{\tilde{A_1^2}}(\omega) = \widehat{[E_1(0,t)]^2}$	Fourier transform of the square of the fundamental field at the center of the nonlinear crystal	eq. (2.50)
$\hat{A}_i(z,\omega)$		Spatial field envelope at frequency ω_i	eq. (2.17)
a_m	See equation (2.73) or (2.78)	Amplitude of the m-th Fourier component of the periodic nonlinear coefficient distribution	eq. (2.73)
$\hat{A}(z,\omega)$	$\hat{E}(z,\omega) = \hat{A}(z,\omega)\exp[-ik(\omega)z]$	Spatial field envelope	eq. (2.9)
b	$b \equiv \frac{1}{\alpha}\xi_{L_{wg},opt}g(\xi_{L_{wg},opt}=1)$	Pulse-shape efficiency parameter	eq. (2.83)
$\lvert B_{1,0}\rvert^2$	$\lvert B_{1,0}\rvert^2 = B_{1,0}\cdot B_{1,0}^*$	Squared magnitude of the peak fundamental field, $B_{1,0}$	below (2.64)

Table B. 1: Summary of notation used in chapter 2, listed in alphabetical order.

Symbol	Definition	Description	Reference
$\widehat{B_1^2}(\omega)$		Fourier transform of the square of the fundamental temporal field envelope at the center of the nonlinear crystal	below (2.99)
b_{crit}	$b_{crit} \equiv \frac{\sqrt{\xi_{L_{walk},opt}}}{\alpha} g(\xi_{L_{walk},opt} = 1)$	Pulse shape efficiency parameter for critically-phasematched ultrashort-pulse SHG	eq. (2.88)
$B_i(z, t)$		Temporal envelope at frequency ω_i	eq. (2.52)
$B_{i,0}$		Field amplitude of (temporal) peak of fundamental pulse	above (2.96)
$\hat{d}[\Delta k']$	See equation (2.47)	Spatial Fourier transform of the normalized nonlinear coefficient distribution. (Tuning curve for CW-SHG)	after (2.47)
d_{eff}		maximum effective nonlinearity	below (2.27)
D_{g2}	See equation (2.90)	Lowest-order chirp of QPM grating	eq. (2.90)
$D_{g2,opt}$	$D_{g2,opt} \equiv \frac{\delta\nu^2}{2\beta_2 L - D_p}$	QPM grating chirp which generates a transform-limited SH pulse	eq. (2.105)
$D_{g,i}$	See equation (2.90)	Higher-order chirp of QPM grating	eq. (2.90)
$1/D_p$		Chirp on fundamental pulse at the center of the nonlinear material	above (2.96)
$1/D_{SH}$	$D_{SH} \equiv D_p/2 + (\delta\nu)^2/2D_{g2} - \beta_2 L$	Chirp on the SH pulse	eq. (2.103)

Table B. 1: Summary of notation used in chapter 2, listed in alphabetical order.

Symbol	Definition	Description	Reference
$D(\Omega, \Omega_a, z')$	$D(\Omega, \Omega_a, z') \equiv d(z') (\exp[-i\Delta k''(\Omega, \Omega_a)z'] - 1)$	Weighted nonlinear coefficient	below (2.46)
$d(z)$	$d(z) \equiv \chi^{(2)}(z)/(2d_{eff})$	normalized nonlinear coefficient	below (2.27)
$\mathcal{E}_p$		Fundamental pulse energy	below (2.82)
E_i		Electric field at frequency ω_i	eq. (2.15)
FOM	$\text{FOM} \equiv d_{eff}^2/(n_1 n_2 \Delta n_g)$	Figure Of Merit for ultrashort-pulse SHG	eq. (2.82)
FOM_{crit}	$\text{FOM}_{crit} \equiv \frac{d_{eff}^2}{n_1^{1.5} n_2 \sqrt{\Delta n_g \rho}}$	Figure Of Merit for critically-phase-matched ultrashort-pulse SHG	eq. (2.87)
$g(\xi_{L_{max}})$	See equation (2.65) or $g(0) = \frac{1}{A_1^2} \cdot \frac{\int \lvert\widehat{A_1^2}(\Omega)\rvert^2 d\Omega}{\int \lvert\hat{A}_1(\Omega)\rvert^2 d\Omega}$	Pulsed-SHG efficiency reduction factor. ($g = 1$ for single-frequency CW-SHG)	eq. (2.65)
h	$h = 0.8$ for confocal focusing	Boyd & Kleinman efficiency reduction factor for focused Gaussian beams	below (2.79)
I_p	See equations (2.111)	Temporal peak fundamental intensity	eq. (2.111)
k	$k^2 \equiv [\omega^2 \varepsilon(\omega)]/c^2$	**k**-vector in the medium	below (2.9)
$k_{g,m}$	See equation (2.73)	**k**-vector of the m-th Fourier component of the periodic nonlinear coefficient distribution	below (2.73)
$k_i(\omega)$	See equation (2.39)	**k**-vector near $\omega = \omega_i$	eq. (2.39)

Table B. 1: Summary of notation used in chapter 2, listed in alphabetical order.

Symbol	Definition	Description	Reference
$\tilde{k}_i(\omega-\omega_i)$	See equation (2.39)	Dispersion terms at frequency ω_i with order higher than two	eq. (2.39)
Δk_0	$\Delta k_0 \equiv 2k_1 - k_2$	**k**-vector mismatch	below (2.45)
$\Delta k_a(\Omega)$	$\Delta k_a(\Omega) \equiv \delta\nu\Omega + \Delta\beta\Omega^2 + \tilde{k}_2(\Omega)$	Dispersion of the **k**-vector mismatch	below (2.93)
$\Delta k(\omega, \omega')$	$\Delta k(\omega, \omega') \equiv k(\omega') + k(\omega-\omega') - k(\omega)$	Dispersion of the **k**-vector mismatch	eq. (2.37)
$\Delta k'(\Omega)$	$\Delta k'(\Omega) \equiv \Delta k_0 + \delta\nu\Omega + \Delta\beta\Omega^2 + \tilde{k}_2(\Omega)$	ω'-independent dispersion terms	eq. (2.44)
$\Delta k''(\Omega, \Omega_a)$	$\Delta k''(\Omega, \Omega_a) \equiv \beta_1(\Omega_a^2 - \Omega\Omega_a) + \tilde{k}_1(\Omega-\Omega_a)$	ω'-dependent dispersion terms	eq. (2.45)
L_{max}	$L_{max} \equiv \frac{0.886\pi}{\delta\nu \cdot \Delta\Omega_{Pulse}}$	Characteristic crystal length, satisfying $\frac{\Delta\Omega_{SHG}}{2} = \Delta\Omega_{Pulse}$	eq. (2.62)
L		length of the nonlinear material	below (2.20)
L_{min}	$L_{min} \approx 3\lvert\delta\nu/D_{g2}\tau_1\rvert$	Minimum chirped-QPM crystal length	below (2.93)
L_{opt}	satisfies $\tau_{nor} = 1$	optimum crystal length	below (2.72)
$L_{walkoff}$	$L_{walkoff} \equiv \tau_1/\delta\nu$	Group velocity walkoff length	above (2.68)
n	$n = \sqrt{\varepsilon}$	refractive index	below (2.7)
$n_{1,2}$		refractive index at fundamental (1) or SH (2) frequencies	below (2.31)
$n_{g,i}$	$n_{g,i} \equiv c/v_{g,i}$	group refractive index	below (2.81)
P_1		Power of CW beam	below (2.79)

Table B. 1: Summary of notation used in chapter 2, listed in alphabetical order.

Symbol	Definition	Description	Reference
$P_{1,0}$		Temporal peak fundamental power	below (2.80)
$\widehat{P_{NL}}(z, \omega)$	See equation (2.26) or (2.27)	Nonlinear electric polarization	eq. (2.26) or (2.27)
TBP	See table 2.1	Time-bandwidth product	eq. (2.68)
$v_{g,i}$	$v_{g,i} \equiv 1/\left(\frac{\partial k}{\partial \omega_i}\right)$	Group velocity in the medium at the fundamental (i=1) and second harmonic (i=2) frequencies	eq. (2.40)
z		propagation direction	below (2.7)
α	$\mathcal{E}_p = \alpha P_{1,0}\tau_1$	Pulse shape dependent constant	below (2.82)
β_i	$\beta_i \equiv \left.\frac{\partial^2 k}{\partial \omega^2}\right\|_{\omega_i}$	group velocity dispersion (GVD) in the medium at the fundamental (i=1) and second harmonic (i=2) frequencies	eq. (2.41)
$\delta\beta$	$\delta\beta \equiv (1/2)[\beta_1 - \beta_2]$	GVD mismatch	below (2.45)
Δn_g	$\Delta n_g \equiv n_{g,1} - n_{g,2}$	group refractive index mismatch	below (2.81)
δv	$\delta v \equiv [1/v_{g1} - 1/v_{g2}]$	group velocity mismatch (GVM) parameter	below (2.45)
$\Delta\Omega_{SHG}$	$\Delta\Omega_{SHG} = 1.77\pi/\delta v L$	FWHM bandwidth of the transfer function for uniform crystal	below (2.61)
$\Delta\Omega_{Pulse}$	$\Delta\Omega_{Pulse} = 2\pi \cdot \mathrm{TBP}/\tau_1$	FWHM bandwidth of the fundamental pulse	above (2.68)

Table B. 1: Summary of notation used in chapter 2, listed in alphabetical order.

Symbol	Definition	Description	Reference
η_{conf}	$\eta_{conf} = \frac{2.54\pi^3}{\varepsilon_0 \lambda_1^3}\text{FOM} \cdot \mathcal{E}_p \cdot \frac{\tau_0}{\tau}$ or see equation (2.114)	Conversion efficiency for confocally focused SHG of chirped Gaussian pulses in chirped-QPM materials of minimum length	eqs. (2.113) and (2.114)
η_E	$\eta_E = \Gamma^2 \lvert B_{1,0}\rvert^2 L_{max}^2 \xi_{L_{max}}{}^2 g(\xi_{L_{max}})$	Energy conversion efficiency	eq. (2.64)
$\eta_{E,0}$	$\eta_{E,0} = 1.6\Gamma^2(B_{1,0}^2\tau_0)[\tau_0/(\delta\nu)^2]$	Efficiency for plane-wave SHG of unchirped pulses in a homogeneous (or periodic QPM) material of one group velocity walkoff length	eq. (2.110)
$\eta_{E,PW}$	$\eta_{E,PW} = \frac{\pi}{\sqrt{2}}\Gamma^2(B_{1,0}^2\tau_0)\frac{1}{\tau}\frac{1}{D_{g2}}$	Efficiency of plane-wave SHG of chirped pulses in a chirped-QPM material with $L \geq L_{min}$	eq. (2.109)
Γ	$\Gamma \equiv -i2\pi d_{eff}/(\lambda_1 n_2)$	Nonlinear coupling coefficient	below (2.31)
$\lambda_{1,2}$		free-space wavelengths at fundamental (i=1) and second harmonic (i=2) carrier frequencies	below (2.30)
Λ_{local}	See equation (2.91)	Local QPM period	eq. (2.91)
Λ_{QPM}	$\Lambda_{QPM} = 2\pi m/\Delta k_0$	m-th-order QPM grating period	below (2.76)
ω_i	$\omega_2 = 2\omega_1$ and $\omega_i = (2\pi c)/\lambda_i$	fundamental (i=1) and second harmonic (i=2) carrier frequencies	below (2.30)
Ω	$\Omega \equiv \omega - \omega_2$	Frequency relative to SH carrier	below (2.41)

Table B. 1: Summary of notation used in chapter 2, listed in alphabetical order.

Symbol	Definition	Description	Reference
Ω_1	$\Omega_1 \equiv \omega - \omega_1$	Frequency relative to fundamental carrier frequency	below (2.97)
Ω_a	$\Omega_a \equiv \omega' - \omega_1$	Dummy integration frequency relative to fundamental carrier	below (2.41)
ρ		Poynting vector walkoff angle	above (2.85)
τ_0	$\tau_0 = \tau_1/(2 \cdot \sqrt{\ln 2})$	$1/e$ power half-width of fundamental pulse	above (2.96)
τ_1		fundamental pulse FWHM duration	above (2.68)
τ_2		SH pulse FWHM duration	below (2.71)
τ_{nor}	$\tau_{nor} \equiv \tau_2/\tau_1$	normalized pulse length parameter	below (2.71)
τ_{SH}	$\tau_{SH} = \sqrt{\left(\frac{\tau_0}{\sqrt{2}}\right)^2 + \left(\frac{\sqrt{2}D_{SH}}{\tau_0}\right)^2}$	$1/e$ power half-width of the SH pulse	eq. (2.104)
$\xi_{L_{max}}$	$\xi_{L_{max}} \equiv L/L_{max}$	normalized crystal length	below (2.63)
$\xi_{L_{max},opt}$	$\xi_{opt} \equiv L_{opt}/L_{max}$	Optimum crystal length normalized to L_{max}	below (2.72)
$\xi_{L_{wo}}$	$\xi_{L_{wo}} \equiv L/L_{walkoff}$	Walkoff-normalized crystal length	eq. (2.70)
$\xi_{L_{wo},opt}$	$\xi_{opt} \equiv L_{opt}/L_{walkoff}$	Optimum crystal length normalized to walkoff length	below (2.72)

IMAGE EVALUATION TEST TARGET (QA-3)

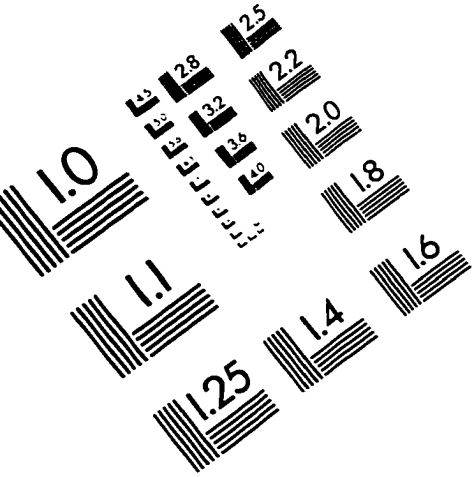

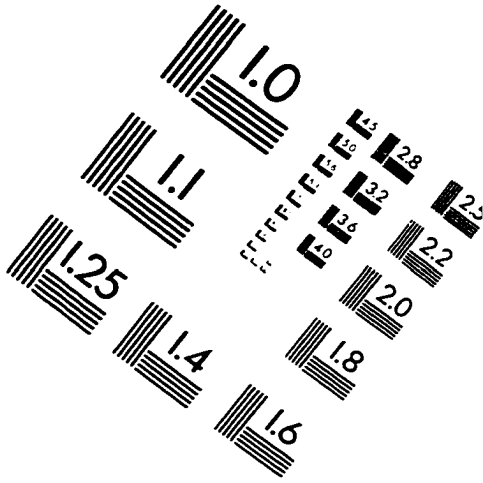

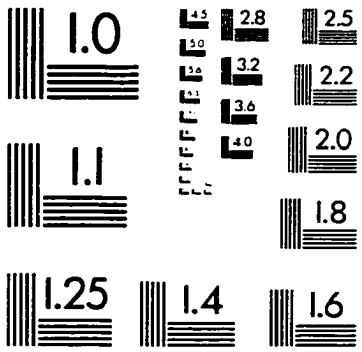

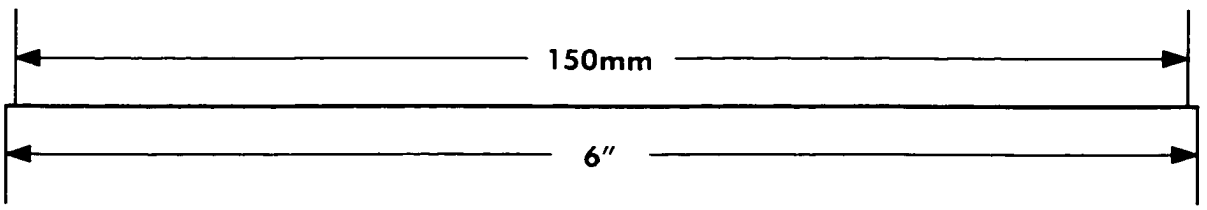

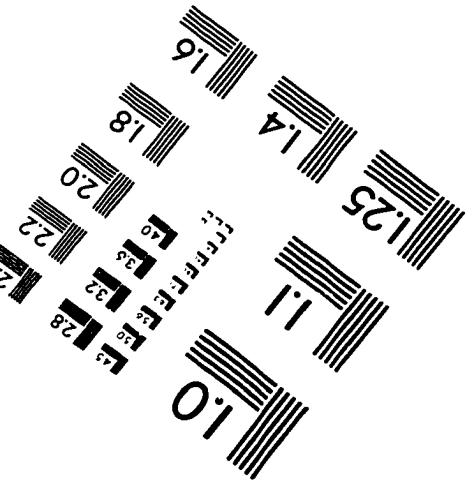

APPLIED IMAGE, Inc
1653 East Main Street
Rochester, NY 14609 USA
Phone: 716/482-0300
Fax: 716/288-5989